Visualisation of magnetic domain structures and magnetisation processes in Goss-oriented, high permeability steels using neutron grating interferometry

PAR

Benedikt Karl-Josef Gerhard BETZ

ÉCOLE POLYTECHNIQUE
FÉDÉRALE DE LAUSANNE

Suisse
2016

Mir wird applaudiert,
weil mich jeder versteht,
und ihnen, weil Sie niemand versteht.
— C. Chaplin zu A. Einstein

...lieber stehend sterben,
als knieend leben...
— Kevin Russel

Abstract

Industrial transformer cores are built from stacked sheets of an iron silicon alloy, which are called laminations. The internal magnetic domain structures of these highly anisotropic grain-oriented electrical steel laminations with a sharp (110) [001]-texture, the so-called Goss-texture, determines predominantly the magnetic properties of transformer cores and thereby the degree of efficiency and the performance of transformers. Such typical laminations are 300 μm thick and are coated by a glassy magnesium silicate layer.

The most commonly used investigation techniques for these laminations are inductive B-H-hysteresis-measurements using fluxmeters. This technique reveals global magnetic properties such as magnetic hysteresis, remanence, saturation and losses. Locally resolved information about the underlying domain structure cannot be obtained by this method. Hence, the surface domain structure is predominantly studied by Kerr-microscopy investigations. Here, the limited information depth of $\approx$20 nanometers allows only for indirect interpretation of the internal volume domain structures. Furthermore, the field of view is limited to some millimeters.

In this thesis, the neutron grating interferometer (nGI) technique is used for the investigation of magnetic domain structures in Goss-oriented (GO-) electrical steels at the Swiss Spallation Neutron Source (SINQ) using the cold neutron imaging facility ICON. In contrast to the attenuation based transmission image, the dark-field image (DFI) is related to multiple refraction of unpolarised neutrons at magnetic domain walls. Thereby the use of the DFI allows for the visualisation of bulk magnetic domain structures in two dimensions as even in three dimensions with a spatial resolution of down to 70 μm in a field of view of up to 4096 mm^2 (64 mm × 64 mm).

In particular the DFI is used for the in-situ visualisation of the locally resolved response of the bulk and the supplementary magnetic domain structures in GO-steels under the influence of externally applied magnetic fields. In the first part, the domain formation and growth along the initial magnetisation curve (0 A/m - 6000 A/m) up to the saturated state in static DC magnetic fields was studied. For decreasing field values, the visualisation of the recurrence of the hysteretic domain structure down to the remanent (0 A/m) state is given.

In the second part, the DFI was used to visualise and interpret the response of bulk magnetic domain walls to dynamic AC magnetic excitations. The visualisation of the domain wall motion under the influence of an external alternating sinusoidal magnetic field is performed. In detail, scans combining varying levels of DC$_{offset}$ (0 A/m - 30 A/m), oscillation amplitude A$_{AC}$ (0 A/m – 1500 A/m), and oscillation frequency f$_{AC}$ (0 Hz – 200 Hz) are conducted. By increasing

the amplitude A_{AC} while maintaining constant values of DC_{offset} and f_{AC}, the transition from a frozen domain wall structure to a mobile one is recorded. Vice versa, increasing f_{AC} while keeping A_{AC} and DC_{offset} constant led to the reverse transition from a mobile domain wall structure into a frozen one. It is shown that varying both A_{AC} and f_{AC} shifts the position of transition region and that higher frequencies require higher oscillation amplitudes to overcome the freezing phenomena.

In addition, the DFI allows for the analysis of the laminations coatings' influence onto the volume and the supplementary surface magnetic domain structures. To visualise the stress effect of the coating onto the underlying domain formation an uncoated lamination was investigated with stepwise increasing applied external tensile stresses up to 20 MPa. Hereby the domain configurations of the intermediate stress states are imaged and finally the original domain structure of the coated state is reproduced. More detailed, the visualisation of how the applied stresses lead to a refinement of the volume domain structure and the suppression and reoccurring of supplementary domains is given.

To compare and verify the results of the nGI, complementary experiments using magneto-optical Kerr microscopy, Faraday imaging, small-angle neutron scattering and Laue X-ray diffraction experiments were performed.

The here presented experimental findings allow for new fundamental insights into macro-magnetism and enable new approaches in the field of descriptive models for bulk macro-magnetic phenomena. Furthermore the results have the potential to further improve the properties of GO-steels used in industrial transformer applications.

Key words: Neutron imaging; neutron grating interferometry; magnetism; dark-field imaging; magnetic domains; electrical steel; Goss-orientation;

Kurzfassung

Die Leistung und die Effektivität elektrotechnischer Bauteile wie Transformatoren werden maßgeblich von den magnetischen Eigenschaften kornorientierter Elektrobleche beeinflusst. Die Kerne moderner Transformatoren sind aus gestapelten, höchst anisotropen[1] Elektroblechen aufgebaut. Die innere magnetische Domänenstruktur dieser, sogenannter Goss Bleche (scharfe (110)[001] Textur), bestimmt im Wesentlichen die magnetischen Eigenschaften des Transformators. Typischerweise sind die einzelnen Bleche 300μm dick und mit einer glasigen Schutzschicht überzogen.

Standardmäßig werden diese Bleche mittels induktiver Magnetfeldmessungen untersucht. Diese Untersuchungen liefern hysteretische B-H Kennlinien, welche die globalen magnetischen Eigenschaften wie magnetische Verluste oder die Sättigungsmagnetisierung einer Probe liefern. Die unterliegende magnetische Domänenstruktur hingegen bleibt hierbei völlig unerforscht. Magnetische Oberflächendomänen werden hauptsächlich durch Kerr Mikroskopie untersucht, welche jedoch durch ein kleines Sichtfeld von wenigen Millimetern und die geringe Eindringtiefe von ca. 20 Nanometern begrenzt ist.

In dieser Arbeit, wird nun die Neutronen Gitter Interferometrie (nGI) an der Strahllinie ICON der Schweizer Spallations Neutronen Quelle (SINQ) am Paul Scherrer Institut genutzt, um die magnetischen Domänenstrukturen in solchen Goss-orientierten Elektroblechen zu untersuchen. Im Gegensatz zum konventionellem Transmissionsbild kann das sogenannte "dark-field Image" (DFI) die Streuung von unpolarisierten Neutronen an magnetischen Domänenwänden abbilden. Daher kann mit dem nGI die Abbildung von Domänenstrukturen sowohl in zwei als auch in drei Dimensionen mit einer räumlichen Auflösung von bis zu 70 μm erreicht werden.

Im Einzelnen wird mit Hilfe des DFI das Verhalten von Volumen- und Oberflächendomänen unter dem Einfluss von extern angelegten magnetischen Feldern untersucht. Die Formation von Domänenstrukturen während des Abschreitens einer magnetischen Neukurve (0 A/m - 6000 A/m) bis zur magnetischen Sättigung der Probe wird in einzelnen Schritten verbildlicht. Für die hysteretische Entmagnetisierung der Probe wird das Wiedererscheinen der Domänen beobachtet und der remanente Zustand (0 A/m) kann abgebildet werden. Zusätzlich wird ein Zusammenhang zwischen der Kornorientierung und der zugehörigen Volumen- und Oberflächendomänenstruktur herausgearbeitet.

Zweitens, wird die Reaktion der Domänen auf dynamische magnetische Wechselfelder untersucht. Eine sinusförmige magnetische Anregung mit variierender Frequenz f_{AC} (0 Hz -

---

[1]Aufgrund der präferierten Kornorientierung

200 Hz), Amplitude A_{AC} (0 A/m - 1500 A/m) und/oder Offset DC_{offset} (0 A/m - 30 A/m) wird dafür angelegt. Wird bei konstant gehaltener Frequenz und Offset die Amplitude erhöht, kann ein Übergang von einer eingefrorenen zu einer mobilisierten Domänenstruktur beobachtet werden. Wird hingegen die Frequenz bei konstantem Offset und konstanter Amplitude erhöht, so ist der umgekehrte Übergang von mobilisierten Domänenstrukturen hin zu einer eingefrorenen zu finden. Weiterhin wird gezeigt, dass die Variation beider Parameter f_{AC} und A_{AC} dazu führt, dass die Übergangsregion für höhere Frequenzen hin zu höheren Amplituden verschoben wird.

Der Einfluss der isolierenden Schutzschicht der Bleche auf die magnetische Domänenstruktur wird visualisiert, indem bei einem Blech die Schutzschicht entfernt und es mit dem ursprünglichen magnetischen Zustand des beschichteten Blechs verglichen wird. Im Folgenden induziert eine externe Kraft schrittweise steigende interne Spannungen in dieses unbeschichtete Blech. Durch diese Spannungen können sowohl die dazwischen liegenden Stadien der Domänenstruktur, als auch die finale Reproduktion der ursprünglichen, magnetischen Struktur des beschichteten Blechs gezeigt werden.

Um die magnetischen Ergebnisse, die mit Hilfe des nGIs erhalten wurden, zu verstehen und zu verifizieren, wurden magneto-optische Kerr Mikroskopie Untersuchungen, Faradayexperimente, Kleinwinkelstreumessungen und Röntgen Laue Diffraktionsexperimente durchgeführt. Die in dieser Arbeit präsentierten experimentellen Ergebnisse können helfen, die magnetischen Eigenschaften von Transformatorblechen und damit die Effektivität und Qualität von Transformatoren weiter zu verbessern. Des Weiteren können Modelle für die Beschreibung von makroskopischen magnetischen Phänomenen weiterentwickelt werden.

Stichwörter: Neutron Imaging; Neutron Gitter Interferometrie; Magnetismus; Dunkelfeldimaging; Magnetische Domänen; Elektroblech; Goss-orientation;

Contents

Contents

Contents

List of Figures

List of Symbols

U	voltage
N	windings of a coil
P	magnetic losses
J_s	saturation polarisation
$R_{0.2}$	yield point
R_m	tensile strength
R_u	tearing strength
H	magnetic field
B_s	saturation magnetisation
B_v	vacuum magnetisation
I	electrical current
l_m	magnetic length
B	magnetic flux density
R_i	resistance
B_r	remanent flux
H_c	coercive field
J_{800}	polarisation with 800 A/m applied field
P_{50}	losses at 50 Hz
μ_r	relative permeability
P_{ed}	eddy-current losses
f	frequency
ρ	specific electrical resistance
d	thickness of a lamination
μ_N	magnetic moment of a neutron
Θ	rotation angle
M	magnetisation
ϑ_s	crystallographic misorientation angle
t_0	characteristical length for supplementary domain generation
A	exchange constant $[\frac{J}{m}]$
K	anisotropy constant $[\frac{J}{m^3}]$
K_d	stray field constant $[\frac{J}{m^3}]$
E_{Ze}	Zeeman energy
M_s	saturation magnetisation

List of Symbols

G_0, G_1, G_2	gratings of the nGI setup
p_0, p_1, p_2	periods of the gratings
s	slit width of the source grating
λ	wavelength of neutrons
l	distance between G_0 and G_1
n_{SLD}	neutron scattering length density
h_1	height of the phase grating G_1
Φ	phase shift
d_T	Talbot distance
x_{st}	direction of stepping
$I(m, n, x_{st})$	intensity in each detector pixel (m,n)
a_i	amplitude coefficient
ϕ_i	phase coefficient
k	wave vector
V	visibility
n	refractive index
δ	real part of the refractive index
β	imaginary part of the refractive index
h	Planck constant
B_k	knee of the magnetisation curve
Ω_{MCS}	dark-field coefficient for monodisperse colloidal systems
G	real space correlation function
ξ_{setup}	setup parameter
SDD_{eff}	effective sample-to-detector distance
$|\Delta n_{nuc}|$	difference in the nuclear part of the refractive indices
C	concentration
D_{DS}	sample to detector distance in SANS
$\vec{q}$	scattering vector
σ	internal stress
DC_{offset}	Offset of an alternating magnetic excitation
A_{AC}	Amplitude of an alternating magnetic excitation
f_{AC}	Frequency of an alternating magnetic excitation

Preface

The following thesis is divided into seven chapters.

The **first** chapter is the introduction and explains the importance of the investigated material. The magnetic and mechanical basics as well as the application field of electrical steels are introduced and the differences between Non-oriented and Grain-oriented electrical steels are explained. The influences of external coatings, electrical steel laminations are usually coated with, are explained and the standard investigation techniques for electrical steels are mentioned. Finally the motivation of the thesis is derived.

In the **second** chapter a detailed description of the underlying and determining magnetic domain structures in Goss-oriented electrical steels is given. Both, basic domains structures as well as supplementary domain structures fundamentally determine the materials properties. However both are not investigated using standard techniques. The magnetisation behaviour of different domain structures is shown for externally applied magnetic fields. The basics of neutron interaction with matter as well as the wave-optical description are given for nuclear and magnetic interactions. The principle of neutron grating interferometry, the data acquisition and the image processing is explained.

The **third** chapter focuses on the setup and the sample environments. The individual setup gratings are shown and the sample environment for various external influences like magnetic excitations and stress applications are explained and illustrated. Afterwards, the dark-field signal is characterised concerning on the one hand the particle size dependent (ultra-) small angle scattering and on the other hand the concentration dependent altering of the macroscopic scattering cross sections. Thereby the sensitivity range of the used instrument is derived.

In chapter **four** it is shown, how the DFI allows for the *in-situ* visualisation of the locally resolved response of the bulk and the supplementary magnetic domain structure in GO-steels under the influence of externally applied magnetic fields. In particular, the domain formation and growth along the initial magnetisation curve up to the saturated state is shown. For decreasing field values, the recurrence of the hysteretic domain structures down to the remanent state is visualised. Additionally, the DFI allows to derive a link between the grain orientation and the corresponding volume and supplementary domain structures. To compare and sus-

tain the DFI findings, complementary experiments using magneto-optical Kerr microscopy, Faraday imaging, small-angle neutron scattering and Laue X-ray diffraction are performed and presented.

The DFI is used in Chapter **five**, to visualise and interpret the response of bulk magnetic domain walls to dynamic magnetic excitations. Hereby, the transition regions between frequency-induced domain wall freezing and amplitude-induced domain wall mobilisation could be identified. In particular, the behaviour of the magnetic domains under the influence of a DC_{offset}, an oscillation amplitude A_{AC} and a frequency f_{AC} is studied. Freezing phenomena for magnetic domain walls are directly visualised and explained by eddy-current damping effects. The transition from mobilised to frozen domain wall structures were found to be frequency but also amplitude dependent. The interplay of those two parameters is studied, and a frequency dependent shift of the amplitude induced transitions was found.

The DFI investigations in chapter **six** show the impact of the protective coating, GO-steel laminations are commonly coated with, to the volume basic and supplementary magnetic domain structure. To visualise the effect of the inter-granular tensile stresses induced by the coating to the underlying domain formation, an uncoated GO-lamination is used. Stepwise increasing external tensile stresses up to 20 MPa are applied. Hereby the domain configuration of the intermediate stress states are recorded, and finally the original domain structure of the coated state is recreated. More detailed, the externally applied stresses compensate for the removed stresses by uncoating the lamination.

Chapter **seven** gives the conclusion and outlook. This chapter reports on the results and explanations from the experimental chapters and puts them together in context. The found results pave the way for additional questions and experiments. Future experiments are proposed in the outlook and the potential of the technique is outlined.

1 Introduction

In this chapter the mechanical and magnetic basics and the application of electrical steels are introduced. The differences between Non-oriented and Grain-oriented electrical steels are explained. Mechanical as well as magnetic properties are explained and the influence of external coatings to electrical steels is derived. The investigation techniques that are standardly used to characterise electrical steels are mentioned and the motivation of the thesis is given at the end of this chapter.

1.1 Application range and properties of electrical steels

1.1.1 Application range

Electrical steels are a key material for power apparatus in electric home appliances, industrial machinery and transport equipment, though they also are used in the field of renewable energy and the processing electrical and automotive industries. There is a diversity of applications for electrical steels. Large coils of different types of electrical steels are industrially produced, as depicted in Figure 1.1.

Figure 1.1: Coiled electrical steel sheet, as they are produced in industry. The sheet itself has a thickness of 350 μm and the roll is about 1.5 m in diameter [1].
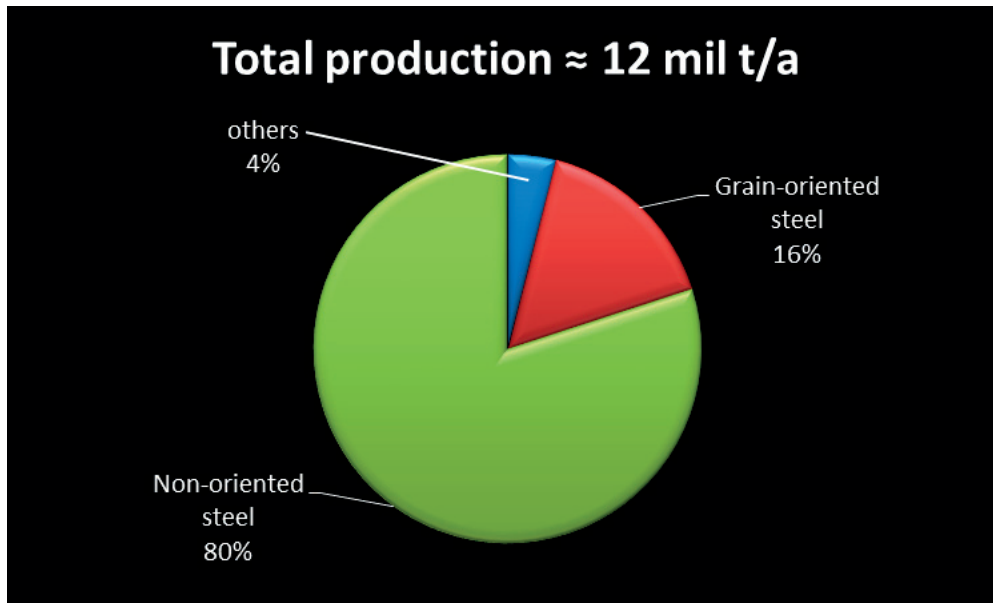
Figure 1.2: Share of Non-oriented electrical steels and Grain-oriented electrical steels in the annual production of soft magnetic materials [4].

The main categorisation of electrical steel is between:

- Non-oriented (NOR) electrical steel also called generator steel

- Grain-oriented (GRO) electrical steel also called transformer steel

The share of electrical steel on the world's annual steel production is just $\approx$ 1%. This is still about an amount of 12 million tons per year [2]. In the world market for soft magnetic materials electrical steel accounts for 96 % of the yearly produced quantities [3]. Figure 1.2 illustrates the classification of the yearly production of soft magnetic materials [4]. It is also shown, that the amount of Non-oriented electrical steel (80%) is much higher as compared to the annual amount of Grain-oriented electrical steel (16 %).

Non-oriented electrical steel

Non-oriented electrical steels are magnetically isotropic, meaning they exercise their magnetic properties equivalently in any given direction. This makes NOR-steels especially well-suited for use, where the transport of electrical energy in several directions is important, such as in electric motors or in generators.
Newly developed hybrid, as well as electric motors have higher claims to their components as traditional electrical motors e.g. in machine tools have, since they operate at up to four times the speed of the most powerful motors currently used in industrial applications. The objective in respect of such motors is to minimise losses so that as much as possible of the energy stored in the batteries of electric cars can be converted into motion. An example of a rotor-stator package used in an electric motor is shown in Figure 1.3.

Figure 1.3: Rotor-stator package built from stacked laminations as used by ThyssenKrupp [5].

Many different kinds of electrical motors exist, but they all have in common the conversion of electrical energy into mechanical energy. Conventionally, the force, which is acting through a magnetic field onto a current-carrying conductor, is converted into motion in such a device. A generator does it the other way round, by converting motion into electric or magnetic energy by the use of the same effects and convertability of forces. Electric motors are used in the modern world to drive various machinery and transport equipment (mainly rolling stock) and their impact can be seen in how they account for over 50 percent of electricity consumption in Germany for example [6]. By using these continuously developing NOR-steels, significant increases in efficiency as well as loss reductions are and will be achieved in the future. A variety of different NOR-steels exist, and they are distinguished by different grades. These grade indicate the the losses and the thickness of the sheet.

Grain-oriented electrical steel

Grain-oriented electrical steels are magnetically highly anisotropic and provide their magnetic properties in a dedicated direction only, the rolling direction[1]. GRO-steels are solely available as a thin sheet with a thicknesses of less than 1 mm. Preferably they are produced even thinner with a thickness of 350 μm or 175 μm, with respect to their dedicated applications. The main application for GRO-steels are the manufacturing of transformer cores, power reactors and hydro-generators. GRO-steels are used wherever the magnetic flux path is entirely or predominantly along a dedicated direction, generally in the rolling direction of the material. Thin GRO-steel laminations[2] are used as material in transformer cores where they are wound by wires, allowing for a high magnetic flux induction. Also for GRO-steels, a multitude of

---

[1]The direction, in the plane of the sheet, perpendicular to the axes of the rolls during rolling [7]. Compare also Figure 1.7 & 1.8

[2]Electrical steels in the form of thin cold-rolled strips are called laminations
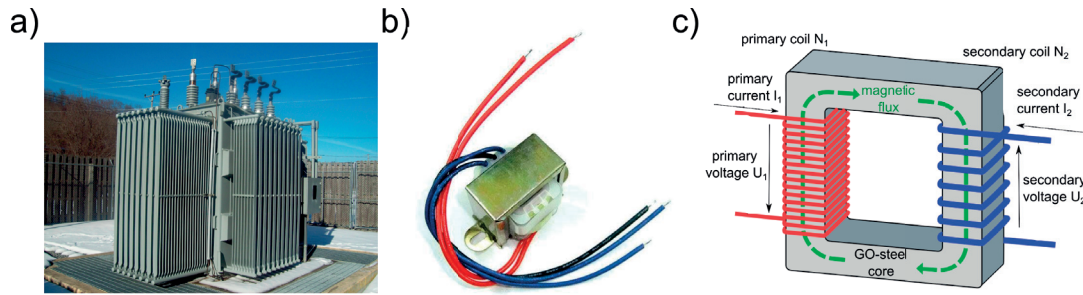
Figure 1.4: Exemplary applications of transformers. a) Industrial transformer as used in an electrical substation [9]. b) Thumbnail sized transformer as used in a computer [10]. c) A schematic of a transformer with GRO-steel core, windings and magnetic flux are delineated. Adapted from [11].

grades exists. The grades display again the losses and the thickness of the lamination. Transformers are available from units with a weight of some hundreds of tons used for the coupling of national electricity grids working with millions of volt-amperes (VA), down to thumbnail sizes, transferring less than one thousandth of VA. Figure 1.4 a) shows such a huge transformer as it is used in an electrical substation, while in b) a centimeter sized transformer, as it is used in a computer, is shown. A schematic of a transformer is depicted in Figure 1.4 c). The primary voltage U_1 in the primary coil with N_1 windings induces a magnetic flux ϕ in the core. The magnetic flux in the core induces a voltage U_2 in the secondary coil with a number of N_2 windings. The voltage is transformed and can be calculated using the following equation: $\frac{U_2}{U_1} = \frac{N_2}{N_1}$.

The core material, which is GRO-steel, determines the efficiency of the transformer by its magnetic properties and so is very relevant for industrial use and industrial competition. The annual global expenditures on transformers are growing and were in the range of 10 billion euros in 2008. This indicates the significance of transformers and their applications for industry [8].

When the magnetic flux transport is important for the performance, the use of electrical steels can be of benefit. NOR-steels are used when various in-plane magnetisation are needed, while GRO-steels provide best results when the magnetic flux is directed only in a single direction. Although the industrial importance of NOR-steels is higher, in the following the focus will be on GRO-steels. The production of this material is highly sophisticated, resulting in expensive production routines. The very anisotropic magnetic properties and their fundamental influence to the performance of transformers is investigated within this thesis.

1.1.2 Magnetic properties of Grain-oriented electrical steels

Electrical steels in general are an iron alloy comprising 0 to 6.5% silicon. The silicon significantly increases the electrical resistivity, Figure 1.5 a), which decreases the induced eddy currentseddy-current (compare section 1.1.3) and lowers the core losses, visible in Figure 1.5

a)

b)

c)
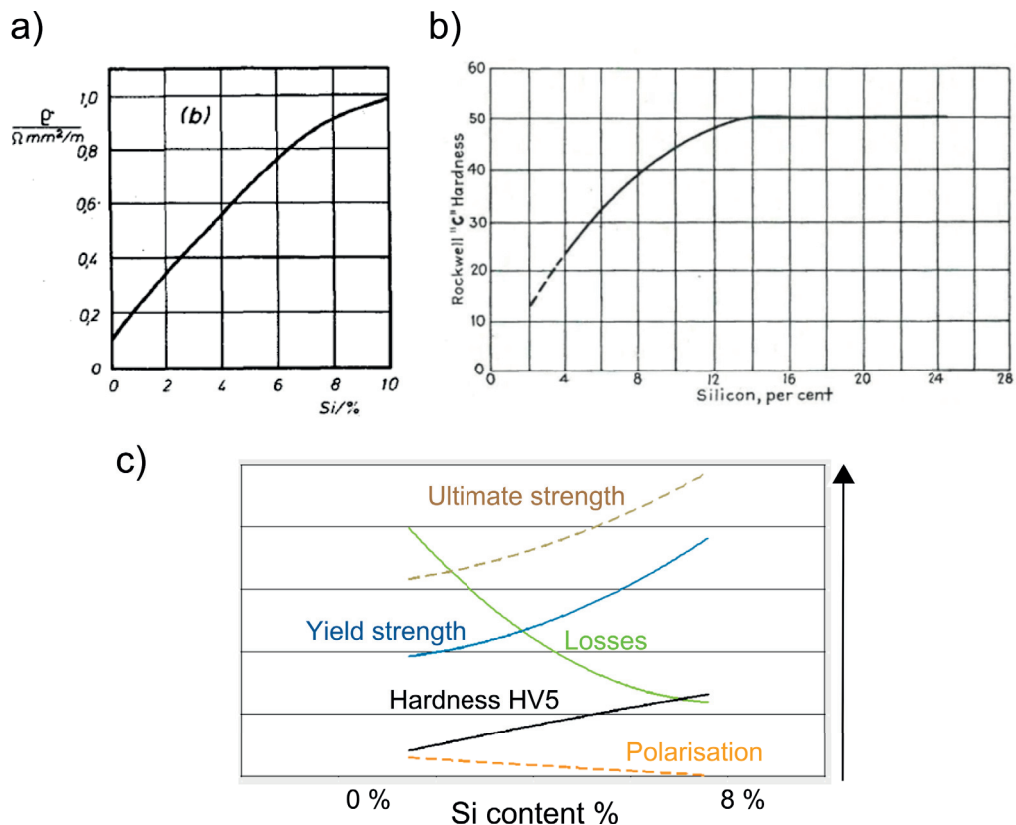
Figure 1.5: Influence of alloying with silicon. a) Electrical resistivity increasing with the silicon contend in the FeSi alloy [12]. b) The Rockwell hardness of the alloy increases by the addition of silicon[14]. c) The magnetic losses decrease by increasing the silicon contend, while the magnetic polarisation decreases slightly. The ultimate strength, the yield strength and the hardness increase, leading to difficulties in the production [13].

c). However, the grain structure hardens and the alloy is more brittle due to the alloying with silicon. This adversely affects the workability of the material and produces difficulties in the production especially during cold rolling. Therefore, electrical steels are commercially only produced up to 3.2% silicon content. Figure 1.5 shows some effects of the silicon alloying. In a) the electrical resistivity increases with increasing silicon contend. The Rockwell hardness, shown in b), is increasing. Additionally in c) it is shown, that the magnetic polarisation decreases slightly, while the losses significantly decrease. Since these are wanted effects, high percentages of silicon would be preferred. However, the mechanical properties such as the ultimate strength, the yield strength and the hardness increase by silicon alloying. These are very unwanted effects, which forbid for the industrial processing [12] [13].

Small concentrations of manganese (reducing the brittleness by removing oxygen from the alloy) and aluminum (nitriding and increasing the scale resistance) can be added (up to 0.5%). Other composites have to be kept very low in order to retain the desired magnetic and mechanical properties, since they can form inclusions in the alloy, that are leading to increased magnetic losses, as can be seen in Figure 1.6 a). In b) the allowable residual carbon content C_R is shown. This allowed content in view of the ageing of the steel alloy is depending
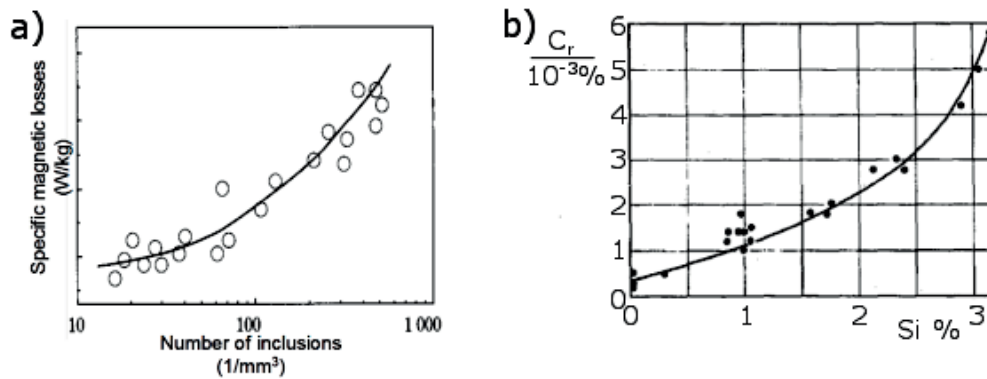
Figure 1.6: a) Influence of the number of inclusions to the magnetic losses [15]. b) Allowable residual carbon content C_R in electrical steels for the same ageing behaviour [12].

on the silicon content. The lower the proportion of silicon is, the less carbon is allowed. For example the carbon content for an alloy with 3 percent of silicon needs to be kept below 0.005%. These restrictions and technical demands result in very complicated and expensive production routines for GRO-electrical steels.

GRO-electrical steel usually has a silicon level of ≈ 3 %. The properties of GRO-steels are optimised in the rolling direction, which is achieved through a very dedicated production routine, including several cold and hot rolling, annealing, pickling and hardening steps [16]. The Goss-orientation (GO), after its inventor Norman P. Goss (patented in 1935)[17], is the only industrial-state grain orientation. Others, such as cube orientation, have not been produced on an industrial scale. The Goss-orientation (Goss-texture) is schematically shown in Figure 1.7. In this Goss-orientation, the crystal orientation relative to the sheet is the [001]-direction parallel to the rolling direction, which is generally the length of the lamination. The plane parallel to the surface is the (110) crystal plane.
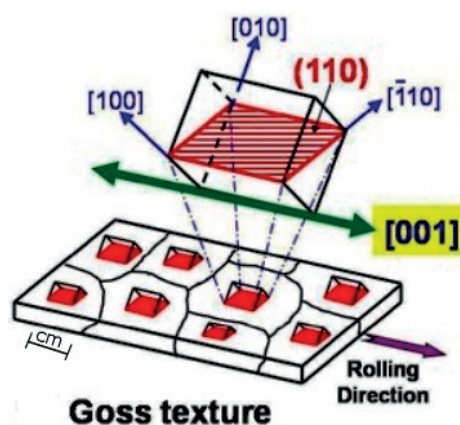
Figure 1.7: Goss-orientation in a steel alloy with [001] parallel to the rolling direction and (110) parallel to the surface [18] for all grains. The crystallographic cubic structure of the steel is shown as a zoom to the atomic scale on top. The crystallographic planes and directions are labeled. In the case of steel a cube edge has the length of ≈ 2.86 Å.
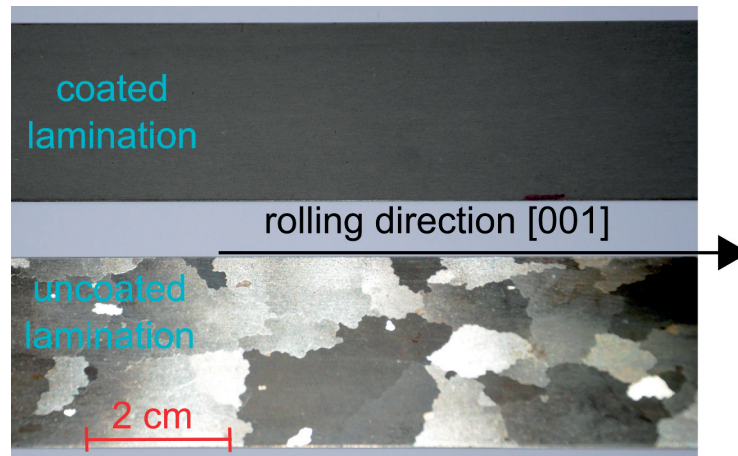
Figure 1.8: Optical photographs of a coated Goss-oriented electrical steel lamination on the top. A second optical photograph of the Goss-oriented electrical steel lamination where the coating was chemically removed is shown in the bottom [20]. Large, centimeter sized grains are visible due to different reflections of visible light for different grains after etching the lamination.

The crystallographic grains in GO-steels grow very large through the various production stages for the development of the texture, giving diameters of up to several centimeters in length. These grains can be made visible by different reflections of visible light after chemical etching a GO-lamination[3] [20]. This is show in Figure 1.8. On the top, an optical photograph of a coated[4] lamination is shown, where no features are visible and the lamination looks homogeneous. The bottom image shows a lamination that was uncoated before taking the photograph and reveals the large elongated grains.

The texture of a steel lamination is a measure of the distribution of crystallographic orientations. Such GO-steels are commonly characterised by the pronounciation of the Goss-texture, also called the sharpness of the texture. This sharpness can be increased up to an orientation deviation of less than 3 ° [21].

Mechanical properties, such as the tensile strength, the tearing strength and the yield point of Goss-oriented steels depend strongly on the degree of texture. Figure 1.9 shows, that the tensile strength as well as the tearing strength decrease with an increasing degree of texture, while conversely the yield point increases [22].

Despite intensive research for more than half a century, there is still no general consent as to the origin of the preferred growth of the Goss-grains. However, it is known that the heredity of Goss orientation in early stages of production plays an important role. Research to understand the evolution of these grains better in industrially processed silicon steels, during the various production and treatment steps, is ongoing [23],[24],[25].

GO-steel laminations are commonly characterised by their magnetic properties along the

---

[3]The samples are provided from ThyssenKrupp. For materials details see Thyssen PowerCore C (C 130-30) in [19].

[4]The coating is glassy magnesium silicate layer
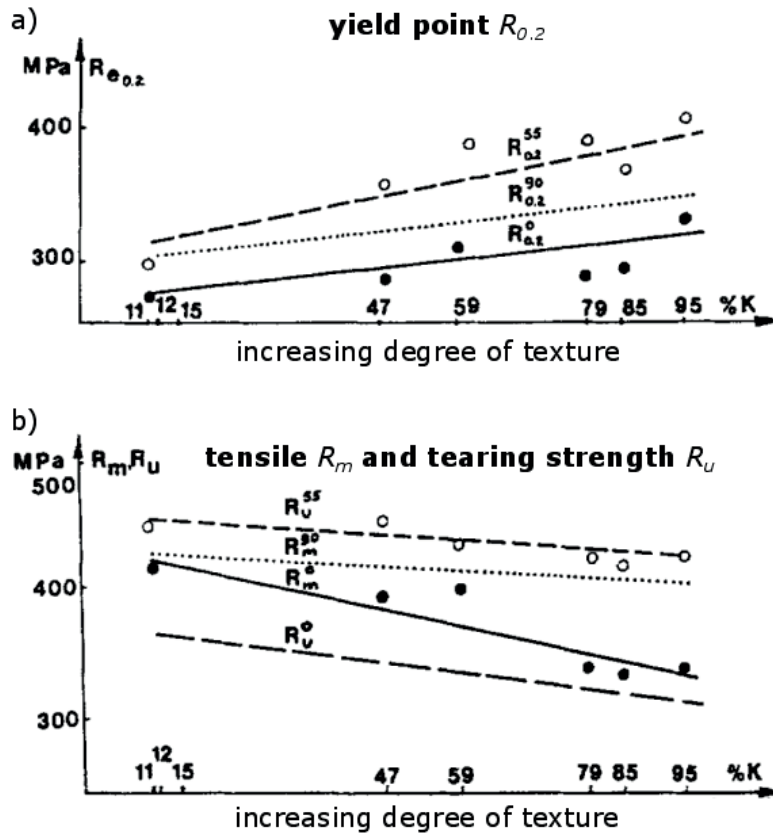
Figure 1.9: Mechanical properties depending on the degree of texture. a) The changes of the yield point $R_{0.2}$ with increasing degree of texture. Increasing degree of texture leads to an increased yield strength. In b) the tensile strength R_m and tearing strength R_u are shown, depending on the degree of texture. Both decrease with increasing degree of texture. Adapted from [22].

rolling direction only. The <001> type crystal directions are the easy axis [5] of magnetisation that a cubic crystal like iron-silicon (FeSi) provides and in a GO-steel they are aligned in rolling direction. Figure 1.10 shows the magnetisation behaviour in different directions of a GO-steel lamination. The magnetisation along the <100> axis is saturated nearly instantaneously when applying a magnetic field compared to the <110> or the <111> direction. Consequently Goss-orientated steels are characterised along their magnetic easy direction only.

For the purpose of characterising GO-steel laminations, either the power losses P (difference between input and output power) or the saturation polarisation J_s are used. Indeed, instead of J_s often the saturation magnetisation B_s [6] is similarly used. These two quantities are connected via the following formula.

$$J_s = B_s - B_v \tag{1.1}$$

---

[5] energetically favorable direction of spontaneous magnetisation
[6] maximum magnetisation attainable due to applied field H
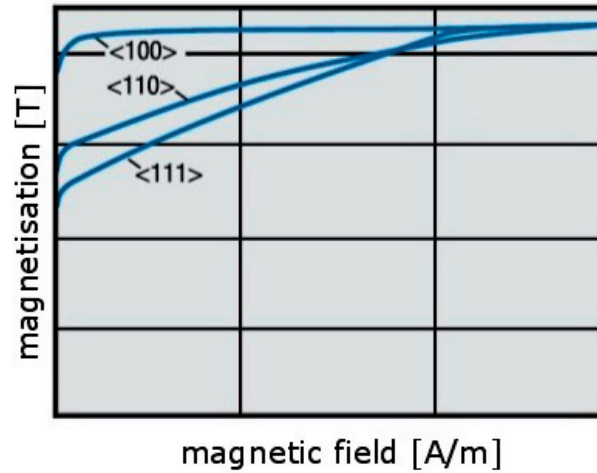
Figure 1.10: Magnetisation behaviour of a GO-steel lamination along different crystallographic axis. The <100> axis is the magnetic easy axis of the cubic Fe-Si crystall [26].

with the magnetisation in vacuum B_v.

To obtain these characterising measurement parameters P or B_s/J_s, individual sheets are investigated by the internationally standardised Epstein frame method [27]. An Epstein frame is built similar to a transformer and also called a four arm-measuring coil system. Such an Epstein frame consists of several coils which are serially connected. An outer coil with N_1 windings for the magnetisation and an inner coil with N_2 windings for measuring the flux density via the induced Voltage U are combined in one part on every arm. The sample to be investigated has to be part of the system, which is achieved by putting the lamination into the coils. Figure 1.11 a) shows an optical photograph of such an Epstein frame, where the hole for the inserted sample can be seen. In b) the frame is schematically illustrated. The coils, wound around the sample are shown and the magnetic length l_m of the frame is included. This length is fixed in the Epstein geometry to 940 mm.

With the knowledge of the applied current I, the windings of the magnetisation coil N_1 and the magnetic length l_m, the magnetic field can be calculated using

$$H = \frac{N_1 \cdot I}{l_m}.$$ (1.2)

Measuring the induced voltage U, the magnetic flux density B can be derived by:

$$B = \frac{1}{N_2 \cdot A} \int U dt$$ (1.3)

with the cross-section of the sample A and the windings of the measuring coil N_2. Ramping the magnetic field H and recording the magnetic flux density B, a magnetic hysteresis loop (B-H-loop) can be recorded. While the saturation magnetisation B_s, the saturation value of

9
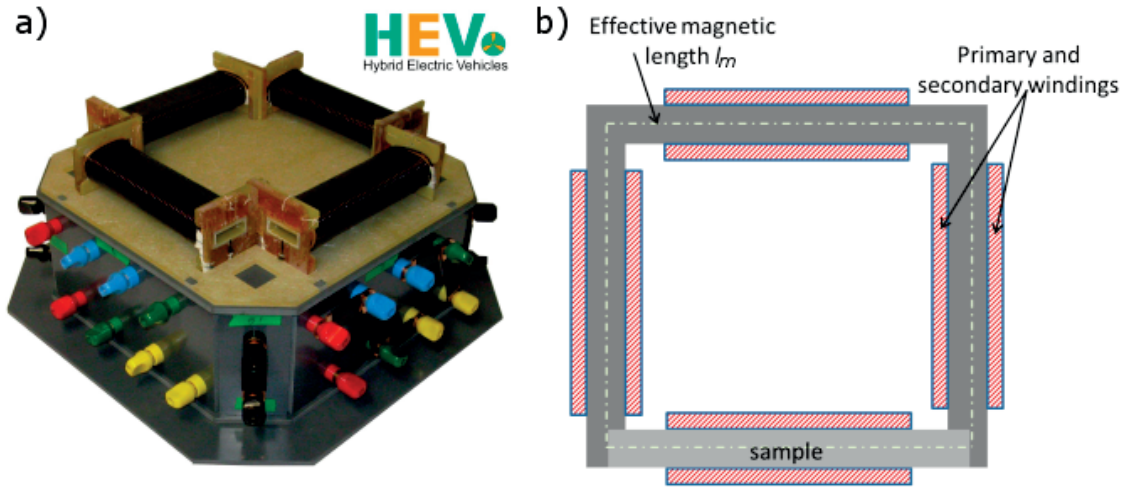
Figure 1.11: a) Epstein frame for magnetic characterisation measurements of P, B_s or J_s. Samples are introduced into the opening of the coils. The magnetic circuit has to be closed by inserting at least four laminations [28]. b) Schematic drawing of the Epstein frame geometry with windings and effective magnetic length. The sample is mounted such that the sample itself closes the magnetic circuit.

the magnetic flux density, is directly obtainable, the power losses P are given in [29] by

$$P = \frac{N_1}{N_2} \cdot P_m - \frac{(1.111 \cdot |U|)^2}{R_i} \tag{1.4}$$

with R_i being the resistance of the Epstein frame and P_m the power in watts ($P = U \cdot I$). While measuring the power losses P by means of a watt-meter method, the Epstein frame behaves exactly like a transformer.

The hysteresis losses P and saturation magnetisation B_s of different grades of the GO-steels are characterised and can be compared by the Epstein method. By way of example, in Figure 1.12 a) a hysteretic B-H loop of a GO-steel lamination (C 130-30)[7] is shown. The zoom for the x-axis of this loop is shown in b) and the saturation magnetisation B_s, the remanent flux B_r and the coercive field H_c can be directly obtained. The losses are proportional to the area included in the B-H loop marked by the blue dashed area.

The magnetic flux density can be increased in GO-steel laminations by 30% in the rolling direction due to the sharp texture, while the magnetic saturation is decreased only by 5% [30]. Furthermore, the increase of the average crystal size, concomitant by the Goss-grain growth, decreases additionally the hysteresis losses [31].

The table in Figure 1.13 shows values for losses and saturation polarisation of different grades of GO-steel laminations. The saturation polarisation J_s for 800 A/m applied field J_{800} is exceptional for GO-steels, with a maximum value of 1.83 T. Hysteresis losses are small: At a thickness of 350 μm the losses for 50 Hz applied frequency of the field P_{50} are only 0.93

---

[7]The number 130 stands for the max. losses of 1.3 W/kg at 60 Hz and 1,7 T; The digit 30 is representing the thickness of 300 μm
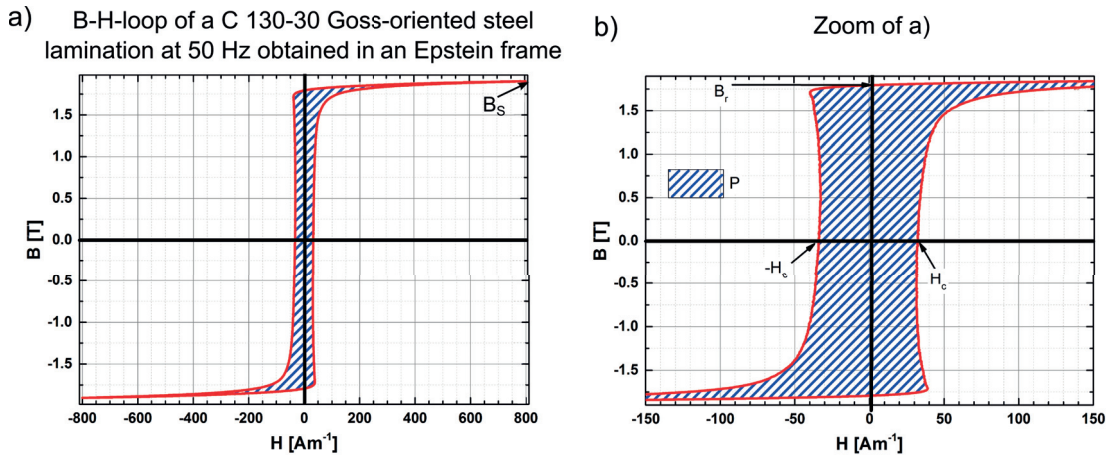
Figure 1.12: a) Hysteretic B-H-loop of a Goss-oriented electrical steel lamination (C 130-30) as it is obtained at 50 Hz using the Epstein method. b) Zoom of the loop. The saturation magnetisation B_s, the remanent flux B_r and the coercive field H_c are included. The blue dashed area is proportional to the losses P which can be calculated using equation 1.4.

W/kg (for grade C 140-35 from Figure 1.13). The trend of increasing losses but also increasing saturation polarisation with increasing thickness of the individual lamination can be seen in the table. This is mainly due to the increasing eddy-currents in thicker sheet (see following section). In addition, the different losses for different grades, providing the same thickness, can be seen [32]. Grade C130-30 is marked by a red box, because this grade is investigated in the experimental part of this thesis.

GO-steels are commonly not characterised by their relative permeability μ_r because the permeability is depending on where it is measured in a B-H-loop, since it is the slope of the curve ($\mu_r = \frac{dB}{dH}$). Nonetheless it is an important property, since the permeability is the ability of a material to conduct magnetic flux. The exceptional permeability of GO-steels, which can

grade	thickness	maximum hysteresis losses				typicall hysteresis losses				saturation polarisation	
		1.5 T	1.7 T	1.5 T	1.7 T	1.5 T	1.7 T	1.5 T	1.70	800 A/m	800 A/m
		50 Hz	60 Hz	50 Hz	60 Hz	50 Hz	60 Hz	50 Hz	60 Hz	min. T	typ. T
		W/kg	W/kg	W/lb	W/lb	W/kg	W/kg	W/lb	W/lb		
C 110-23	0.23	0.73	1.10	0.44	0.66	0.69	1.06	0.41	0.64	1.80	1.83
C 120-23	0.23	0.77	1.20	0.46	0.72	0.73	1.15	0.44	0.69	1.78	1.83
C127-23	0.23	0.80	1.27	0.48	0.76	0.77	1.24	0.46	0.74	1.75	1.82
C 120-27	0.27	0.80	1.20	0.48	0.72	0.78	1.16	0.47	0.70	1.80	1.83
C 130-27	0.27	0.85	1.30	0.51	0.78	0.82	1.24	0.49	0.74	1.78	1.83
C 140-27	0.27	0.89	1.40	0.53	0.84	0.86	1.32	0.52	0.79	1.75	1.82
C 130-30	0.3	0.85	1.30	0.51	0.78	0.83	1.20	0.50	0.72	1.80	1.83
C 140-30	0.3	0.92	1.40	0.55	0.84	0.87	1.26	0.52	0.76	1.78	1.83
C 150-30	0.3	0.97	1.50	0.58	0.90	0.91	1.32	0.55	0.79	1.75	1.82
C 140-35	0.35	1.00	1.40	0.60	0.84	0.93	1.33	0.56	0.80	1.80	1.83
C 160-35	0.35	1.05	1.50	0.63	0.90	0.97	1.40	0.58	0.84	1.78	1.83
C 165-35	0.35	1.11	1.65	0.67	0.99	1.01	1.47	0.61	0.88	1.75	1.82

Figure 1.13: Table of maximum hysteresis losses, average hysteresis losses and saturation polarisation for different grades and thicknesses of Goss-oriented electrical steel grades [32]. The grade that is used for the experiments in this thesis (C 130-30) is marked by a red box.

reach up to several ten-thousands of H/m, in combination with the small hysteresis losses and the high saturation polarisation, makes GO-steel laminations well-suited for the transport of magnetic fluxes in industrial applications.

The measurements using the Epstein method, result in well-known magnetic B-H-loops which reveal global magnetic properties. Hereby neither a locally resolved information nor any information about the underlying domain structure can be obtained. The investigation of magnetic domains is, not exclusively but mostly, performed by Kerr microscopy. For this, surface sensitive, technique the protective coating, which was already shown in Figure 1.8 a), needs to be removed. The significant impact of the coating removal to the magnetic properties of a GO-lamination will be investigated in the following section.

1.1.3   Impact of the protective coating

The driving force of all ongoing development in GO-steels is the reduction of losses and accordingly the increased efficiency in industrial application. To decrease eddy-current losses in a transformer, GO-steel laminations have to be insulated from one another. This is due to transformer cores being built from stacked laminations and the eddy-current losses are thickness dependent [33]:

$$P_{ed} = \frac{\pi^2 \cdot d^2 \cdot {B_0}^2 \cdot f^2}{6 \cdot \rho_{el} \cdot \gamma} \tag{1.5}$$

for the magnetic induction B_0, the frequency f of the magnetic AC-field, the electrical resistivity ρ_{el}, the density of the material γ and the thickness of the sheets d. These thickness dependent losses are illustrated in Figure 1.14, where the eddy-currents are schematically drawn for a solid block in a) and for a core built of stacked sheets with an insulating layer between each sheet in b).
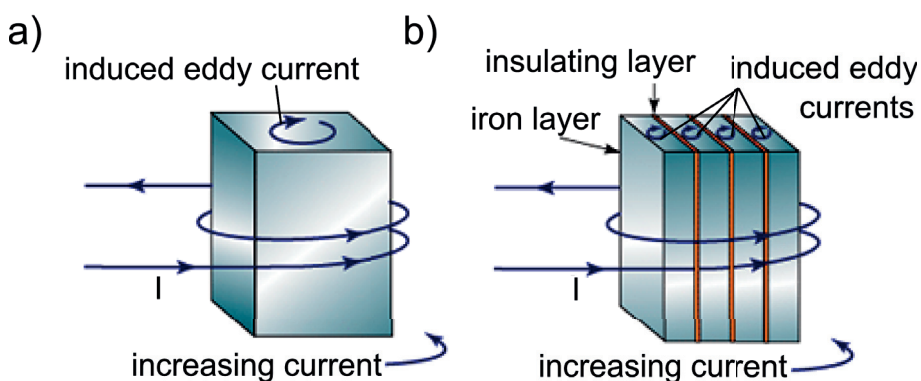
Figure 1.14: Schematic drawing of eddy-currents in a) a massive iron block and b) in stacked iron sheets. By using equation 1.5, the decreased eddy current losses due to the stacked sheets instead of a massive block becomes obvious [34].

Due to the loss reduction by isolating the individual laminations from another, GO-steels are produced almost solely in a coated state. A measure for the type of coating together with the form of the sheet is the stacking factor. Since each insulating layer reduces the effective magnetic volume inside a transformer core the effective density of magnetic material in a transformer core is expressed by this measurable relative to a massive block. Accordingly the value of the stacking factor is always less than 1. It decreases in the case of non-uniform thicknesses of the stacked sheet, increasing thickness of the coating and decreasing thicknesses of the individual sheets. A variety of coatings are available, and enormous effort has been expended on the investigation of coatings and their influence on the magnetic performance of electrical steels [35],[36],[37],[38]. Laminations may be coated by organic varnishes, but these will not survive further treatment such as stress-relief annealing. Consequently, GO-steels are often coated by a MgO powder before they are high temperature annealed[8]. This powder, together with the silicon oxide (SiO_2) already solved in the steel, forms a glassy magnesium silicate layer. Usually these magnesium silicate layers are thin. A coating thickness of 2 to 5 μm provides good electrical resistance and a high stacking factor [40].

This type of coating not only acts as insulator, but also tends to put the steel in tension when it is cooled by having a smaller coefficient of thermal contraction. The residual tensile stresses, which are largely longitudinal, lead to a further preference of the magnetic easy axis in rolling direction. The magnetic structure with domains parallel to the rolling direction divided by 180 ° walls is even more favorable, and hence the core losses decrease further [41]. The stresses, induced by the coating can be seen in Figure 1.15. In a) three laminations are shown, coated only on the top side. Due to the coatings smaller coefficient of thermal contraction the laminations bend when they are cooled down. In b) it is schematically illustrated, how the layer can substitute an external force for the application of an tensile stress to the steel sheet. Also, resistance to corrosion, rust and mechanical strokes is ensured by the coating, as it is acting as a lubricant during cutting processes. A further advantage of the coating is the reduction of transformer noise. The transformer "hum" is reduced due to the magnetostriction being remarkably low in the rolling direction, which is the dominant effect of the noise generated
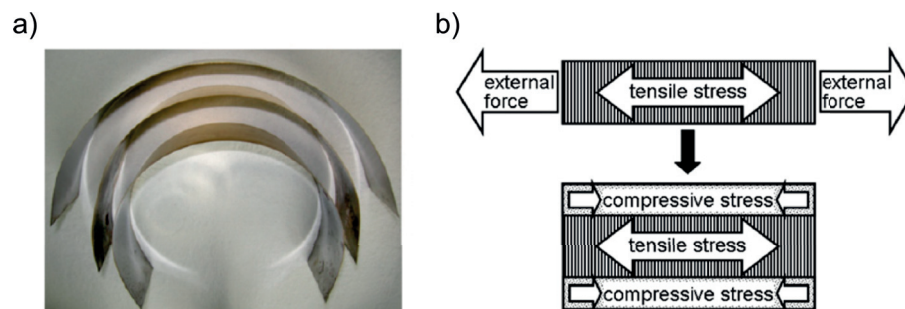
Figure 1.15: Tensile stress applied by the coating. a) Optical photograph of three sheets, coated on one side only (layer on the convex sides). b) Illustration of the basic idea: a tensile stress in the GO-steel laminations (reducing power losses) could be applied by external forces as well as by a layer showing compressive stress [38].

---

[8]Further information about different coating can be found for example in [39]
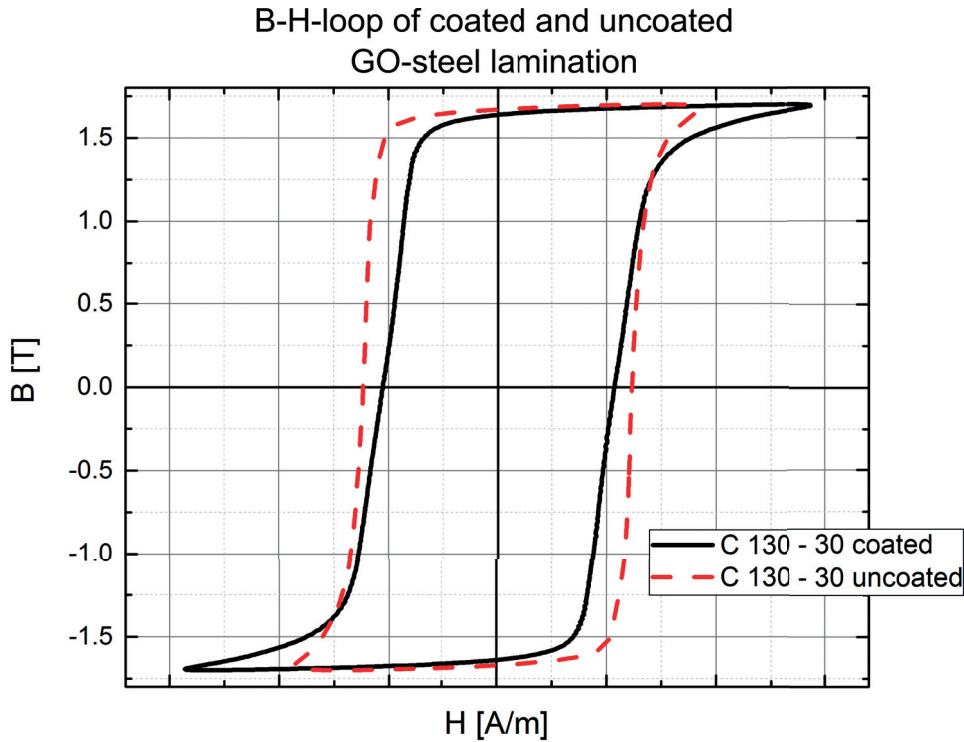
Figure 1.16: B-H-loops of a C130-30 GO-steel lamination, in the coated state (solid line) and in the uncoated state (dashed lines). Losses P are proportional to the area included by the hysteresis loop. Consequently the uncoated sheets will yield higher losses.

in transformer applications. In Figure 1.16 the influence of the coating is investigated by taking a B-H hysteresis loop of a lamination with and without coating (Epstein method). The coating can be removed by chemical etching of the lamination [20]. In the graph in Figure 1.16, the magnetisation behaviour of one exemplary chosen C130-30 GO-steel laminations is illustrated. The solid line represents the coated sheet, while the dashed line represent the same laminations but in its uncoated state. The area imbedded by the hysteresis loop is significantly larger for the uncoated state. As already mentioned previously, this area is proportional to the losses P of such a lamination. Consequently the losses are remarkably reduced by the coating. The effect of tensile stress on the losses in a single Goss-crystal was investigated by Yamamoto and Nozawa [42] and are consistent with the effects found in the measurement of a whole lamination. The application of tensile stresses leads to a decrease in total losses, as can be seen in the graph in Figure 1.17. The applied stress (in $\frac{kg}{mm^2}$) is plotted versus the total losses (in $\frac{W}{kg}$). The reduced losses due to tensile stresses are clearly visible. For the highest permeability the losses are almost bisected. The effect is more pronounced the higher the permeability of a grain is. This illustrates the significant impact of stresses in general but also the stress applying coating on GO-steel laminations, which are designed to allow for high permeability.
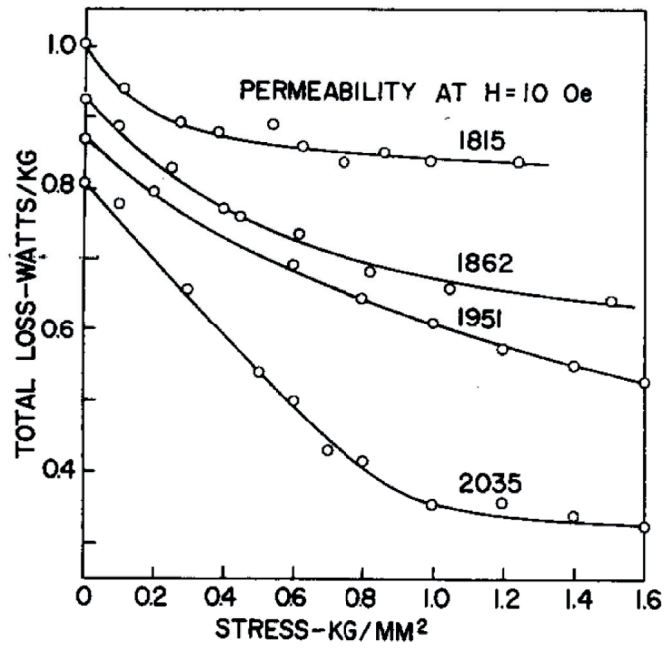
Figure 1.17: Decreasing losses for increasing applied tensile stresses onto a single Goss-grain. The higher the permeability gets, the more pronounced the effect is [42].

1.2 Motivation of this thesis

The conventionally performed characterisation measurements of GO-steels result in magnetic B-H-loops and deliver global magnetic properties, such as losses, saturation magnetisation and permeability. Neither local resolved information nor any information about the underlying domain structure can be obtained, although the magnetic domain structure of the material determines its global properties and is fundamental for its performance. Even the multitude of techniques for magnetic domain investigations, such as Kerr microscopy [43], Bitter technique [44], Lorentz microscopy [45], electron holography [46] or photo-emission electron microscopy [47] are surface sensitive and cannot access the internal volume domain structure. A further drawback of these techniques is the fact that the coating of the steel lamination needs to be removed. This has been shown to have a significant influence on the magnetic properties [22][38][48] but also to the underlying magnetic domain structure [49][50].

To overcome the limitations of these well-established techniques, neutrons can be used, since they can easily penetrate centimeter thick metallic samples and they carry an intrinsic magnetic moment μ_N. Therefore neutrons are able to interact with magnetic structures. However neutron techniques have their own challenges in the image quality or the exposure time. Due to the neutrons spin interaction with the local magnetisation in magnetic samples [51] several magnetic observation techniques using neutrons have been developed. Single-crystal interferometry base techniques [52][53][54][55] as well as crystal analyser-based topography techniques [56][57] have their practical limitation in the very small neutron beam divergence (only a few mdeg) and the small energy spread (a few meV), resulting in inefficient setups with exposure times of several hours per image. Neutron depolarisation analysis [58][59] are limited in the sense of an imaging approach, by the large sample-to-detector distances (≈ 0.5 m) due to geometrical requirements, that compromises the resolution. Experiments using the neutron grating interferometry technique, developed at the Paul Scherrer Institut (PSI), were first performed in 2005 [60]. A neutron grating interferometer (nGI) is able to probe samples with the purpose of obtaining local magnetic information from the volume of the sample. Thus the nGI technique allows for the study of bulk magnetic domain wall structures and their behaviour in GO-steels in the so called dark-field image (DFI) spatially resolved in two [61][62][63] and even in three dimensions [64]. The images of the volume magnetic domain structure obtained by the nGI technique are of non-destructive nature and provide a centimeter sized field-of-view with a spatial resolution down to several tens of micrometer.

The new aspect in this thesis, is the response of magnetic domain walls under the influence of various external influences. In particular, the magnetic domain structure response to externally applied magnetic fields, both static DC- and also alternating, dynamic AC-fields is studied. Additionally the influence of mechanical forces to the volume magnetic domain structure is investigated. The exact, spatially resolved influence of the protective coating to the local domain structure is visualised in the volume as well. Correlative measurements, such as magneto-optical Kerr microscopy, Faraday imaging, small-angle neutron scattering and

Laue X-ray diffraction are performed to compare and sustain the DFI findings.

These experiments and systematic studies allow on the one hand for the experimental proof of magnetic volume domain formation, while on the other hand new insights in the magnetic domain behaviour can be gained, that may lead to further development of the GO-steel sheets as components of transformer cores, and to increased efficiency in industrial transformer applications.

2 Basics

The objective of this chapter is to explain the bulk magnetic domain structures that can be found in GO-steels. It is derived, how the macroscopic magnetisation behaviour and the magnetic properties are fundamentally influenced and determined by the internal domain structures and how they are investigated. Furthermore, the basics of attenuation based neutron imaging are explained and the wave optical description of neutrons interaction with matter is given. In the end, the principle of neutron grating interferometry is illustrated and it is shown, how the data acquisition and image processing is performed.

2.1 Magnetic domain structures in Goss-oriented electrical steels

The underlying internal structure of magnetic domains and domain walls in GO-steels is essential for their magnetic behaviour and performance. Without easily displaceable domain walls, providing the necessary permeability, modern electrical machines would simply not work. For the investigation of local magnetic domain structures in GO-steels, generally the
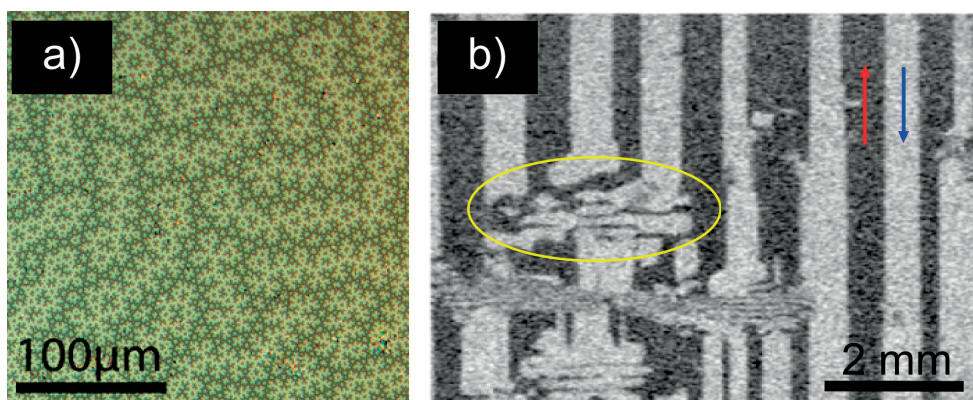

Figure 2.1: Exemplary Kerr microscopy images of magnetic domains. a) Kerr image of the fractal domain pattern in $Nd_2Fe_{14}B$ [65]. b) Single shot domain image (Kerr) from a Goss-oriented electrical steel surface [66]. Vertical elongated domains with "'up"' and "'down"' magnetisation (marked by the arrows) and supplementary domains (marked by the yellow circle) can be seen.

magneto-optical Kerr effect (MOKE) [67] [68] [69] is used, which provides information about the magnetic domain structures at the surface of a sample.

Figure 2.1 shows two images obtained by Kerr-microscopy[1]. The Kerr image in a) shows an exemplary domain pattern. This is an image of a fractal domain pattern in $Nd_2Fe_{14}B$ with a resolution in the μm range. The Kerr microscopy image in b) depicts the magnetic structure on the surface of a GO-steel lamination. Several domains inside one grain are visible. Vertical elongated domains with "'up"' and "'down"' magnetisation (marked by the arrows) and supplementary domains (marked by the yellow circle) can be identified [66].

Using Kerr microscopy techniques, locally resolved images of the domain structure at the surface are achievable with high resolution in space and time, but the internal volume domain structure cannot be investigated directly. This is due to the interaction volume of the light being limited to the surface or a small penetration depth of several nanometers. Furthermore, Kerr microscopy is limited due to the high resolution achievable, in the field of view to some millimeters. The sample requirements, such as the need for polishing, can hinder investigations and are further drawbacks. In the case of GO-steel sheets for example, the already mentioned coating needs to be removed before polishing and only after that, the investigation can be performed. This will result in an altered magnetic structure (compare 1.1.4) that is investigated.

As seen in the Kerr image in 2.1 b) the internal magnetic domain structure in GO-steels can be divided into two different kinds of magnetic domains: Wide **basic domains** (blue and red arrow in Figure 2.1) in ideally oriented grains, on the one hand, and **supplementary domains** in slightly misoriented grains or at grain boundaries on the other hand [41] [70].

2.1.1 Basic volume domains in highly oriented grains

The basic magnetic domain structures of GO-sheet are slab-like volume domains that are magnetised in 180° parallel or antiparallel to the magnetic easy axis, which is the [001]-axis. A special feature in GO-steels (also in other positive anisotropy cubic materials) is the domain walls, which are oriented in the (100) or the (010) plane, forming a "zigzag-shape", as visible in the schematic in Figure 2.2 a). Given the energy of a domain wall is proportional to the length of the wall, one would expect the shortest possible domain wall to be realised, which is perpendicular to the surface (110). However in GO-steels the energy for a domain wall in the (100) and (010) plane is the lowest. The balance of these two energy reductions lead to the shortest domain walls (110) tending to rotate towards the above mentioned orientation and "zigzag-shape" [70]. In Figure 2.2 a) the basic domains with the magnetisation, marked by arrows, pointing along and opposed to the [001] direction and the gray domain walls, oriented along the [010] and [100] direction, are shown. The SEM type II[2] image in Figure 2.2 b) shows the surface magnetic domain structure in such a GO-steel in the top view. These domains form

---

[1]The Kerr microscopy uses the rotation of the polarisation plane of a linearly polarised light beam for the reflection at a solid surface with a magnetisation

[2]Backscattered electrons are used for the contrast formation. Energy-dependent penetration depth from 1 μm up to $20\mu m$
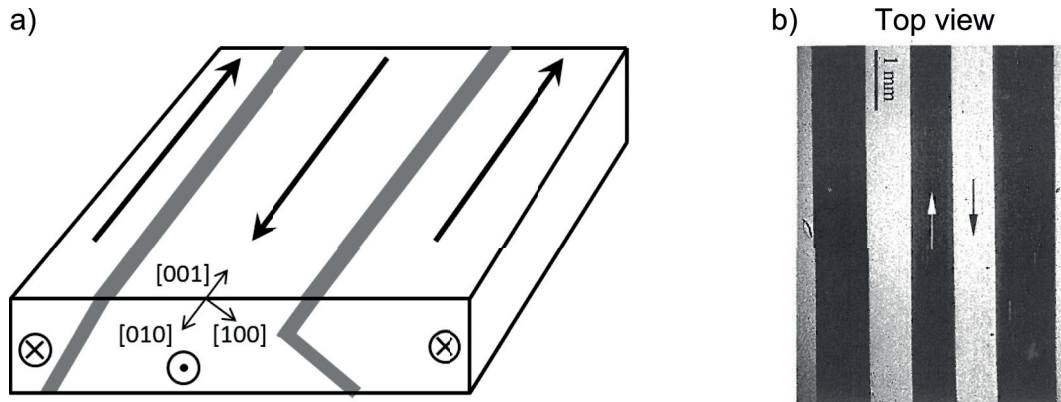
Figure 2.2: Basic domain structure in Goss-oriented electrical steels. a) Schematic of basic magnetic domains and their domain walls in a GO-steel. Magnetisation pointing in rolling direction ([001]) and domain walls along the preferred orientation along the [010]- and [100]-axis. b) Electron backscattering image of an ideally oriented grain in an GO-steel, showing wide volume domains (up to several mm in width) with magnetisation pointing in ± [001]-direction [70].

the basis for the magnetic flux transport in the sample, hence they are called **basic domains**.

2.1.2 Supplementary domains in slightly misoriented grains

However perfectly oriented grains, with a magnetic easy axis in the surface, display only simple magnetic domain patterns. The patterns get much more complex in slightly misoriented grains [70] [71].

The misorientation of a grain is characterised by the angle between the surface and the nearest magnetic easy axis ϑ_s which is delineated in Figure 2.3 a) and b) as the angle between the easy
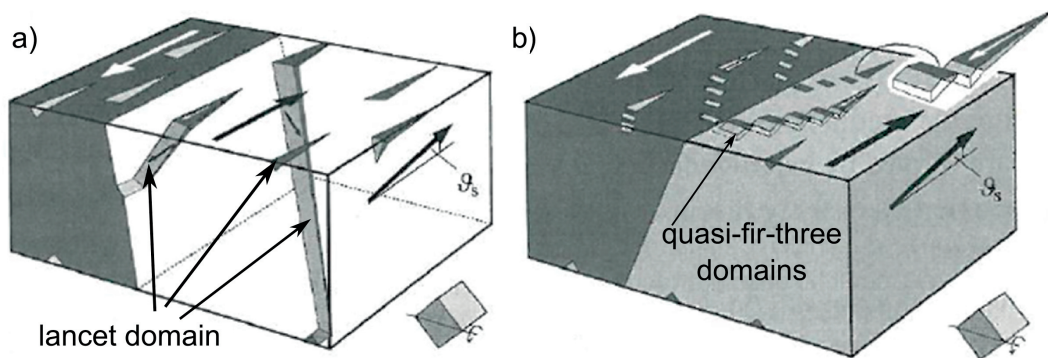
Figure 2.3: Two possible supplementary domain patterns in GO-steels [70]. a) Sketch of two basic domains with supplementary lancet domains as they can be observed in a misoriented (110) crystal. The flux is transported to the opposite surface by internal transverse domains. b) Two basic domains with an alternative quasi-fir-tree pattern. The flux is transported to the adjoining domains, parallel to the surface.

axis and a line parallel to the surface. Two different domain patterns that exist in misoriented grains in GO-steels are schematically shown in Figure 2.3. In a), standard lancet domains are present, while b) depicts a quasi-fir-tree pattern of domains. In a), the magnetic flux is transported to the opposing surface or the neighboring domain by internal supplementary transverse domains [70]. In b), the flux is transported parallel to the surface to the next domain. The underlying principle of both patterns is the introduction of small supplementary surface domains, which collect the flux. Without these supplementary domains the magnetic flux would escape from the surface leading to energetically unfavorable magnetic stray fields. Thus the effective size of domains at the surface is decreased and the flux that needs to be diverted is distributed onto these supplementary domains [70]. Due to the fact that these compensating domains are superimposed on the basic domain structure, these domains are called **supplementary domains**.

The most frequently occurring supplementary patterns are lancet patterns as shown in Figure 2.3 a). These patterns tend to transform into quasi-fir-tree patterns as the crystals get thicker. Note, that the strength of the misorientation (value of ϑ_s) determines the scale and amount of the supplementary pattern, not the character [72]. Since the supplementary domain pattern reduces stray field energies at the expense of additional domains near the surface, there is a minimum value for the misorientation angle ϑ_s, giving rise to the generation of the supplementary pattern. This value evolves from the energy balance between domain wall generation and stray field reduction and is dependent on the sample thickness t. Therefore, as a criterion for the presence of a supplementary domain pattern, a characteristic length t_0 is calculated using the exchange constant A, the anisotropy constant K and the stray field constant K_d:

$$t_0 = \frac{\sqrt{A \cdot K}}{K_d \, sin^2(\vartheta_s)}. \tag{2.1}$$

This characteristic length is compared to the samples' thickness t. If the thickness of the sample is larger than this characteristic length ($t > t_0$), the basic domain structure is completed by the generation of a supplementary domain pattern. If the thickness is smaller, the stray field is reduced by rotating the magnetisation of the basic domain parallel to the surface, against the anisotropy force [70]. Note, that supplementary domains are only formed for misorientation angles up to $\vartheta_s \leq 10°$, while larger misorientation angles lead to fractally branched surface domain structures.

However, supplementary domain structures can arise for reasons other than misoriented grains. Internal defects, stresses or grain boundaries can also cause a rich variety of additional domain structures to occur [70].

In Figure 2.4 some of these impacts are shown. The image in Figure 2.4 a) reveals isolated lancet domains and small segments of basic slab domain walls, which form a large angle with the preferred axis (enlarged on the right). Both phenomena indicate internal transverse domains (compare Figure 2.3 a)) that are likely connected and caused by inclusions inside the sample. The supplementary domain pattern in Figure 2.4 b) is due to stresses inside the material. Here, thermal stresses were artificially introduced by laser scribing through
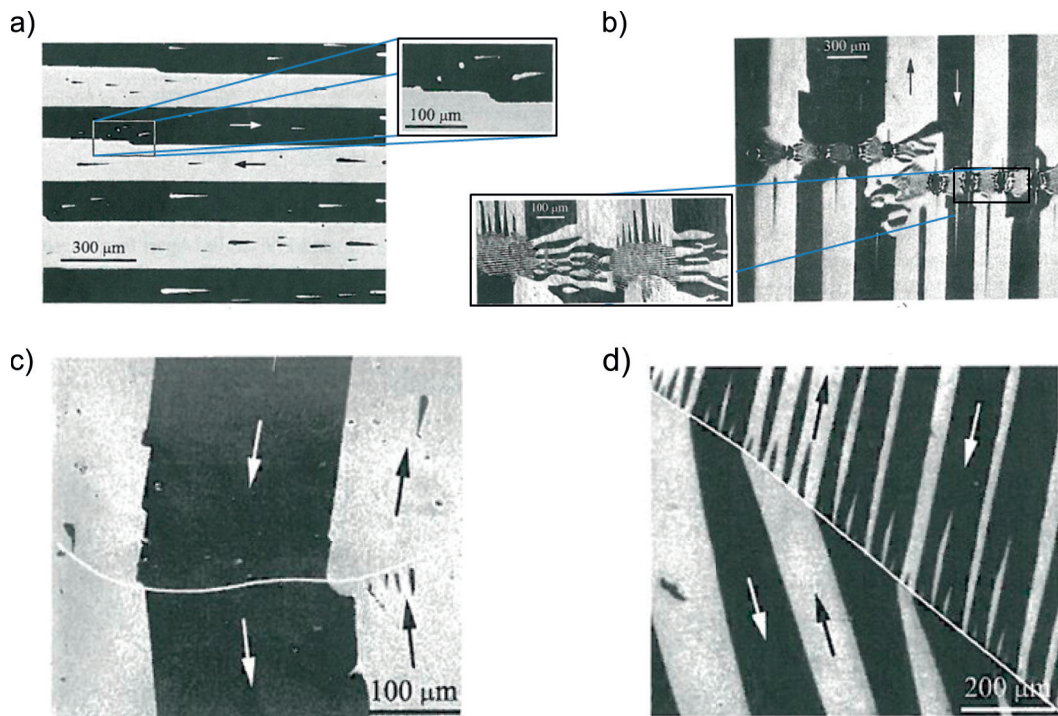
Figure 2.4: Supplementary domains in a GO-steel lamination caused by different impacts [70]. In a) slab-like domains on a largely undisturbed Goss oriented (110) grain, showing additionally lancet domains and small segments in the basic domains (enlarged on the right) due to internal inclusions, are visualised. In b) a SEM type II contrast image of a supplementary domain structure generated due to artificially induced thermal stresses (laser scribing) is shown. The zoom on the left is a high resolution Kerr image of the same region. c) and d) each illustrate a grain boundary providing a different magnetic charge. While the boundary in c) allows for continuous basic domains over the boundary, the boundary in d) introduces supplementary dagger-shaped domains.

the protective coating [73] [74]. This image is obtained by SEM type II contrast through the coating, while the enlarged image (left) is a Kerr microscopy image. In the Kerr image, the small domain width is visible even though the domain structure has been quantitatively changed by removing the coating, which was required for the Kerr investigations.

Grain boundaries can also act as source of supplementary domains. This is shown in Figure 2.4 c) and d). The delineated white line marks the grain boundary while arrows mark the magnetisation of basic domains. The magnetic charge, which is determined by the tilting angle and the stress state of the grain boundary, defines if basic domains can be continued as shown in c) or different types of supplementary domain structures can be generated as shown in d) [70] [75] [76]. The dagger-shaped domain pattern in d) is a typical pattern to be found at grain boundaries in GO-steels.

2.2 Magnetisation behaviour of ferromagnetic Goss-oriented steels

Two processes are responsible for the magnetisation of a GO-steel on the domain level. Either the domain walls start to move or the magnetisation of the domains is rotated in response to an applied magnetic field [70] [77]. Already in 1949 an experiment has been performed by Williams and Shockley [78] where they could connect the motion of domain walls directly with the magnetisation of the sample. Goss-oriented steel crystals were magnetised and at the same time they observed the position of a domain wall using a bitter[3] decoration technique [79]. A direct, linear relation between the magnetisation and the domain wall position was observed.

In another experiment, performed by G.L. Houze Jr. in 1967, the domain wall motion during magnetisation was investigated in a GO-steel lamination using Kerr microscopy [69]. Here, the same linear dependence could be shown.

This domain wall magnetisation behaviour holds for samples, where the domains' magnetisation is pointing only in the direction of the applied field or opposite, like the basic domain structure in GO-steels. Applying a magnetic field to such a sample causes the domain walls to move so as to increase the size of domains whose magnetisation is lying parallel to the applied field, at the cost of the sizes of domains whose magnetisation is opposing the field. This behaviour can be explained by the Zeeman energy E_{Ze}, which is the energy arising from the interaction of a magnetic domain with an externally applied magnetic field [80]:

$$E_{Ze} = -\mu_0 \int_V \vec{M} \cdot \vec{H_{ext}} dV \tag{2.2}$$

Therefore, the Zeeman energy is proportional to the negative of the cosine of the angle β between magnetisation of the domain M and the externally applied field H_{ext}. In Figure 2.5, the angle β can be seen. Here, domains with their magnetisation oriented parallel to the applied field reduce this energy, while domains with their magnetic field oriented opposite to the applied field increase the Zeeman energy. This process is schematically visualised in Figure 2.5 a). The top part of the image shows a sample with two antiparallel magnetised domains without an external field. In the bottom part of Figure 2.5 a), the externally applied magnetic field H leads to a growth of the domain parallel to H ($\beta = 0°$) on the cost of the domain which is magnetised in the opposite direction ($\beta = 180°$).

If magnetic domains are perpendicular to the applied external field, the magnetisation M of the domains will rotate. This is schematically shown in Figure 2.5 b). The upper scheme shows the domain state for two antiparallel magnetised domains without an external field. On this occasion, the field is applied in perpendicular direction ($\beta = 90°/-90°$). In the bottom sketch, the magnetisation of both domains is rotated by 45° due to the applied field. The rotation angle depends on the strength of the applied field H. If domains with magnetisation directions between parallel and perpendicular are present, like in supplementary domain structures, both, the domain wall motion and the magnetisation rotation, play a role.

---

[3]Magnetic colloid material is drawn to the sample. An arrangement at the magnetic field gradients allows for the domain visualisation by electron or optical microscopy.
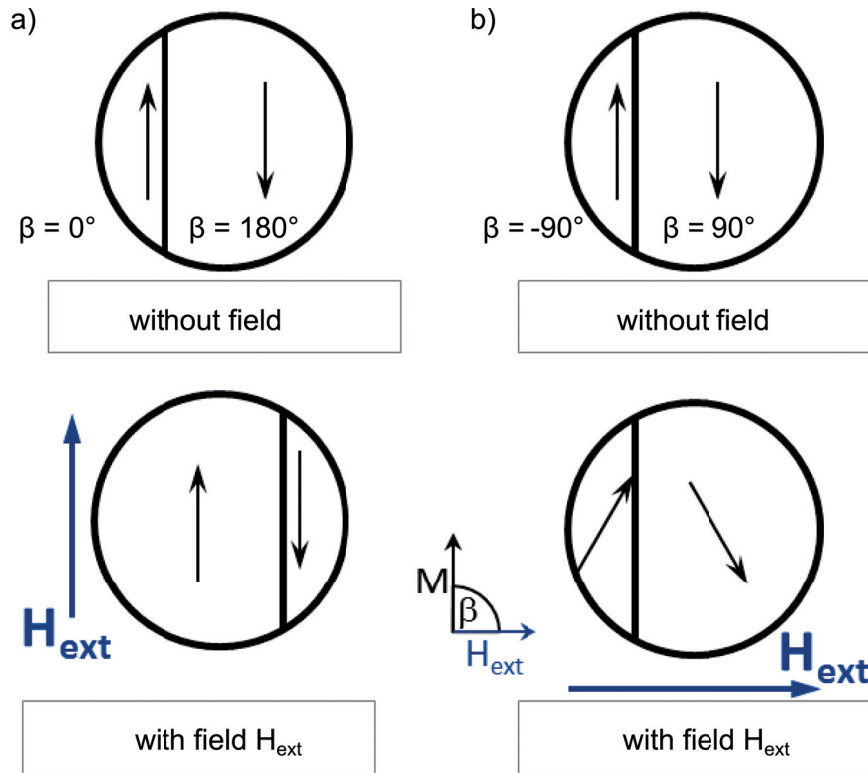
Figure 2.5: Two different processes of magnetisation. In a) a schemtical of magnetisation by domain wall motion is shown. Domains with magnetisation M parallel ($\beta = 0°$) or antiparallel ($\beta = 180°$) to the applied field H grow or shrink by domain wall motion. In b) magnetisation by domain magnetisation rotation is schematically illustrated for domains with magnetisation M perpendicular ($\beta = \pm 90°$) to the applied field H_{ext}.

Starting to magnetise a realistic sample, both processes happen at the same time and cannot be sharply distinguished. Although a rough separation is shown in Figure 2.6 and can be described as follows: Domain wall motion is the main process up to about the "knee"[4] of the magnetisation curve B_k; from there to saturation magnetisation M_s, rotation predominates. In the region above the knee, work must be done against the anisotropy forces (magnetisation is rotated out of the magnetic easy direction) and a large increase in the applied field H is required for relatively small increases in the magnetisation M [81].

Using the Epstein technique, described in the previous chapter, it is possible to reveal global magnetic properties and global characterisations of electrical steels. By the use of Kerr-microscopy, magnetic domain structures at the surface can be analysed with a high resolution in space and time. Several other techniques exist (decoration, electron microscopy techniques, magneto-optical techniques, local probe techniques, x-ray techniques, etc.), but they have the common issue, that no direct, locally resolved, observation of bulk magnetic domain structures

---

[4]The "knee" of the magnetisation curve B_k is defined by $B_k = \frac{1}{\sqrt{2}} \cdot B_s$ where B_s is the saturation magnetisation [81]
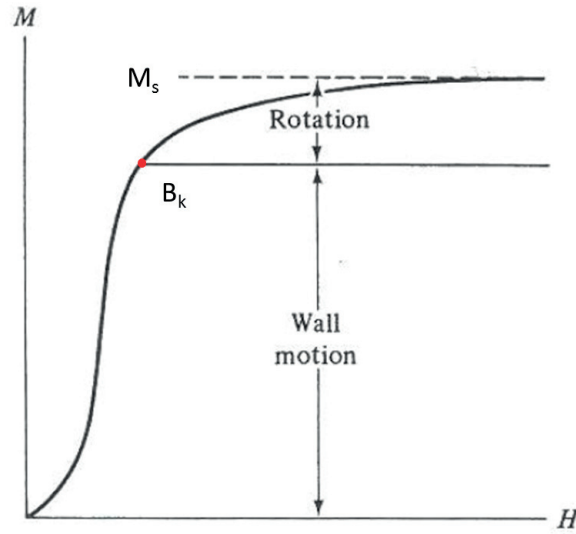
Figure 2.6: General separation of the magnetisation process into the process of domain wall motion and magnetisation rotation [41]. The saturation magnetisation M_s and the knee of the magnetisation curve B_k are marked.

is possible[5]. For the purpose of performing investigations of bulk magnetic domain structures and their behaviour, neutron dark-field images obtained by neutron grating interferometry, will be explained and performed in the following sections.

2.3 Attenuation based neutron imaging

To reveal the principle of neutron imaging, one has to think about what happens, when a beam of neutrons passes through matter. What happens is: the intensity of the incoming neutron beam will decrease, because neutrons are removed from the beam by nuclear interactions. As an uncharged particle, neutrons do not interact with the electrostatic potentials of electrons and protons in matter. The interaction of the neutrons is dominated by the strong neutron-nuclear interaction. Therefore a direct link between the atomic number of a material and the interaction probability with neutrons cannot be found[6]. For cold neutrons[7] the main two processes leading to the attenuation of a neutron beam are absorption and scattering at the nucleus of an atom. The cross sections for the absorption σ_a and the scattering σ_s summed together deliver the total cross section σ_t in this approximation:

$$\sigma_t = \sigma_a + \sigma_s. \tag{2.3}$$

---

[5] For the very dedicated cases of an iron alloy having 12.8 $at\%$ of silicon, the Libovicky method is able to investigate bulk structures, but is of destructive nature [82].

[6] In contrast to x-rays

[7] Cold neutrons are neutrons, having a kinetic energy between 0.12 meV and 12 meV, which is according to a wavelength between 26 Å and 2.6 Å [83].

Most databases for neutron cross sections give values for thermal neutrons with a velocity of $2200 \frac{m}{s}$ [84]. In the energy rnage of cold neutrons, the scattering cross section σ_s is mainly not energy dependent, while the absorption cross section σ_a is. Therefore the energy dependent total cross section for neutrons of velocity v can be given by

$$\sigma_t(v) = \sigma_s + \frac{2200\frac{m}{s}}{v} \cdot \sigma_{a,(2200m/s)}. \tag{2.4}$$

Consequently, slower (colder) neutrons have a stronger attenuation, since the absorption cross section is depending on v^{-1}.

The intensity of an incoming neutron beam is reduced by the loss of neutrons due to these interactions. Assuming, that no scattered neutron will hit the detector, the intensity I of a neutron beam with initial intensity I_0 transmitted through a sample of thickness t can be written by the famous Lambert-Beer law [85] as

$$I = I_0 \cdot e^{-\Sigma \cdot t}, \tag{2.5}$$

where the so-called attenuation coefficient Σ is given by

$$\Sigma = \sigma_t \cdot \frac{\rho \cdot N_A}{M_{Mol}}, \tag{2.6}$$

with ρ the density of the attenuating element, the Avogadro number N_A and the molar mass of the element M_{Mol}.

In Figure 2.7 a periodic table of the elements is shown with the corresponding attenuation coefficients for each element for neutrons with a velocity of 2200 m/s. Here a capricious behaviour of the coefficients is observed looking at the atomic number.

Figure 2.7: Periodic table of the elements with the corresponding attenuation coefficients (in cm^{-1}) for thermal neutrons with a velocity of 2200 m/s.

For an arbitrary number of elements, along a straight line L the formula for the beam intensity I becomes

$$I = I_0 \cdot exp\left[-\int_L \Sigma(x,y)dl\right],$$ (2.7)

in each pixel (x,y) of the detector behind the sample. The attenuation coefficient can be rewritten as

$$\Sigma(x,y) = \sum \Sigma_i(x,y) = \sum_i \sigma_{t_i} \frac{\rho_i(x,y)N_A}{M_{Mol_i}}.$$ (2.8)

This simple exponential behaviour does not apply to all situations. Thick samples, strongly scattering (hydrogen) as well as highly absorbing (boron, gadolinium) materials show a deviation due to multiple scattering effects, or the changing spectrum due to the strong energy dependence of the attenuation, need to be taken into account.

2.4 Wave optical description of neutron interaction with matter

2.4.1 Nuclear and magnetic interaction potentials

The propagation of low energy neutrons as particle waves can be described by the Schrödinger equations [86]. The propagation of light can be described by Maxwell's equations [87]. Due to mathematical analogies between these equations, analog phenomena can be found in neutron optics compared to light optics.

Particle wave fields $\psi(\mathbf{r},t)$ are described by the Schrödinger equation

$$H\psi(\mathbf{r},t) = \left(-\frac{\hbar^2}{2m}\nabla^2 + V(\mathbf{r},t)\right)\psi(\mathbf{r},t) = i\hbar\frac{\partial\psi(\mathbf{r},t)}{\partial t},$$ (2.9)

with H the hamiltonian, $\hbar$ the reduced Planck constant, m the mass of the particle, which is in our case a neutron ($m_N = 1.675 \cdot 10^{-27}\,kg$) and the interaction potential V. The analogy in the description of electromagnetic wave fields by the vacuum wave equation is obvious

$$\nabla^2\psi(\mathbf{r},t) - \frac{1}{c^2}\frac{\partial^2\psi(\mathbf{r},t)}{\partial t^2} = 0,$$ (2.10)

where c is the speed of light. Using the plane wave approach, these linear equations can be solved in free space by:

$$\psi_k(\mathbf{r},t) = a_k e^{i(k\cdot\mathbf{r}-\omega_k\cdot t)} = \psi(\mathbf{r})e^{-i\omega t}.$$ (2.11)

Here a_k is the amplitude, $|\mathbf{k}| = \frac{2\pi}{\lambda}$ is the modulus of the wave vector, λ is the wavelength of the neutron and ω is the angular frequency. In both cases, this leads in stationary situations, to the Helmholtz equation

$$\nabla^2\psi(\mathbf{r}) + k^2\psi(\mathbf{r}) = 0,$$ (2.12)

and consecutively to the following dispersion relations using the energy E

$$\text{for particle waves:} \qquad k_p^2 = \frac{2mE}{\hbar^2} \qquad\qquad (2.13)$$

and

$$\text{for electromagnetic waves:} \qquad k_{em}^2 = \frac{E^2}{\hbar^2 c^2} \qquad\qquad (2.14)$$

Note, that the velocity of wave propagation for electromagnetic waves is always constant (velocity of light c), while it is determined by the de Broglie relation [88] and is constant for particle waves.

Refraction, reflection, diffraction and interference are consequences of these stationary equations. Therefore the complete spectrum of phenomena known from the wave nature of light does also occur for neutron waves. Due to the variation in the time derivative in the wave equations, first order for particle waves (Equation 2.11) and second order for electromagnetic waves (Equation 2.10), time dependent phenomena are expected to be unequally.

To derive the refractive index for neutrons, quantum mechanical considerations have to be taken into account. Like p[hotons, neutrons that move inside a material, are influenced by spatially dependent potentials $V(\mathbf{r})$. The energy eigenstates ($E = \hbar\omega$) and the wave function in free space

$$\psi(\mathbf{r}, t) = \psi(\mathbf{r})e^{-i\omega t} \qquad\qquad (2.15)$$

solve the time-independent Schrödinger equation:

$$\nabla^2 \psi(\mathbf{r}) + \frac{2m}{\hbar^2} E\psi(\mathbf{r}) = 0. \qquad\qquad (2.16)$$

Interactions in the medium are described by the introduction of a potential term into equation 2.16, resulting in

$$\nabla^2 \psi(\mathbf{r}) + \frac{2m}{\hbar^2} [E - V(\mathbf{r})]\,\psi(\mathbf{r}) = 0. \qquad\qquad (2.17)$$

Both equations, 2.16 and 2.17, are Helmholtz scalar wave equations (compare equation 2.12). Accordingly, the wave vector $\mathbf{k}$ everywhere outside of a medium is

$$k^2 = \frac{2mE}{\hbar^2} \qquad\qquad (2.18)$$

and the wave vector $\mathbf{K}$ inside the medium including the potential $V(\mathbf{r})$ is

$$K^2(\mathbf{r}) = \frac{2m}{\hbar^2} [E - V(\mathbf{r})]. \qquad\qquad (2.19)$$

The spatially dependent refractive index $n(\mathbf{r})$ for neutrons is defined as the ratio of the wave vector inside a medium $\mathbf{K}(\mathbf{r})$ and the free space wave vector $\mathbf{k}$ [89]:

$$n(\mathbf{r}) = \frac{\mathbf{K}(\mathbf{r})}{\mathbf{k}} = \sqrt{1 - \frac{V(\mathbf{r})}{E}}. \qquad\qquad (2.20)$$

The scattering can be considered as isotropic, because the neutron-nucleus interacting range is much smaller than the wavelength of thermal neutrons. Therefore the Fermi pseudo potential can be used, to describe the interaction of neutrons with a sample which contains many nuclei [90] using the neutron scattering length[8] b [84] [91] and the position $\mathbf{R}_j$ of the j-th nuclei:

$$V_{nuc}(\mathbf{r}) = \frac{2\pi\hbar^2}{m} \sum b_j \delta(\mathbf{r} - \mathbf{R}_j). \tag{2.21}$$

Mostly the mean interaction potential (also called neutron optical potential) of a material is used and it can be given by

$$\langle V_{nuc}(\mathbf{r}) \rangle = \frac{2\pi\hbar^2}{m} b_c N \tag{2.22}$$

with the mean number of scattering nuclei per unit volume N and the mean coherent scattering length $b_c = \langle b \rangle$. The coherent scattering length can be positiv or negative since nuclear potential can also be attractive or repulsive[9] [91].

Any absorption and nuclear reaction effects are described by the imaginary part of the scattering potential in Equation 2.22. This results in a complex scattering length $b_c = b' - ib''$ [92]. As visible from Equation 2.20 the refraction index becomes also complex with the real part δ and the imaginary part β [55]

$$n(\mathbf{r}) = \sqrt{1 - \frac{V}{E}} = 1 - \delta + i\beta. \tag{2.23}$$

The imaginary part of the refractive index is responsible for absorption and incoherent scattering processes. It can be given as [93]:

$$\beta = \frac{\sigma_t N\lambda}{4\pi}, \tag{2.24}$$

where σ_t is the total reaction cross section per atom. For many materials, this imaginary part is small compared to the real part ($\delta/\beta \approx 10^4$) and therefore often neglected (within the energy range of cold neutrons).

Since in magnetic materials, the neutrons can interact not only with the nuclear potentials, but also with the magnetic field $\mathbf{B}$ in the sample via the neutrons' intrinsic magnetic dipole moment μ_N, the real part consists of a nuclear contribution δ_{nuc} and a magnetic contribution δ_{mag}, if a magnetic field $\mathbf{B}$ is present inside the sample.

The nuclear part is given by [55]

$$\delta_{nuc} = \frac{\lambda^2 N b_c}{2\pi}. \tag{2.25}$$

For magnetic interaction potentials $V_{mag}(\mathbf{r})$ having the form

$$V_{mag}(\mathbf{r}) = -\mu_N \cdot \mathbf{B}, \tag{2.26}$$

---

[8]The scattering length is an effective cross section, which is related to the type and strength of a potential
[9]Most time it is positive, but in general ranges from -5 fm to + 10 fm.

the magnetic contribution to the real part of the refractive index can be written using the kinetic energy of the free neutron E_0 as [94] [95]:

$$\delta_{mag} = \pm \frac{\mu_N \cdot \mathbf{B}}{2E_0} = \pm \frac{2\mu_N \cdot \mathbf{B} m\lambda^2}{h^2}. \tag{2.27}$$

When a neutron with its magnetic moment μ_N reaches a region with a magnetic field $\mathbf{B}$, a Zeeman splitting of the potential energy, corresponding to the two quantised spin states of the neutron occurs, with a magnitude of $\pm\mu_N \cdot \mathbf{B}$ [80] [96]. This happens on the cost of the kinetic energy of the neutron. Therefore, the velocity of the neutron is changed. The different momentum changes due to the Zeeman energies $\pm\mu_N \cdot \mathbf{B}$ of the eigenstates $\langle\uparrow|$ and $|\downarrow\rangle$ of the Pauli spin operator are responsible for the different signs. For further information see also Figure 2.9.

2.4.2 Neutron refraction at magnetic domain walls

The spontaneous magnetisation in ferromagnetic samples occurs from the magnetic moments of adjacent atoms being parallel [97]. As discussed in section 2.1 regions of atoms with magnetic moments pointing in the equal direction are called magnetic domain[10]. Each magnetic domain is described by the magnetic induction B, as can be seen in Figure 2.8. Inside each domain, the magnetisation points along a magnetic easy axis with the value of the saturation magnetisation B_s. For a cubic crystal like FeSi the directions x,y and z delineated in Figure 2.8 correspond to the crystallographic (001),(010) and (100) directions, respectively. The transition region between the two domains, called the domain wall, is the area, where the magnetisation rotates out of the easy direction. For Bloch domain walls, mostly present in GO-steels, the magnetisation rotates through the plane of the wall, while for Neél walls the magnetisation rotates in the plane of the wall. The thickness of the domain wall depends on the anisotropy of the material and is in the range of some nm for iron [70]. Additionally a neutron beam is schematically included in Figure 2.8, which aims at the domain wall. Neutrons are able to interact with the atomic nucleus and the magnetic moments of the atomic shells with their magnetic moment μ_N. The refraction of neutrons in magnetic materials can only be described correctly using dynamical approaches [98] [99] [100] [101] [102]. Therefore, the Schrödinger equation with a spin-dependent potential, depending on the average homogeneous magnetic induction, needs to taken for the description of the neutrons refraction. To do so, the domain walls are assumed to be infinitely thin and as a plane plate. This is permitted by the neutrons velocity being too large for an interaction with the magnetic moments of the atoms in the wall while passing through. It is called an adiabatic penetration process. Hence it is not necessary to investigate the neutrons behaviour inside the domain wall. This is in analogy to the Snell's law in optics, which describes the refraction of a light beam at an interface of changing refractive indices by simply the two refractive indices. To calculate the refraction angles, we consider the refraction of unpolarised neutrons at

---

[10]They are also called Weiss domain

domain walls as a boundary value problem of the Schrödinger equation including a spin dependent potential. Consequently, the Hamilton operator H is then given by:

$$H = -\frac{\hbar^2}{2m}\nabla^2 + V_{nuc}(\mathbf{r}) - \mu_N \cdot \mathbf{B}(\mathbf{r}), \tag{2.28}$$

using the mass of the neutron m, the nuclear interaction potential $V_{nuc}(\mathbf{r})$ and the product of μ_N and $\mathbf{B}(\mathbf{r})$ for the magnetic interaction potential. Passing through one magnetic domain, the neutron experiences only a constant interaction potential, allowing for the calculation of its behaviour with the time-independent Schrödinger equation inside one domain

$$H\psi(\mathbf{r}) = E\psi(\mathbf{r}). \tag{2.29}$$

Here $\psi(\mathbf{r}) = \begin{pmatrix} \psi\uparrow \\ \psi\downarrow \end{pmatrix}$ is the spinor of the neutrons. The total energy of a free neutron can be given as $E = \frac{\hbar^2 k^2}{2m}$ and the wave equation of a neutron in a magnetic material turns out to be:

$$(\nabla^2 + k^2)\psi(\mathbf{r}) - \frac{2m}{\hbar^2}\left[V_{nuc}(\mathbf{r}) + \mu_N \cdot \sigma \cdot \mathbf{B}(r)\right]\psi(\mathbf{r}) = 0. \tag{2.30}$$

Here, $\sigma = (\sigma_x, \sigma_y, \sigma_z)$ is composed of the 2x2 Pauli spin matrices. This is the vector that couples all components of the spin to the magnetic induction $\mathbf{B}$.

When entering a region of homogeneous magnetisation, a neutron experiences a potential
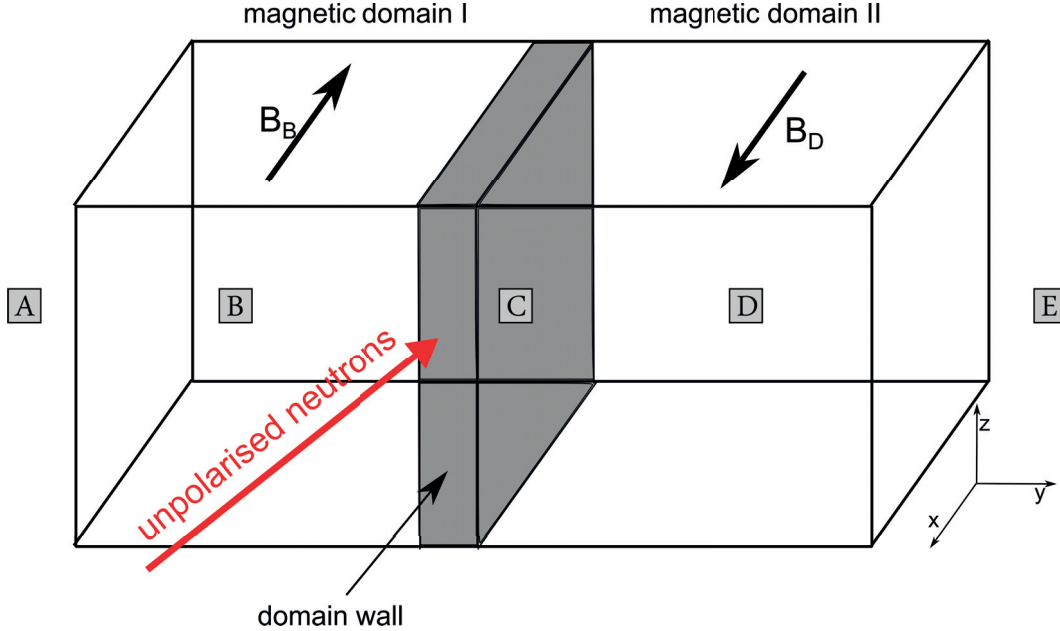
Figure 2.8: Schematic of a plane domain wall separating two neighboring magnetic domains with different magnetic inductions B. The neutrons transverse in series the regions A,B,C,D and E. Region A: Free space (air) outside the sample. Here no magnetic induction is present ($B = 0$). Region B: Magnetic domain I with constant magnetic induction B_B. Region C: The domain wall with rotating magnetic induction. Region D: Magnetic domain II with constant magnetic induction B_D. Region E: Free space (air) outside the sample ($B = 0$).

jump, which is depending on the spin state of the neutron (parallel or antiparallel to the magnetic induction **B**). The steadiness of the wave function and its derivatives at the magnetic sample surface is the boundary condition. Note, that inside the sample a constant nuclear potential is assumed, thereby only the magnetic potential jump needs to be taken into account, when calculating the neutrons behaviour while traversing a magnetic domain wall.

Due to the domain wall being considered infinitely thin, the neutron passes non-adiabatically through the wall, resulting in the neutrons spin being not able to follow the rotation of the magnetic induction in the wall, and therefore the spin is fixed during the passage. The Larmor frequency of the neutron is given by $\omega_L = \frac{2|\mu_N|\cdot|\mathbf{B}_S|}{\hbar}$. The probability of refraction for the neutron passing the domain wall, where the magnetic induction rotates with a frequency ω is determined by the ratio $\frac{\omega}{\omega_L}$ [101] [102]. As a consequence, behind a domain wall three different neutron beams exist. An unrefracted, unpolarised beam and two refracted spin-polarised beams, which are displaced by a certain angle compared to the incident beam. In analogy to the nuclear potential, the magnetic potential is also assumed to have an averaged magnetic induction $\mathbf{B}_{AV} = \mu_0\mathbf{H}_{AV} + \mathbf{M}_{AV}$ and furthermore the sample is considered as a continuum instead of a lattice.

The Schrödinger equation (Equation 2.30) is solved by a spinor of the form

$$\psi(\mathbf{r}) = c \cdot e^{i\mathbf{k}_{p,a}\cdot\mathbf{r}}, \tag{2.31}$$

while $\mathbf{k}_{p,a}$ are the wave vectors for the neutron with spin parallel or antiparallel to $\mathbf{B}_{AV}$:

$$\mathbf{k}_p^2 = k^2 - \Delta k^2 - k_{B_{AV}}^2 \quad \text{and} \quad \mathbf{k}_a^2 = k^2 - \Delta k^2 + k_{B_{AV}}^2. \tag{2.32}$$

In this equation $\Delta k^2 = 2\pi \cdot N \cdot b_c$ accounts for the nuclear and $k_{B_{AV}}^2 = \frac{2m}{\hbar^2} \cdot \mu_N \cdot |\mathbf{B}_{AV}|$ for the magnetic interaction. Substituting the wave vectors in Equation 2.20 results in an additional spin dependent potential contribution for magnetic materials:

$$n^2 = \frac{k_{p,a}^2}{k^2} = \frac{k^2 - \Delta k^2 \pm k_{B_{AV}}^2}{k^2} = 1 - \frac{\Delta k^2 \pm k_{B_{AV}}^2}{k^2}. \tag{2.33}$$

As visible in Figure 2.9, ferromagnetic samples behave as birefringent materials for a beam of unpolarised neutrons, due to the refractive indices inside the sample being related to the magnetic induction B. When neutrons penetrate a ferromagnetic sample, the first refraction occurs at the sample surface, where the first transition from air $\boxed{A}$ into the first magnetic domain $\boxed{B}$ occurs (compare Figure 2.8). A second refraction takes place at the domain wall. Due to the assumption of a homogeneous material in respect to the nuclear interaction potential the refractive index is given by just the magnetic potential changes

$$n^2 = \frac{k^2 \pm k_{B_{AV}}^2}{k^2 \mp k_{B_{AV}}^2}. \tag{2.34}$$

The whole process of the refraction of an unpolarised neutron beam at a sample surface and a magnetic domain wall is illustrated in Figure 2.9. Here, a domain wall separates two magnetic domains with opposite magnetic induction (compare also Figure 2.8). θ and $\mathbf{k} = (k_X, k_Y, k_Z)$

are the angle and wave vector of incident neutron beam. While the normal vector of the sample surface points in the z-direction, the normal vector of the domain wall points into the y-direction. The spin of the incoming neutron can either be parallel or antiparallel (marked by the index p and a) with respect to the z-direction. Due to its assumed homogeneity, the nuclear potential is neglected in the following:

$$k_{p,a}{}^2 = k^2 - \Delta k^2 \pm k_{B_{AV}}{}^2 \approx k^2 \pm k_{B_{AV}}{}^2. \tag{2.35}$$

Thus, the beam gets refracted at the surface of the sample, where the normal component of the wave vector k_Z jumps to $k_{Z,(p,a)} = \sqrt{k_Z{}^2 \pm k_{B_{AV}}{}^2}$. This results in an refraction angle at the
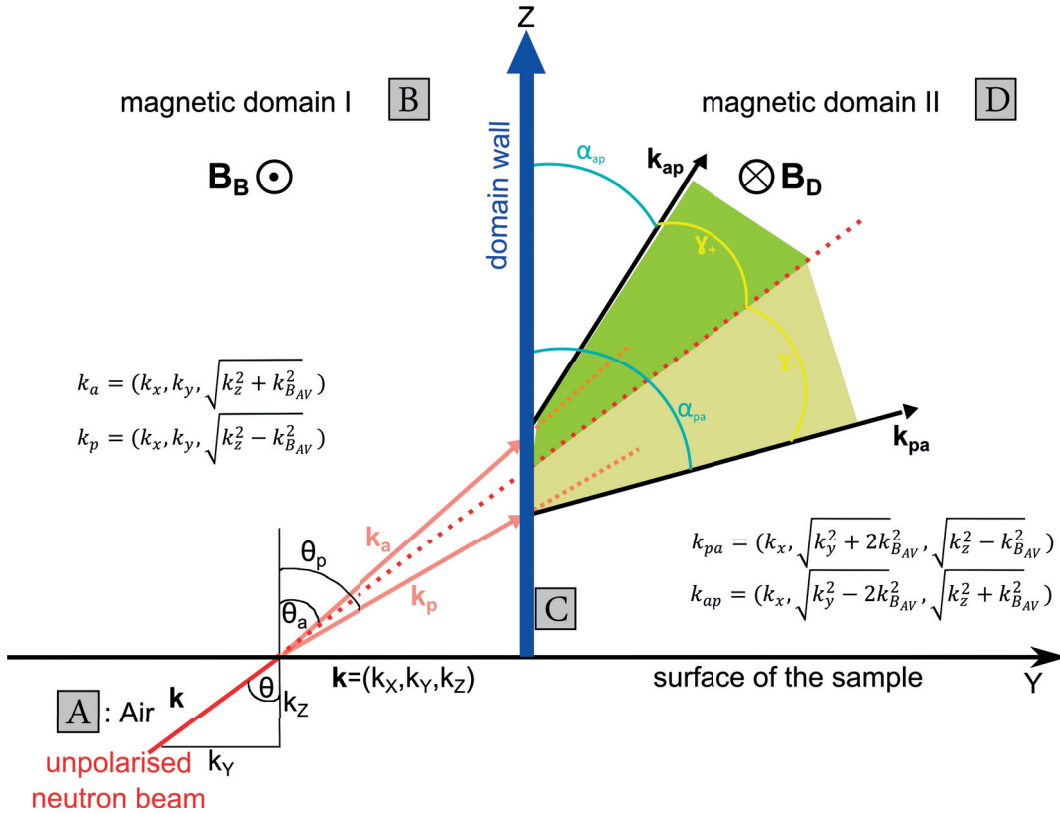
Figure 2.9: Mechanism of the refraction of an unpolarised neutron beam in a ferromagnetic sample. A domain wall separates two magnetic domains with opposite magnetic induction (compare also Figure 2.8). θ and **k** are the angle and wave vector of incident neutron beam. The beam gets refracted at the surface of the sample and later at the magnetic domain wall. Due to the first refraction, the normal component of the wave vector k_Z jumps to $k_{Z,(p,a)} = \sqrt{k_Z{}^2 \pm k_{B_{AV}}}$. The refraction angle for spin parallel and antiparallel are named θ_p and θ_a. Refracted at the domain wall, the normal component k_Y changes into $k_{Y,(pa,ap)} = \sqrt{k_Y{}^2 \pm 2k_{B_{AV}}}$ in dependence from the spin orientation. After being refracted at the domain wall, the refraction α_{ap} and α_{pa} can be found. The total refraction angle in the end is included as the two angles γ_+ and γ_-. No variation in the nuclear potential was included here.

sample surface for parallel or antiparallel spin with respect to the magnetic induction B_B of

$$\sin \theta_p = \frac{k_Y}{\sqrt{k^2 - k_{B_{AV}}^2}} \quad \text{or} \quad \sin \theta_a = \frac{k_Y}{\sqrt{k^2 + k_{B_{AV}}^2}}. \tag{2.36}$$

At the domain wall, where the magnetic induction changes suddenly (infinitely thin domain wall), a potential jump of $\pm 2\mu_N \cdot \mathbf{B}_S$[11] occures dependent on the spin configuration. As a consequence, the neutron beam gets refracted at the domain wall. The normal component k_Y changes from $-k_{B_{AV}}^2$ into $+k_{B_{AV}}^2$. This is a total change of $2k_{B_{AV}}^2$. Therefore, k_Y becomes $k_{y,(pa,ap)} = \sqrt{k_y^2 \pm 2k_{B_{AV}}^2}$ depending on the spin directions. The other components of the wave vector stay untouched. Accordingly, after being refracted at the domain wall, the refraction angles α_{pa} and α_{ap} are found as

$$\sin \alpha_{pa} = \frac{\sqrt{k_y^2 + 2k_{B_{AV}}}}{k^2 + k_{B_{AV}}} \tag{2.37}$$

for spin parallel and for spin antiparallel as

$$\sin \alpha_{pa} = \frac{\sqrt{k_y^2 - 2k_{B_{AV}}}}{k^2 - k_{B_{AV}}}. \tag{2.38}$$

The total refraction angles in the end γ_+ and γ_- (yellow in Figure 2.9) can be given for parallel and antiparallel by

$$\gamma_- = \alpha_{pa} - \theta = \arcsin\left(\frac{\sqrt{k_y^2 - 2k_{B_{AV}}}}{k^2 - k_{B_{AV}}}\right) - \theta \tag{2.39}$$

and

$$\gamma_+ = \theta - \alpha_{ap} = \theta - \arcsin\left(\frac{\sqrt{k_y^2 + 2k_{B_{AV}}}}{k^2 + k_{B_{AV}}}\right). \tag{2.40}$$

From these two equations (Equation 2.39 & 2.40) it can be seen, that the angles of refraction stay the same, independent from how the components of the wave vector $\mathbf{k}$ are distributed on k_X and k_Z. The angles are only depending on k_Y and $\mathbf{k}$ and the component of the spin in z-direction. Calculating the angles of refraction[12], they are found to be in the range of tenths of mrad. These angles are detectable with a neutron grating interferometer, as will be explained in detail in the following section 2.5.

---

[11] Here B_S is equal to the average magnetic induction $|B_{AV}|$.
[12] For 4.1 Å and a saturation magnetisation in iron of $\approx 2\ T$.

2.5 Neutron grating interferometer

2.5.1 Principle

The neutron grating interferometer setup is made of three gratings that are placed in a neutron beam [103]. These three gratings G_0, G_1 and G_2 are schematically illustrated in Figure 2.10 together with a velocity selector and a standard neutron detection system. In addition, the place, where various sample environments can be installed is marked by a dotted square[13]. The source grating G_0 is made of Gadolinium, which has a very high absorption cross-section for neutrons, and acts as an absorption grating. G_0 allows for the use of an incoherent neutron source of a width c (typically 20 millimeter). Regarding the spatial coherence, the source is transformed into an array of periodic line sources of width s, which is the slit width of the grating G_0. Each line source provides enough coherence to form an interferometric contrast. For the temporal coherence of the neutron beam, a velocity selector [104] is included, providing a wavelength band with a bandwidth of $\Delta\lambda/\lambda \approx 15\%$, while λ is the wavelength. This is sufficient for the requirements of the grating interferometer (a more detailed study of the coherence requirements can be found in [105]). All the parameters of the setup are designed for a wavelength of the neutrons of 4.1 Å due to some preconditions of the beamline. Therefore, the second grating, the phase grating G_1 provides a period p_1 of 7.96 μm and is placed at a distance l behind G_0. This grating is made of silicon with a height of each silicon
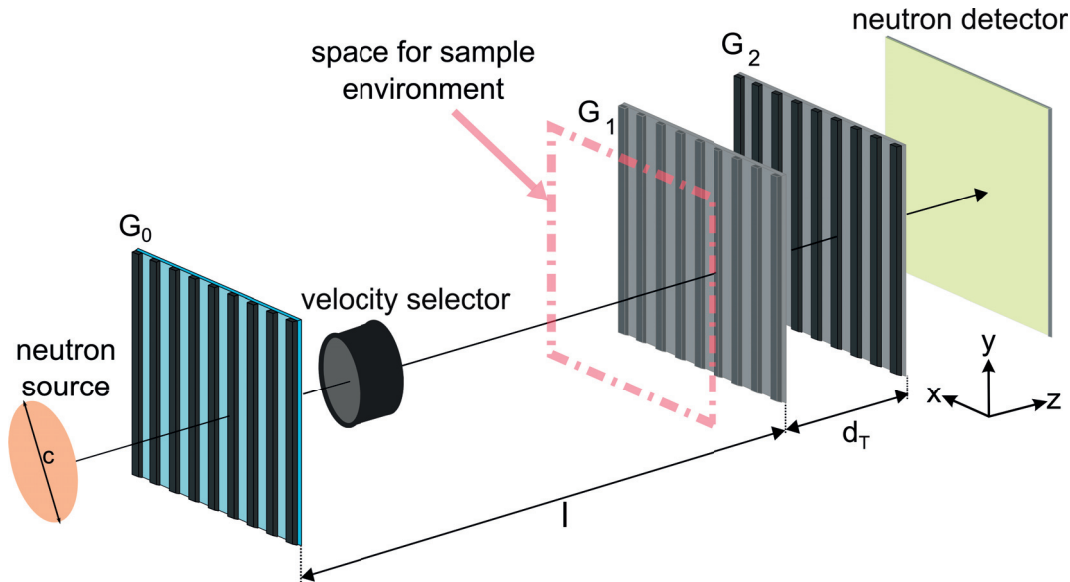
Figure 2.10: Schematic layout of the neutron grating interferometer including the three gratings G_0, G_1, G_2, a velocity selector and a conventional scintillator based neutron detection system. The distance l, the Talbot distance d_T and the source width c are included too. Furthermore the place, where various sample environments can be installed is marked by a dotted square.

---

[13]The different sample environments will be explained in detail in section 3.2

line of 37 μm. Using the following equation with the neutron scattering length density n_{SLD}[14] [84], the wavelength λ and the height h_1 of the silicon:

$$\Phi = n_{SLD} \cdot \lambda \cdot h_1 \qquad (2.41)$$

it becomes clear, that the phase shift Φ applied to the incoming neutrons at 4.1 Å is exactly π. Consequently the phase grating splits the incoming neutron beam into the ± 1 diffraction orders. In other words, the grating applies a periodic phase oscillation onto the incoming neutron beam. A Fresnel diffraction based self-imaging phenomenon called the Talbot-effect [106] transforms this phase modulation into an intensity oscillation behind G_1. This intensity oscillation forms a linear fringe pattern parallel to the lines of the phase grating that changes periodically as a function of the distance d from G_1.

By the use of a phase grating with a phase shift of π, the contrast of the generated interference pattern for an incoming plane wave is strongest for odd Talbot distances d_T, and zero in even Talbot distances:

$$d_T = n \cdot \frac{p_1{}^2}{8 \cdot \lambda}, \qquad (2.42)$$

with n an integer giving the number of the Talbot distance.

The interference pattern that is generated by a spherical wave with the radius l behind the phase grating G_1 is also strongest for an odd, Talbot distance of spherical waves $d_{T,sph}$. This can be given by:

$$d_{T,sph} = \frac{l \cdot d_T}{l - d_T}. \qquad (2.43)$$

Using the intercept theorem for diffraction, the magnification of the image is given by a factor M:

$$M = \frac{l + d_{T,sph}}{l} \overset{(2.4)}{=} \frac{l}{l - d_T} = \frac{d_{T,sph}}{d_T}. \qquad (2.44)$$

The periodicity p_2 of the third grating G_2 needs to match to the distance between the fringes of the interference pattern, given its purpose of transforming the fringe positions into a measurable intensity modulation on the detector. This is needed due to a lack of neutron detection systems with sufficiently high spatial resolution. The period of this analyser grating p_2, can be calculated using:

$$p_0 = p_2 \frac{l}{d_{T,sph}}. \qquad (2.45)$$

Consequently the period p_2 of G_2 is 4 μm in the here used setup, while the grating is again made of gadolinium. Using Equation (2.43) the distance l between G_0 and G_1 can be given by:

$$l = \frac{p_0}{p_2} \cdot \frac{l \cdot d_T}{l - d_T} \Rightarrow l = d_T \cdot \left(\frac{p_0}{p_2} + 1\right), \qquad (2.46)$$

---

[14] $n_{SLD} = \frac{\sum(b_c)}{v_m}$ with the bound coherent scattering length b_c and the molecular volume v_m [84].

and turns out to be 5.23 m in this instance.

Accordingly the magnification can be given in terms of p_2 and p_1

$$M = \frac{d_{T,sph}}{d_T} \overset{(2.5)}{=} \frac{2 \cdot p_2}{p_1},$$ (2.47)

with Equation (2.7) and Equation (2.8)

$$\frac{d_{T,sph}}{d_T} = \frac{p_0 + p_2}{p_0} \overset{(2.8)}{\Rightarrow} p_1 = \frac{2 \cdot p_0 \cdot p_2}{p_0 + p_2}.$$ (2.48)

Hence the first Talbot distance d_{T_1} can than be calculated by:

$$d_{T_1} = \frac{p_1^2}{8\lambda} = \left(\frac{p_0 \cdot p_2}{p_0 + p_2} \right)^2 \cdot \frac{1}{2\lambda},$$ (2.49)

and is 19.4 mm for our case.

The distance l can now be given with Equation (2.8) as

$$l = \frac{1}{2\lambda} \cdot \left(\frac{p_0 \cdot p_2}{p_0 + p_2} \right)^2 \cdot \left(1 + \frac{p_0}{p_2} \right) = \frac{1}{2\lambda} \cdot \frac{p_0^2 \cdot p_2}{p_0 + p_2}.$$ (2.50)

Solving this equation, the period p_0 of G_0 is obtained as

$$p_0 = \frac{\lambda \cdot l}{p_2} \cdot \sqrt{ \left(\frac{\lambda \cdot l}{p_2} \right)^2 + 2\lambda l},$$ (2.51)

resulting in 1076 μm for our setup.

A brief overview of the most important parameters of the neutron grating interferometer used at ICON [107] beam line, SINQ, PSI, is tabulated in Table 2.1. Significant variation of these parameters induces several effects, that will be investigated during the PhD-thesis of R. Harti in the future years.

period source grating p_0	1076 μm
period phase grating p_1	7.96 μm
period analyser grating p_2	4 μm
distance l	5.23 m
Talbot distance d_T	19.4 mm
Wavelength λ	4.1 Å

Table 2.1: Theoretically derived nGI setup parameters for the ICON beam line at PSI.

The detection system used in the interferometer setup is scintillator based. A ^{6}LiF/ZnS scintillator converts the neutrons into visible light. In this type of scintillator, the ^{6}Li acts as converter and creates charged particles by a nuclear reaction

$$^6Li + n \rightarrow T + \alpha + 4.79 MeV$$
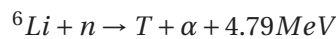
with the triton T and the alpha particle α inducing ionisation and excitation in the solid [108]. This ionisation will stimulate a photon emission from the ZnS crystals, which are mixed together with the LiF in an organic binder. This scintillation light is then reflected by a mirror, that is mounted under 45°, to a high light sensitivity camera, which is placed outside the direct neutron beam to prevent from direct irradiation damage. The cameras used are either charge-coupled device types (CCD) or scientific complementary metal-oxide-semiconductor(sCMOS) based cameras. These cameras allow for different effective pixel sizes due to different optical lens systems focusing the scintillator screen onto the chip.

For the purpose of grating interferometry two different camera/scintillator systems are available. One provides a field of view of 27.5 mm x 27.5 mm (called microbox [109]) and a second one, which provides a larger field of view of 150 mm x 150 mm (called midibox [107]). For the experiments in this thesis, only the larger camera/scintillator system (midibox) has been used.

2.5.2 Data acquisition and image processing

As shown in Figure 2.11 and explained at the beginning of this section, an interference pattern is created behind G_1 with a period of 4 μm, due to the interplay of the first gratings G_0 and G_1. This interference pattern cannot be resolved by the imaging detector due to its small periodicity. In order to circumvent this problem, the analyser grating G_2 is placed in the plane of the interference pattern. A spatial phase stepping approach [110] is used, to transfer the interference pattern into an intensity modulation on the detector that is placed behind G_2 (compare also Figure 2.10). Scanning the analyser grating in equidistant steps in the direction of x_{st} over one grating period p_2 results in a stack of images with different grating positions, and hence a different intensity modulation in each detector pixel is recorded. To be able to
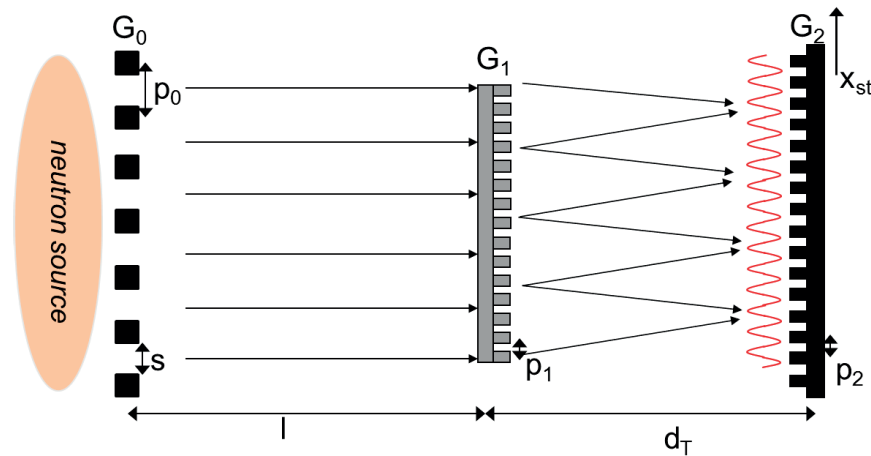

Figure 2.11: Schematic of the nGI principle. G_0 produces a coherent neutron beam while G_1 applies a phase shift of π resulting in an interference pattern of period p_2 (Equation 2.6). x_{st} marks the direction the grating is moved in the phase stepping approach used for the detection of the interference pattern.
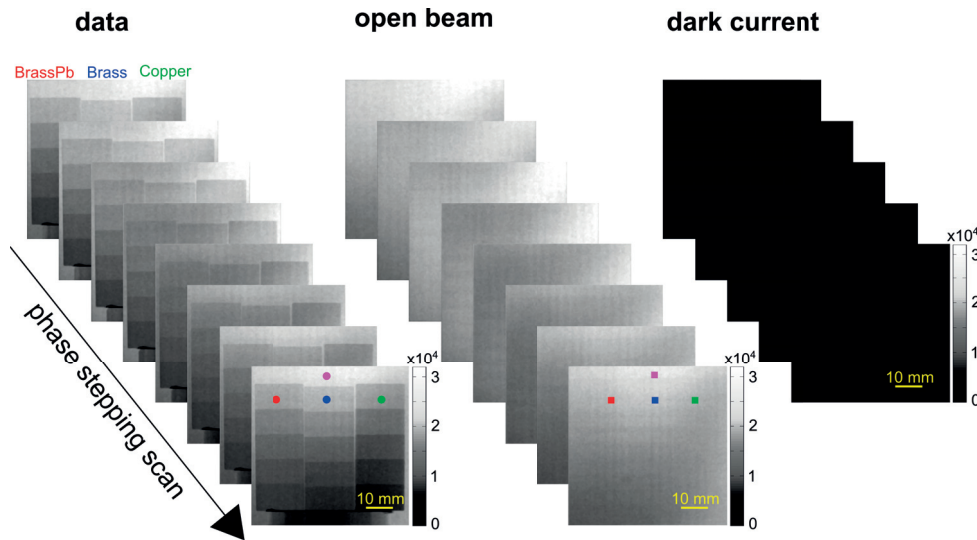
Figure 2.12: Phase stepping stacks with sample in the beam (data), without sample (open beam) and with closed shutters (dark current). Circles and squares mark the pixel, where the oscillations, shown in Figure 2.13, are examined. The exposure time for each image was 30 seconds. Here the samples are step wedges made of brass containing lead, brass and copper from left to right.

produce a dark-field image (DFI), three different sets of images need to be recorded. Those are a stepping scan with the sample in the neutron beam (data), a stepping scan without sample inside the neutron beam (open beam) and a stack where images are taken with closed shutters[15] (dark current). These stacks can be seen in Figure 2.12 where eight data images, eight open beams and five dark currents are shown. The samples shown here are three step wedges (each step 0.5 mm) made of brass containing 3 % lead (red point), brass (blue point) and copper (green point) [111].

The dark current stack is used, to correct for extraneous noise in the CCD camera, which is an electronic offset. The open beam stack (same steps as performed for the collection of the data stack) is required for the correction of inhomogeneous illumination by neutrons, inhomogeneous camera sensitivity and effects such as wave front distortions originating from the gratings themselves. Note that the same principle applies regardless of which grating is stepped. We stepped the source grating G_0, which requires the lowest precision in each mechanical step due its comparably large periodicity.

The first data processing step is the background correction of all acquired data and open beam images. This is achieved by subtracting an average dark current image, formed by averaging all 5 dark currents into one, from each single data and open beam image.

Due to the phase stepping over one period, the intensity $I(m, n, x_{st})$ in each detector pixel (m, n) oscillates as a function of the stepping x_{st}. This is shown schematically in Figure 2.13 a). For the pixels marked by the circles (data) and squares (open beam) in Figure 2.12 this oscillation is respectively plotted versus the stepping x_{st} in Figure 2.13 b) and c).
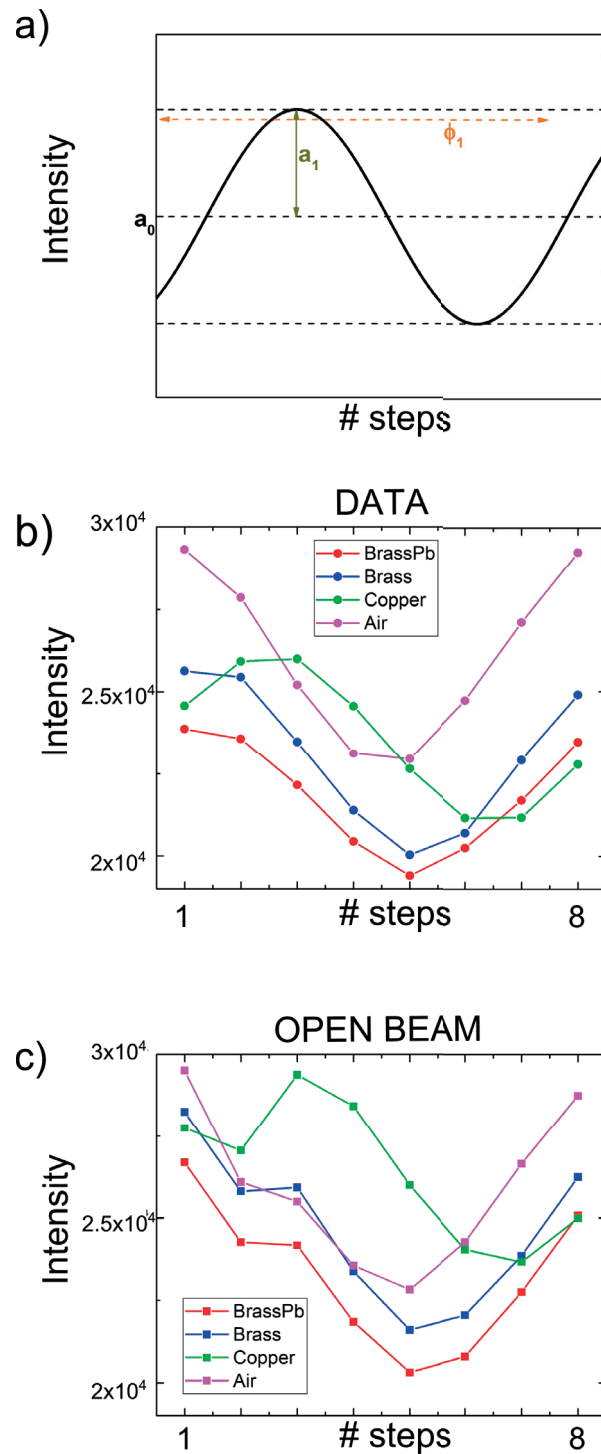
---

[15]no stepping is required

Figure 2.13: a) Schematic oscillation in one detector pixel using the amplitude a_1, the offset a_0 and the phase coefficient ϕ_1. Oscillation of the four pixels (BrassPb, Brass, Cu and air) marked by circles b) and squares c) in Figure 2.12.

These intensity oscillations $I(m, n, x_{st})$ can be described by a Fourier series for each single detector pixel:

$$I(m, n, x_{st}) = \sum_i a_i(m, n) \cdot cos(ikx_{st} + \phi_i(m, n))$$

$$\approx a_0(m, n) + a_1(m, n)cos(kx_{st} + \phi_1(m, n)) \tag{2.52}$$

with a_i being the amplitude, ϕ_i the phase and $k = \frac{2\pi}{p_2}$, using the period p_2 of G_2.

A sinusoidal oscillation can be characterised by the amplitude a_1, the offset a_0 and the phase ϕ_1. We can extract from the oscillation the coefficients (a_0, a_1, ϕ_1) for each detector pixel (m, n).

When we denote the coefficient for a pixel of an image with sample by an s and without sample by ob, we end up with the transmission image (TI) of our sample by normalising the sample image to the open beam image pixel wise:

$$TI(m, n) = \frac{a_0^s(m, n)}{a_0^{ob}(m, n)}. \tag{2.53}$$

The TI, calculated that way, is analogue to the transmission image obtained in classical neutron imaging without a grating interferometer installed. The fact that it is calculated by just using the offset of the two oscillations, which is the mean intensity, clearly demonstrates the attenuation based nature of the TI. The such computed TI of step wedges is shown in Figure 2.14 a). A lead containing brass wedge (left) and a brass wedge without lead (middle) both provide a similar attenuation that increases with increasing thickness of the wedge (downwards). The thickness dependent, exponentially decaying behaviour is described by the Lambert-Beer law in Equation 2.5 [112]. Both brass alloys cannot be distinguished within the uncertainty in this image. The same behaviour for increasing thickness is also provided by the copper wedge (right), although the attenuation is slightly higher than for both brass alloys. It is distinguishable from the brass due to the higher attenuation coefficient of copper (theoretical: Cu: 1.07 cm^{-1} Br: 0.78 cm^{-1}).

The dark-field image (DFI) is formed by the analysis of the amplitude coefficients of the sample $a_1^s(m, n)$ and the open beam $a_1^{ob}(m, n)$ in each pixel. As a first step, normalising the amplitude coefficient a_1^{ob} to the offset a_0^{ob} of the open beam results in the the so-called visibility V^{ob}. This visibility determines the maximum contrast that can be produced by the interferometer

$$V(m, n) = \frac{I_{max}^{ob} - I_{min}^{ob}}{I_{max}^{ob} + I_{min}^{ob}} = \frac{a_1^{ob}(m, n)}{a_0^{ob}(m, n)}. \tag{2.54}$$

For the DFI observation the normalised amplitude coefficient $V^s = \frac{a_1^s(m,n)}{a_0^s(m,n)}$ is normalised to the visibility V^{ob} of the open beam

$$DFI(m, n) = \frac{V^s(m, n)}{V^{ob}(m, n)} = \frac{a_1^s(m, n) \cdot a_0^{ob}(m, n)}{a_0^s(m, n) \cdot a_1^{ob}(m, n)}. \tag{2.55}$$
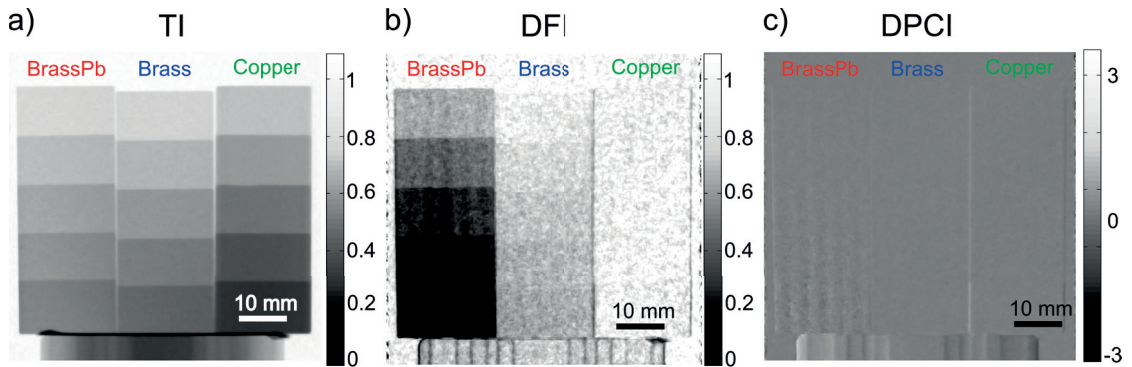
Figure 2.14: Data set, as obtained by one stepping procedure. a) Transmission image (TI) of the three step wedges (brass containing lead, brass and copper from left to right). No visible difference between the brass wedges with and without lead. The copper wedge provides a higher attenuation. The thickness dependent behaviour is described by the Lambert-Beer law [85]. b) Dark-field image (DFI) of the same wedges. The lead containing brass wedge shows a strong contribution, while the brass without lead has a much smaller contrast and the copper does only contribute to the image at its edges. c) Differential Phase Contrast Image (DPCI) of the three wedges. All three wedges are hardly visible.

The DFI of the three step wedges is shown in Figure 2.14 b). The brass containing the lead provides a strong contrast. This contrast again increases with increasing sample thickness. The brass without lead shows only a small contribution in the DFI while the copper stays entirely invisible. Only the edges of the copper wedge show a marginal contribution to the signal. Figure 2.15 a) shows the homogeneous, plain copper, that only introduces a constant phase shift due to its nuclear interaction potential for neutrons. This is not measured in the DFI, only at the edges, where neutron are reflected a small signal is generated [111]. If in a sample strongly varying interaction potentials are present, like in the brass containing the lead, a significant contribution in the DFI is generated. This potential fluctuations in the brass with lead arise from the fact that the lead forms precipitations inside the copper-zinc matrix. Lead has a different interaction potential than brass and the micrometer in size lead island can easily be seen in Figure 2.15 c), where they are marked by purple arrows [113].

As shown in Figure 2.15 b), in the brass alloy without lead two separate phases of brass are present (α-phase: $40\% : 60\%$ and β-phase: $60\% : 40\%$ of Cu/Zn[16]). Both phases provide a slightly different interaction potential for the neutrons. Due to the interaction potential being only slightly different, the contrast formed by the brass without lead precipitations in the DFI is less pronounced than for the brass with lead precipitations.

In general the reduction of the DFI signal is proportional to the degradation of the ability of the incoming neutron beam to interfere, due to scattering or multiple refractions at potential fluctuations inside the sample [114][115][116][117]. The thickness dependent exponentially decaying behaviour of the DFI signal is described analogue to the transmission image by a similar law in [111].

---

[16] $b_{c_{Cu}} = 7.49 \cdot 10^{-24} cm^{-1}$ & $b_{c_{Zn}} = 4.05 \cdot 10^{-24} cm^{-1}$ [84]
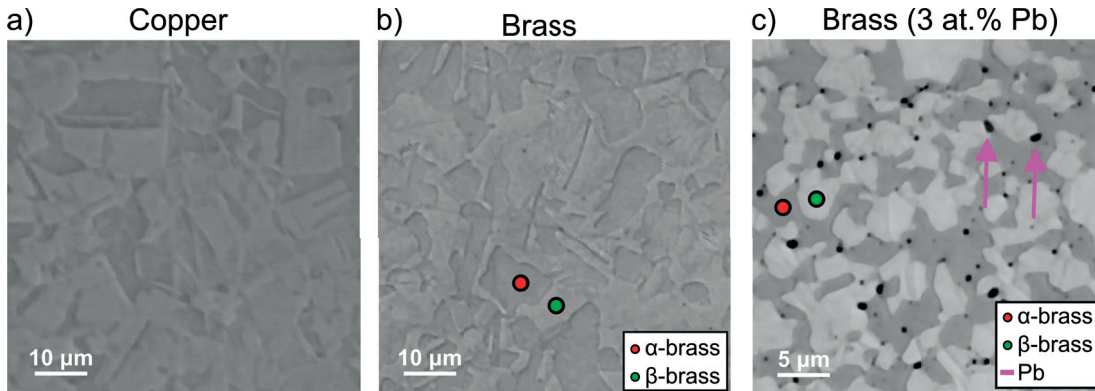
Figure 2.15: Grinding patterns obtained by optical light microscopy. a) Copper as a one-phase material. The structure is due to the different orientations of different fcc grains. b) Brass as a two-phase material. c) Brass containing lead as a three-phase material with micrometer sized lead islands [111].

When performing a phase stepping scan of a sample with nGI, a third image, the differential phase contrast image (DPCI), is obtained [60]. As an example, the DPCI of the three step wedges is shown in 2.14 c). Here, all three wedges are hardly visible, however in the brass containing lead wedge some artifacts occur[17]. The DPCI is calculated by the use of the phase coefficient of the intensity oscillation with sample ϕ_1^s and without sample ϕ_1^{ob} as:

$$\text{DPCI}(m, n) = \phi_1^s - \phi_1^{ob}. \tag{2.56}$$

For completeness, the calculation of the DPCI is given here, however no DPCI will be shown or used in the remainder of this work.

2.5.3 Dark-field imaging of magnetic domain structures

As derived in section 2.4, also potential fluctuations of magnetic origin can interact with neutrons and neutrons can be refracted by magnetic domain walls. Multiple refractions at domain walls will act in the same manner onto the interference pattern as did the small-angle scattering due to the nuclear potential fluctuations in the case of the brass containing lead (Figure 2.14). Accordingly, a neutron beam undergoing multiple refractions at domain walls has a locally degraded coherence when exiting the sample [99]. This decreases the ability of the neutrons to interfere behind the phase grating G_1 and results in a local decrease of the interference pattern. This is illustrated in Figure 2.16, where orange lines in the sample represent magnetic domain walls. Neutrons penetrating the sample are multiply refracted and decrease the coherence of the exiting neutron beam behind the sample. This results in a degraded visibility of the interference pattern and consequently in a decreased value of the DFI. Thus the value in the DFI is correlated to the relative density of magnetic domain walls in the sample. The ability of the nGI to visualise magnetic domain wall densities has been shown

---

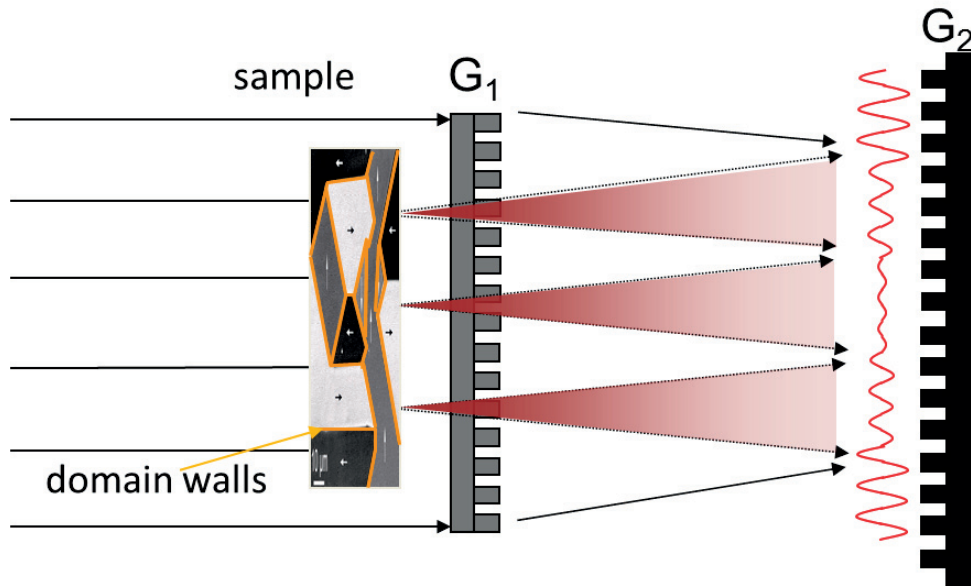[17]For further information about the DPCI see [60] [118] and [119]

Figure 2.16: Multiple neutron refractions at domain walls (orange) inside a sample lead to a local degradation of the coherence and consequently to a decreased visibility of the interference pattern.

[61][63] as well as the possibility of the visualisation of individual magnetic domain walls [62] [120], even in three dimensions [64].

A demonstration of the visualisation of a magnetic domain wall density is shown in Figure 2.17. In a) a schematic of the domain wall structure (red) in a magnetised and a non-magnetised steel foil is shown. The upper foil is magnetised by neodymium magnets, while the lower foil is not. The foils are both mounted on an aluminum holder. In b) the TI of the two 20 μm thick steel foils is shown. The upper foil is between the magnets the lower one does not have magnets. Both foils are invisible in the TI due to the small attenuation of steel. Only the aluminum holder and the neodymium magnets are visible. The DFI of the two steel foils is shown in c). Here, the lower foil provides a contrast while the upper foil, between the magnets, stays invisible. This can be explained by the lower steel foil providing a high density of magnetic domains and thereby domain walls inside the foil (compare a)). These domain walls degrade the coherence of the neutron beam and thereby decrease the DFI signal.

The upper steel foil is magnetised by the attached magnets. That means the foil is in a "'one-domain-state"', with no domain walls inside the sample (compare schematic in a)). This results in no magnetic scattering for the penetrating neutrons and hence no reduction in the DFI signal. The magnets themselves completely attenuate the signal. This results in a noisy signal in the DFI without further information being able to be ascertained.
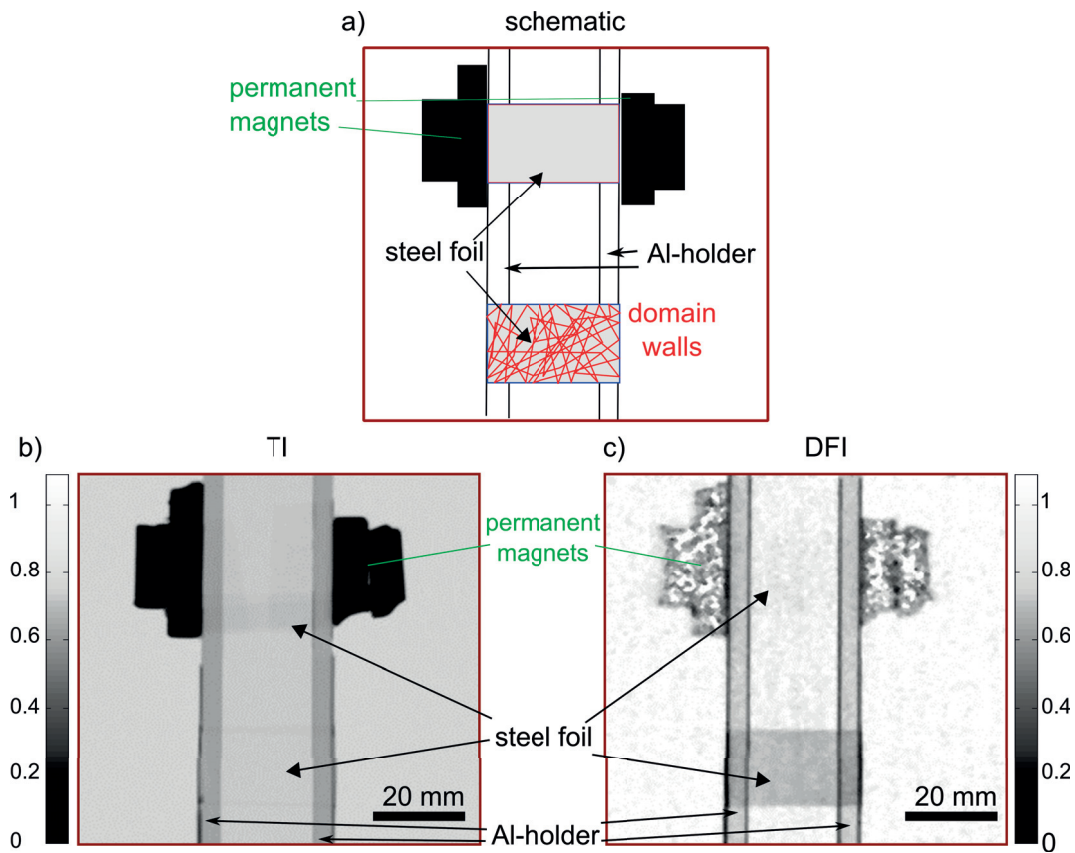
Figure 2.17: Magnetised and non-magnetised steel foil. In a) a schematic of the domain wall structure (red) in the magnetised and non-magnetised steel foil is shown. The upper foil is magnetised by neodymium magnets. In b) the TI of the two steel foils (20 μm thickness) is shown. One foil is mounted between neodymium magnets one is mounted without magnets. In the TI both foils are invisible. In the DFI of the two steel foils in c) the magnetised foil does not show a contribution while the non-magnetised does. The magnetic domain walls inside the lower foil refract the neutrons leading to a decreased DFI signal. The magnetised foil provides no inner domain walls resulting in no scattering and no degradation of the interference pattern. The aluminum holder as well as the neodymium magnets are visible in both images.

3 | Setup and sample environment

In this chapter, the nGI setup with the individual gratings and components as they are used for the experiments are shown. The sample environments for various external influences like magnetic excitations and stress application are explained and illustrated. In the last section, the dark-field signal is characterised concerning firstly the particle size dependent (ultra-) small angle scattering and secondly the concentration dependent altering macroscopic scattering cross section.

3.1 Setup

3.1.1 Standard nGI setup

In Figure 3.1 a schematic of the ICON beam line is shown including the positions of the three gratings [1], the velocity selector and the classical detection system as well as the distances d_T and l. The standard nGI setup, which was available when this work started was installed and put into operation during this thesis. The standard setup allows for an easy use and fast installation and alignment. The whole setup consists of a box containing the source grating G_0 (G_0-box), a velocity selector and an interferometerbox. The interferometerbox is placed as a backpack on the camera system.

Starting from the neutron source in Figure 3.1 one can see, that both devices, the G_0-box and the velocity selector are placed in a vestibule. Both are shown in Figure 3.2. In a) the velocity selector is shown, providing the "monochromatic" beam of neutrons by rotating blades that allow only neutrons of a certain velocity range to pass, others are absorbed by the blades [104]. The place where the G_0-box is installed is marked by a red square. A photograph of the G_0-box with the source grating itself in the middle can be seen in b). The grating is mounted, such that it can be translated and rotated. The translation in direction x_{st} is needed for the data acquisition (explained in section 2.5.1), while the rotation allows for the adjustment of p_0 by rotating the grating out of the squareness. Another optical photograph shows the source grating in a higher magnification in c). The single lines with a period of 1076 μm and a duty cycle[2] of 0.4 are visible.

---

[1] Due to the practical conditions the gratings G_1 and G_2 are put together in the so-called "interferometerbox"

[2] Duty cycle D is the percentage of one period which is not covered by gadolinium. $D = \frac{T}{P} \times 100\%$ with P the period and T the uncovered length.
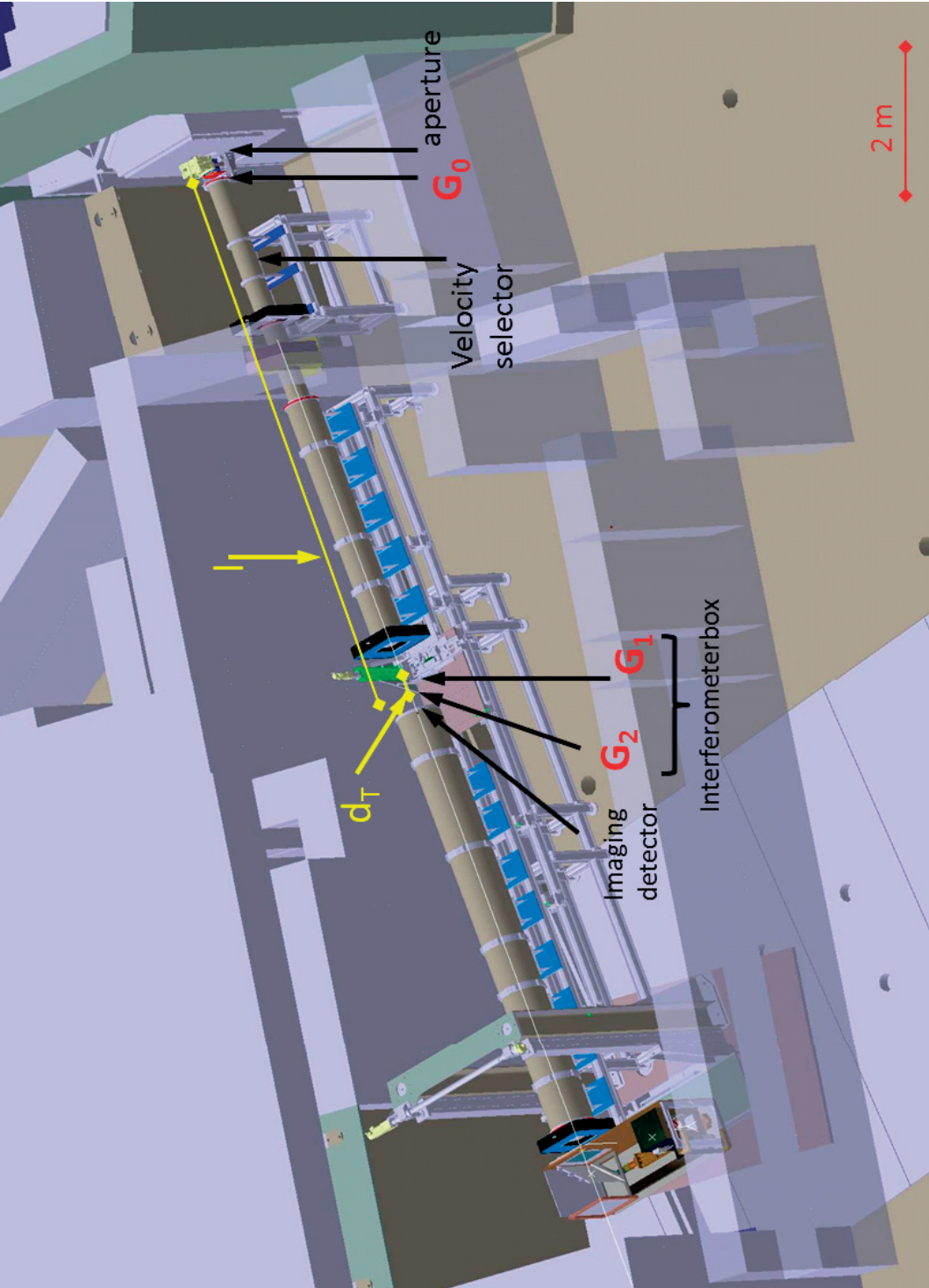
Figure 3.1: The layout of the ICON beam line at PSI including several parameters of the nGI setup [121]. The place for the interferometerbox, G_0-box and the velocity selector are marked.
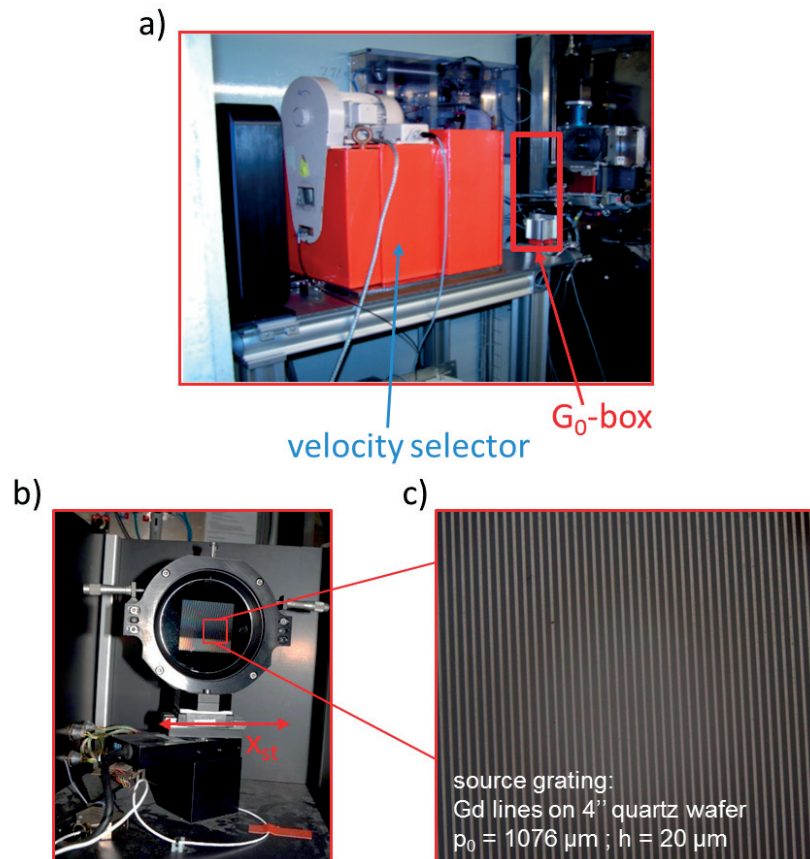
Figure 3.2: Optical photographs of the velocity selector and the G_0-box. In a) the velocity selector is shown. It provides the "monochromatic" beam of neutrons by rotating blades that allow only neutrons of a certain velocity range to pass [104]. The place where the G_0-box is installed is marked by a red square. A photograph of the G_0-box with the source grating itself in the middle can be seen in b). The translation in the direction x_{st} is needed for the data acquisition. Another optical photograph shows the source grating in a higher magnification in c). The single lines with a period of 1076 μm and a duty cycle of 0.4 are visible.

The interferometerbox of the standard setup is placed in front of the detector (see Figure 3.1) and can be seen in in more detail in Figure 3.3. Figure 3.3 a) shows the box with an opened front door while the gratings G_1 and G_2 are labeled. The whole interferometerbox as it is installed directly in front of the camera system as a backpack with closed front door can be seen in Figure 3.3 b). The gratings can be aligned by a rotation of both gratings around the axis of the neutron beam (±4°) and a translation of G_1 in ± beam direction (±20 mm from d_T). The CCD camera used for recording the raw images is visible on top. All the controllers of the stages are interfaced in the conventional, Labview based control software of the beam line (PIN). The scintillator screen and camera box (midibox) is placed directly behind G_2. In addition a rotation stage on top can be installed as visible in Figure 3.3 a). This stage allows for the tomography of a sample, placed between the two gratings of the interferometerbox. The

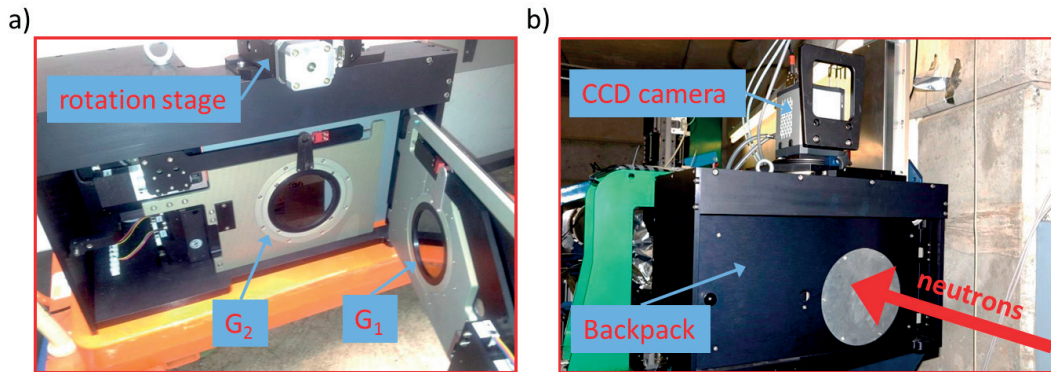**Figure 3.3:** The standard setup, also called backpack setup. In a) the opened interferometerbox with G_1 and G_2 labeled can be seen with the rotation stage on top. The whole interferometerbox can be placed onto the detection system as a backpack allowing for fast assembly and alignment as shown in b). Also the CCD camera on top can be seen here.

field of view is determined by the gratings active area which is 64 mm x 64 mm.

A more detailed view of the gratings G_1 and G_2 is shown in Figure 3.4. Here in a) the phase grating G_1 is shown. The left image is an optical image, where the active area of 64 mm x 64 mm can be seen. On the right a scanning electron microscopy (SEM) image of a cross section of G_1 is shown. The height as well as the period are delineated. In b) the analyser grating G_2 is shown. On the left an optical image, again with the active area is shown, while on the right a cross section scanning electron microscopy image of the 9 μm gadolinium attached to the underlying silicon structure can be seen.

For measurements without magnetic fields, the standard setup worked well, but during the first measurements where magnetic fields were applied, problems in the image quality, namely vertical stripes, appeared. These stripes were produced from drifts of the interferometer grating[3]. These movements occurred, due to parts of the motors, holders, ball bearings and screws being made from magnetic material, which reacts onto the magnetic fields. Therefore a modified grating interferometer setup with the purpose of being insensitive to a magnetic sample environment was designed, produced and put into operation during this thesis.

---

[3] These slight movements induce changes in the grating generated Moirée pattern

a) G_1

phase grating G_1: p_1 = 8 µm ; h = 37 µm   10 µm

b) G_2

Gadolinium

Silicon

analyser grating G_2: p_2 = 4 µm ; h_{Gd} = 9 µm   5 µm
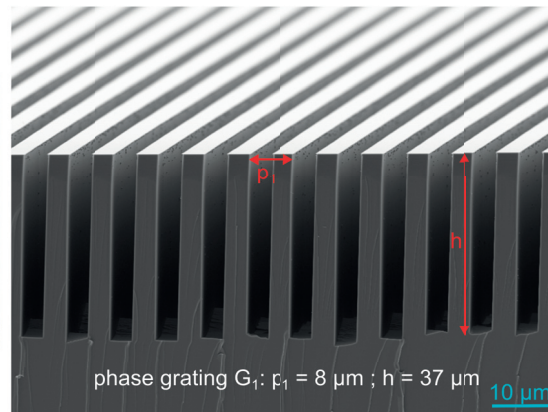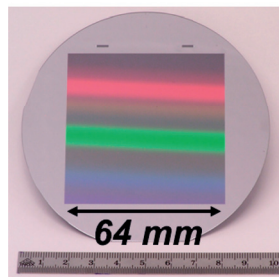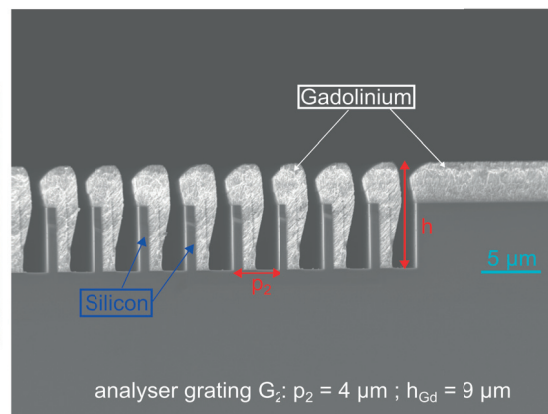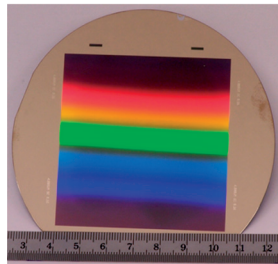
Figure 3.4: Optical photographs and SEM images of the gratings G_1 and G_2. In a) the phase grating G_1 is shown. On the left an optical image, where the active area of 64 mm x 64 mm can be seen. On the right a cross section scanning electron microscopy image is shown. The height as well as the period can be seen. In b) the analyser grating G_2 is shown. On the left an optical image, again with the active area can be seen, while on the right a cross section scanning electron microscopy image of the 9 μm gadolinium attached to the underlying silicon structure is shown.

3.1.2 Modified nGI setup for magnetic measurements

For the modified setup, the G_0-box and the velocity selector stay the same, and at the same place of the beam line. Just the interferometerbox is unique for each setup. This setup is commonly named non-magnetic-setup and it is shown in Figure 3.5 a) and b) from two different perspectives. The same gratings (G_1 and G_2) as used in the standard setup are mounted on support rings and used again. These support rings are mounted on profiles that are fixed on goniometer heads. This setup provides also a field of view of 64 μm x 64 μm. Due to its purpose of being insensitive to magnetic fields, all holders, screws, ball bearings and surroundings are made of nonmagnetic materials. Furthermore, the setup is very flexible, with respect to the installation of sample environments and possibilities of varying sample positions. This is realised through the grating being fixed on two independent holders. In addition, the area around the gratings is not obstructed by a closed box as a surrounding like for the standard setup. The sample that is placed in front of G_1 in Figure 3.5 b) is a steel lamination. This setup enabled for the magnetic investigations performed for the purpose of this thesis. The requirement of magnetic insensibility and spatial resolution (up to $\approx 50\mu m$) are fulfilled by this newly developed setup.
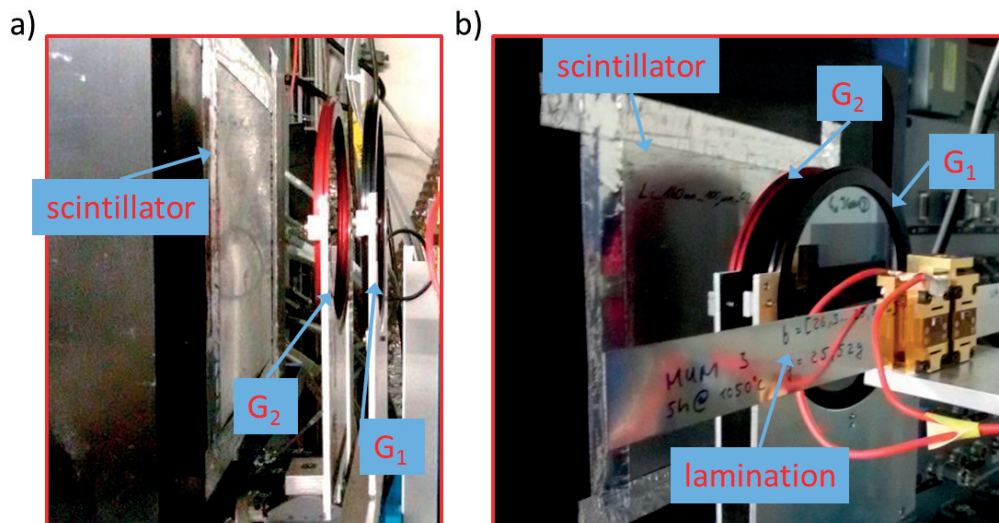
Figure 3.5: Optical photographs of the modified setup. The same gratings (G_1 and G_2) as used in the standard setup, mounted on support rings. Insensitivity for magnetic fields is realised by all holders, screws and surroundings being made of nonmagnetic materials. The sample that is placed in front of G_1 in b) is a steel lamination.

3.2 Sample environment

3.2.1 For magnetisation measurements

For the investigation of GO-steel laminations under the influence of magnetic fields a magnetic sample environment was produced. A **magnetisation frame** similar to an Epstein frame geometry (compare section 1.1.2) was purchased and implemented into the control software. This magnetisation frame[4] is shown in Figure 3.6.

In a) a simplified drawing of the frame can be seen. By a current I applied to the windings, a magnetic field B can be induced in the lamination. Hereby the lamination can be magnetised
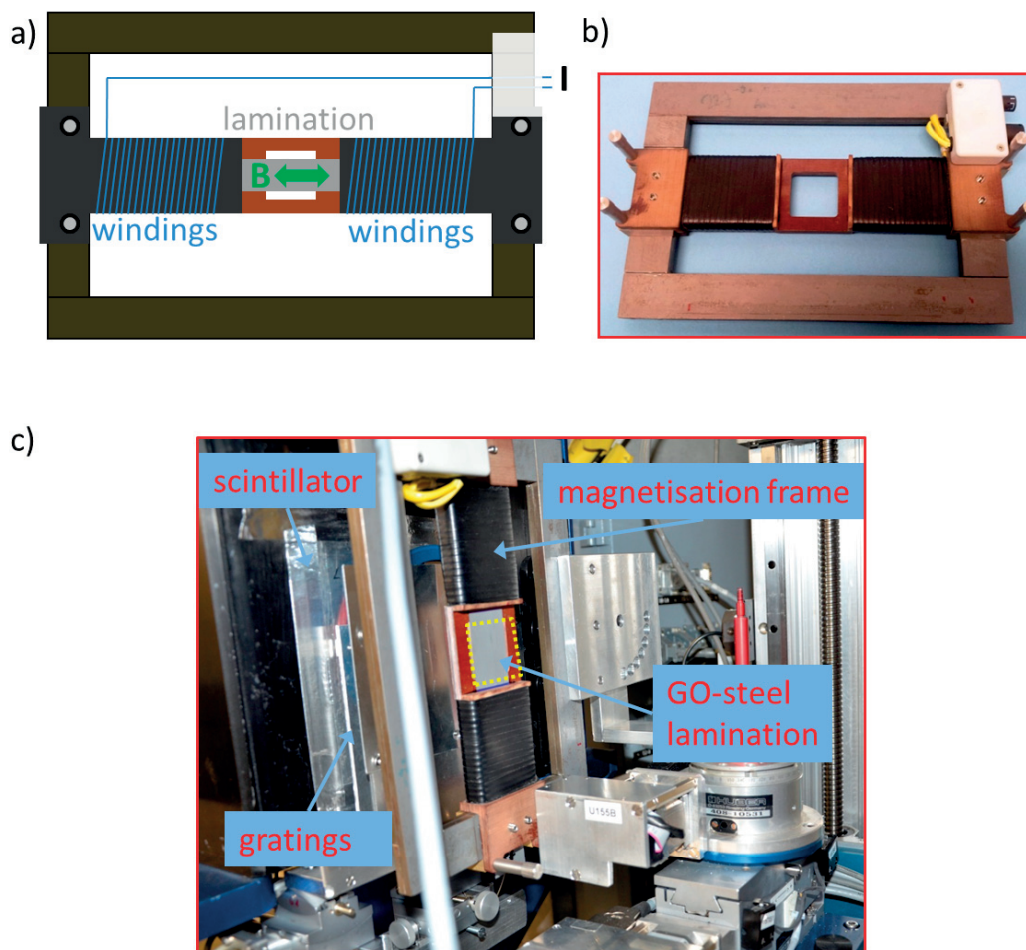
Figure 3.6: Magnetisation frame. a) Simplified drawing of the frame. Supplied by a current I, the windings induce a magnetic field B (green) in the sample (gray). b) Optical photograph of the frame without sample. c) The frame as mounted in front of the gratings and the scintillator. A GO-sheet is mounted inside the windings. By the application of a current to the windings, magnetic fields are induced and penetrate through the sample. The field of view is marked by the dotted yellow box.

---

[4]single sheet magnetic from Evico magnetics [122]
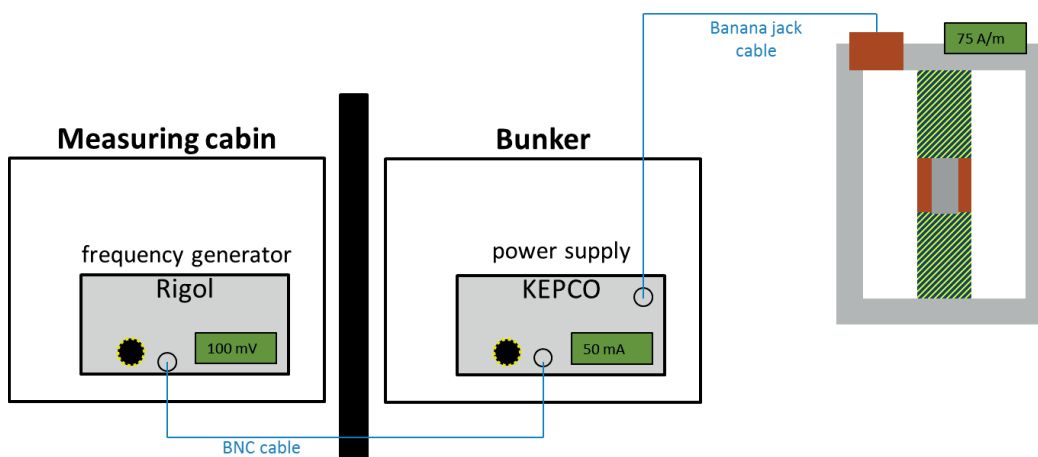
Figure 3.7: Frequency generator in the measuring cabin sending a voltage to the power supply in the bunker. The coils supplied with current induced a magnetic field in the sample. The conversion factor from applied voltage to observed magnetic field is 750 $\frac{A}{m \cdot V}$.

by DC- or AC-magnetic fields, depending on the applied current. An optical photograph of the frame is shown in b). Finally, c) shows the frame as it is placed directly in front of the grating setup (compare dashed square in Figure 2.10). The field of view in this experimental layout is 35 x 35 mm, limited by the magnetic frames window and indicated by the dashed, yellow box. The windings are supplied with a current up to 4A by a power supply (KEPCO BOP100-4ML), while the power supply itself is triggered by a frequency generator (Rigol DG4000). This generator is interfaced into the control software, allowing for the automated application of magnetic fields and measuring processes. The magnetic environment used in this way is able to apply theoretically currents of up to $\pm$ 4 A in DC- as well as in AC-mode[5] or even a combination of both. Consequently, a variety of signals, such as sinusoidal signals, ramp signals or square signals, to name only a few, can be applied using frequencies of up to 60 MHz. The sample is inserted into the frame such that the coils are wound around the sample as part of the frame. This can also be seen in Figure 3.6 a) and c).

When using the mentioned frequency generator, either a constant voltage (DC mode) can be set on the output or a sinusoidal oscillation with a frequency and an amplitude (AC mode). Both the offset and the oscillation can be superimposed as well, resulting in an oscillation with three independent parameters. A schematic of how the magnetic sample environment is connected and installed can be seen in Figure 3.7. The output-voltage signal from the frequency generator is transferred from the measuring cabin to the power supply, which is located inside the bunker, via a BNC cable. The input of a voltage of 100 mV into the power supply results in an output of 50 mA. The magnetic field produced by the frame, when supplied with 50 mA (banana jack cable), was in our case 75 A/m. Consequently the conversion factor from applied voltage to observed magnetic field was found to be 750 $\frac{A}{m \cdot V}$.

---

[5]Especially for AC-mode, it is not possible to apply 4 A, in order to avoid overload of the magnet.

3.2.2 For stress dependent measurements

The investigations under the influence of an externally applied mechanical force can be performed by the use of a **stress application environment**. This environment is based on a conventional translation stage, which was especially designed for use with neutrons.

The stress environment is schematically illustrated in Figure 3.8 a). The lamination is fixed at the bottom. The other side of the lamination is attached to two springs, which transfer the force onto the sheet. These springs are coupled via a load cell to the translation stage, which is able to pull on the whole construct. The load cell measures the applied force via the resistance of the cell. In b), an optical photograph of the stress environment is shown with a lamination schematically included in green. By the use of this translation stage up to 300 N can be applied. Images are taken by placing the whole stress environment into the beam with the sheet itself directly in front of the gratings (compare dotted square in Figure 2.10). The measured force can later be converted into a stress inside the sample using the samples' cross section[6].

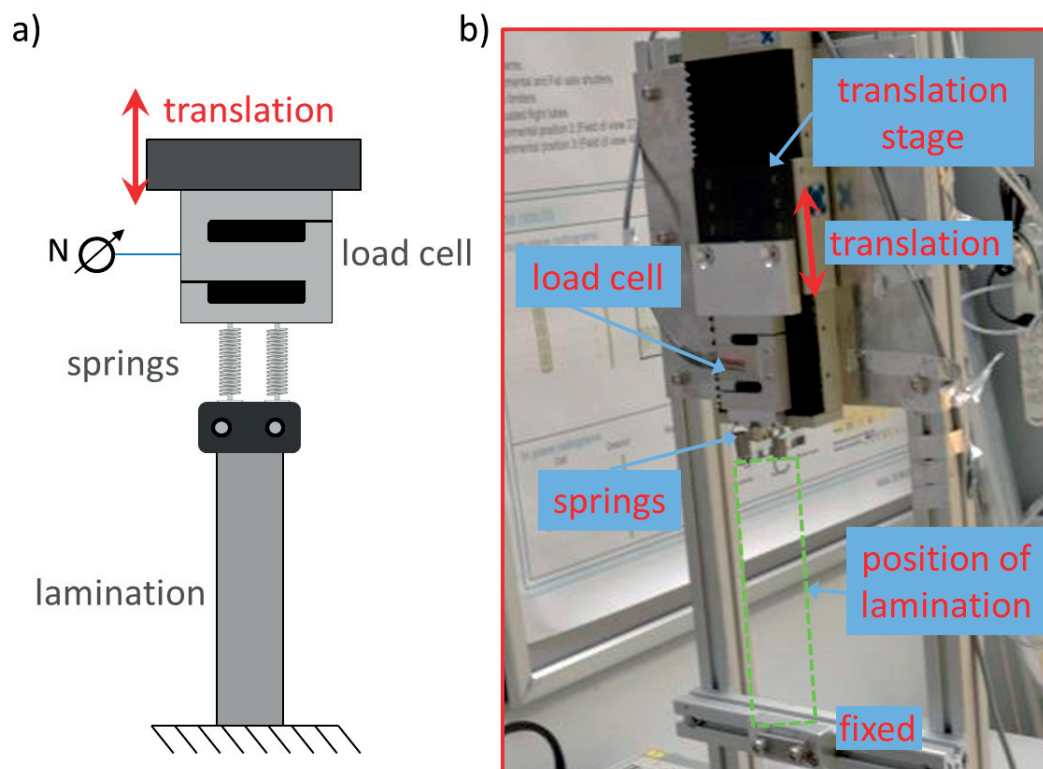**Figure 3.8:** Stress application environment. a) Schematic environment with the lamination fixed at the bottom and connected to springs on the top. Force applied by the movement of the translation stage and measured by the load cell. A force of up to 300 N can be applied. b) Optical photograph of the environment with the sample schematically included (green).

---

[6]For a detailed description see chapter 6.

3.3 Characterisation of the sensitivity range of the nGI setup

As calculated in section 2.5 the dark-field image visualises the scattering properties of samples in the small-angle and ultra-small-angle scattering range[7]. These angles correspond to correlations lengths from several hundred nanometers up to several tens of micrometers. While the nature of the formation of the DFI signal through small angle scattering is well understood, the quality of signal response and quantitative reliability of measurements over a range of sizes and concentrations of scattering structures is in the focus in the following [123]. First theoretical models for the calculation of the DFI signal concentrated on specific structures in particular spherical particles [124] or approaches to extract structural asymmetries [125] are performed. These were based on detailed wave propagation calculations and on modeling small angle scattering with a random Gaussian process, respectively. Results were exclusively compared to x-ray data up to now. A general theory accommodating earlier solutions for specific cases was recently provided by Strobl [126] and revealed that the dark-field signal can be interpreted as a Fourier back transformation of the scattering function from reciprocal space to real space. It has been shown that x-ray set-ups accurately probe scattering parameters in that way and provide real space correlation functions of the scattering structures sufficient for reliable characterisation and quantification, in particular also through available model based approaches.

3.3.1 Theoretical description

The DFI signal exponentially decays as a function of thickness [111], and can be expressed as the normalised visibility with V^s being the visibility with sample and V^{ob} without (compare Equation 2.55) as:

$$DFI = \frac{V^s}{V^{ob}} = e^{-\Omega \cdot t}. \tag{3.1}$$

Here, t represents the sample thickness and Ω is the material dependent dark-field coefficient [111] which can corresponding to theory [126] be expressed as

$$\Omega_{MCS} = -\Sigma^s(G(\xi) - 1), \tag{3.2}$$

where Σ^s is the macroscopic scattering cross section, G the real space correlation function of the scattering structure and the index MCS denotes the validity for monodisperse colloidal systems. The setup parameter ξ_{setup} defines at what correlation length the correlation function of the scattering structures is probed [126] with the chosen set-up parameters and is correspondingly given by:

$$\xi_{setup} = \frac{\lambda \cdot SDD_{eff}}{p_{fringe}}, \tag{3.3}$$

---

[7]It is also explained and analysed in section 4.2.3

where SDD_{eff} is the effective sample to detector distance and p_{fringe} the fringe period at the first Talbot distance d_T. As shown in [126] SDD_{eff} for a geometry with the sample in front of G_1 needs to be calculated, using the real sample to detector distance SDD, by:

$$SDD_{eff} = \frac{(l + d_T - SDD) \cdot d_T}{l}. \tag{3.4}$$

For a monodisperse system of spherical particles the macroscopic neutron scattering cross section can be written as

$$\Sigma^s = \frac{(3\pi^2)}{\lambda^2} \cdot C \cdot |\Delta n_{nuc}|^2 \cdot D, \tag{3.5}$$

with λ being the neutron wavelength, C the concentration in vol% of the particles in the D_2O/H_2O mixture, and $|\Delta n_{nuc}|$ the difference in the nuclear part of the refractive indices of mixture and polystyrene particles [126][124]. With the applicable real space correlation function G for spherical particles which vanishes for correlation lengths bigger than D, i.e. with $G(\xi_{setup} > D) = 0$ follows:

$$\Omega_{MCS} = \frac{3\pi^2}{\lambda^2} \cdot C \cdot |\Delta n_{nuc}|^2 \cdot \xi_{setup} \cdot \begin{cases} D' & \text{for } D \prec \xi_{setup} \\ D' - \sqrt{D'^2 - 1}(1 + \frac{1}{2D'^2}) + & \\ (D'^{-1} - \frac{1}{4D'^3}) \cdot ln\left[\frac{(D' + \sqrt{D'^2 - 1})}{(D' - \sqrt{D'^2 - 1})}\right] & \text{for } D \succ \xi_{setup} \end{cases} \tag{3.6}$$

where D' is the ratio between setup parameter ξ_{setup} and the particle diameter D with $D' = \frac{D}{\xi_{setup}}$. This equation is equivalent to the equations given in [124] for x-rays as well as with the description given in [126] for the corresponding specific case of isolated hard spheres as scattering particles.

For our experimental conditions with $\lambda = 4.1$Å, $SDD = 25mm$ and $p_{fringe} = 4\mu m$ the setup parameter ξ_{setup} turns out to be $2.048\mu m$. The refractive index n_{nuc} is given by [55]:

$$n_{nuc} = 1 - \frac{\lambda^2}{2\pi} \cdot n_{SLD}. \tag{3.7}$$

Here the neutron scattering length densities[8] n_{SLD} are taken from the NIST database [84]. Together with the known setup parameters (ξ_{setup}, λ, SDD and p_{fringe}) and the sample parameters (particle material, diameter D and concentration C as well as the solution composition (D_2O/H_2O mixture)) one can calculate the DFI signal according to the equations 3.1 and 3.6.

---

[8]$C_8H_8 : 1.399x10^{-6}$Å^{-2}; $mixture : 2.282x10^{-6}$Å^{-2}

3.3.2 Experimental results on particle size sensitivity

Experiments are performed on mono-dispersed polystyrene particles[9] as solute in a mixture of D_2O and H_2O (41 vol% : 59 vol%) contained in a 5 mm thick quartz cuvette. This solvent is chosen, to prevent the particles from sedimentation or flooding as the density of the solution and the particles matches, allowing assuming a homogeneous distribution and constant concentration over the whole probed volume. The measurements were performed using aqueous solutions (D_2O/H_2O) with particle diameters (NIST traceable size standards) of 110 nm, 500 nm, 770 nm, $1\mu m$, 2 μm, 3 μm, 4 μm, 5 μm, 7 μm, each with a concentration of 9 vol%. The interaction of the neutrons with the particle solution leads to scattering in the SANS and USANS regimes resulting in a loss of coherence of the exiting neutron wave front. The reduced coherence results in a locally degraded interference pattern behind G_1 which is finally detected in the DFI. For the measurements G_0 was stepped over one period in 16 steps with an exposure time of 45s per phase step.

The TI of an empty quartz glass cuvette (5 mm thickness), one filled with solely the D_2O/H_2O mixture, and the ones filled with the solutions containing different diameters of particles is shown in Figure 3.9 a). Here, the presented TI is stitched together from 5 single TIs in width. The empty cuvette hardly attenuates the neutrons at all, apart from the side walls and stoppers,

Figure 3.9: a) TI showing an empty quartz glass cuvette, a cuvette filled with the D_2O/H_2O homoge-neous mixture, and cuvettes with particle solutions with varying diameter from 0.11 μm up to 7 μm. No obvious contrast difference between the different particle size solutions is obtained in TI. b) DFI of the same cuvettes as in the TI above. In contrast to the TI results the DFI shows clear differences for varying particle sizes. In both images the aluminum holder is slightly visible in the lower part.

---

[9]NIST traceable standards 2 % uncertainty of mono-dispersity

while the filled cuvettes reduce the transmission signal to about 0.23 for both pure aqueous mix and particle solutions, which is due to the beam attenuation by the aqueous solution mainly.

The DFI of the same cuvettes is shown in Figure 3.9 b). Looking at the empty cuvette, again only the edges of the cuvette and the stopper show a contribution in the DFI, while the critical volume which will be filled with the investigated samples does show only a marginal contribution. The aqueous mixture without colloids however reduces the DFI signal to a value of about 0.9, i.e. by 10% in the probed volume. This is due to inelastic scattering of water, which contributes significantly to a sample dependent background in the small angle scattering. This additional and not structure dependent scattering occurs also in the cuvettes containing particles. In order to quantify the scattering from the particles only, according to the theory given above, the DFI values have been corrected for this background contribution by normalisation to the values measured with the pure aqueous solution.

The corresponding DFI contribution measured in the cuvettes with the solutions of different particle diameters clearly varies and ranges from 0.31 to 0.85. This reduction of the DFI signal is due to the elastic coherent small-angle and ultra-small angle scattering signal of neutrons from the polystyrene particles in solution. The diameters of the different particles lead to different scattering distribution and hence the DFI sensitivity concerning the particle sizes can be examined quantitatively and compared to theory.

To quantitatively analyse the particle size sensitivity of the DFI, the mean value was normalised over a limited region of interest of each particle solution (see dashed box in Figure 3.9 in the DFI of 1 μm particles in solution) to the one from the pure D_2O/H_2O mixture as described; hence only the structure dependent coherent scattering contribution without the inelastic background induced by the aqueous solvent is analysed. Each measurement was performed seven times in order to increase the accuracy of the obtained values and the statistics. The corresponding data are shown in Figure 3.10, where the averaged experimentally determined DFI (blue squares) and TI values (inset) are plotted versus the particle diameter. The standard deviations of the seven measurements are given as error bars.

The inset in Figure 3.10 shows the transmission signal by the solutions in more detail. The signal is plotted versus the diameter of the probed particles. The constant (particle independent) reduction of the signal in the TI to about 0.23 for both, solution with and without particles, shows not only the independence of the TI signal of the particle sizes, but also the low and not measurable sensitivity of the attenuation of the particles in solution. The green line in the inset in Figure 3.10 is the average transmission value of all solutions.

Whereas the DFI signal for the 0.11 μm particles displays only little contrast with a value of 0.94, a rapidly decreasing DFI value is obtained for increasing particle sizes with a minimum DFI value of 0.34 obtained for particle sizes of 4 μm. For larger particle sizes than 4 μm the DFI signal starts to slightly increase again and reaches a value of 0.41 for the 7 μm particles. The result of the theoretical calculations (from equation 3.6) of the DFI signal behavior according to particle diameters is shown in Figure 3.10 as the red line for direct comparison. The experimental data are in good agreement with this theoretical prediction of the DFI signal dependence on the particle size. Both the experimental data as well as the theory show a

turning point in the DFI value. The theoretical value of the particle size for the minimum DFI value is at 3.6 μm. This value is strongly dependent on the set-up parameter ξ_{setup} which can hence be used to tune the sensitivity of a grating interferometer to different size ranges of scattering structures. The good agreement with theory underlines the good calibration and tuning potential of the set-up for quantitative studies. The range of particle sizes for which the measurements reproduce theoretical predictions accurately in addition proves the significant range in which the method can be applied with sufficient sensitivity and accuracy to provide quantitative results.
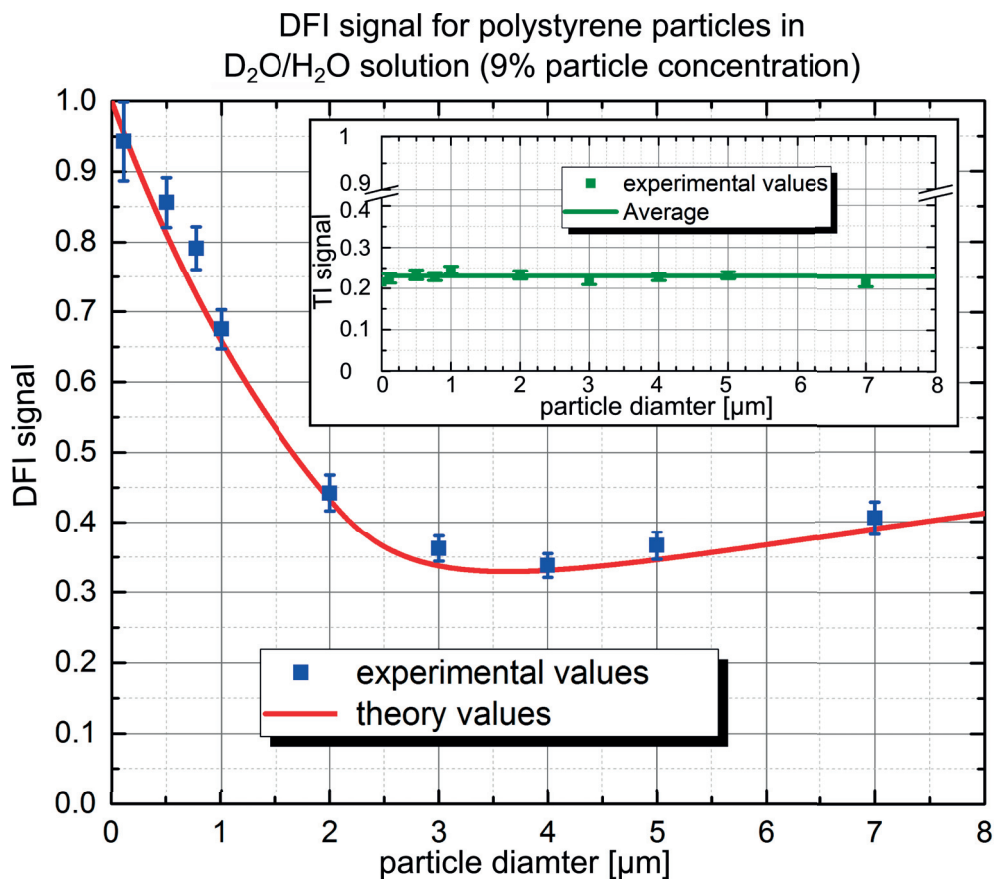
Figure 3.10: Behaviour of the dark-field signal for increasing particle diameters. The experimental values (blue squares) are in good agreement with the theoretical description (red line). Each measurement was performed seven times in order to increase the accuracy of the obtained values and the statistics. The standard deviations of the seven measurements are given as error bars. The highest DFI sensitivity is between approximately 3 to 5 μm, while the length scale where the nGI setup with the used setup parameters is sensitive and quantitative ranges over the full probed range from hundred nanometers up to several micrometers. The obtained contrast values for the TIs are shown in the inset. They reveal a constant behavior (green squares) not depending on the solved particle's diameter. The average value of the TI signal is shown as green line.

3.3.3 Experimental results on concentration dependence

A second run of experiments was performed, to study the behaviour of the DFI signal for different concentrations of particles in solution. All the setup parameters stayed the same like in the first run (previous section) of experiments. In addition to the different particle sizes that were investigated, now the concentration was altered. Solutions with particle concentrations of 12 %, 6 % and 3 % were investigated and the results are shown in Figure 3.11. Representativly the TIs and DFIs for 1 μm and 2 μm are shown out of the assembly of cuvettes. As expected, no differences are visible in the TI, as already previous results showed the insensitivity of the attenuation signal to the particles, whereas the DFI shows
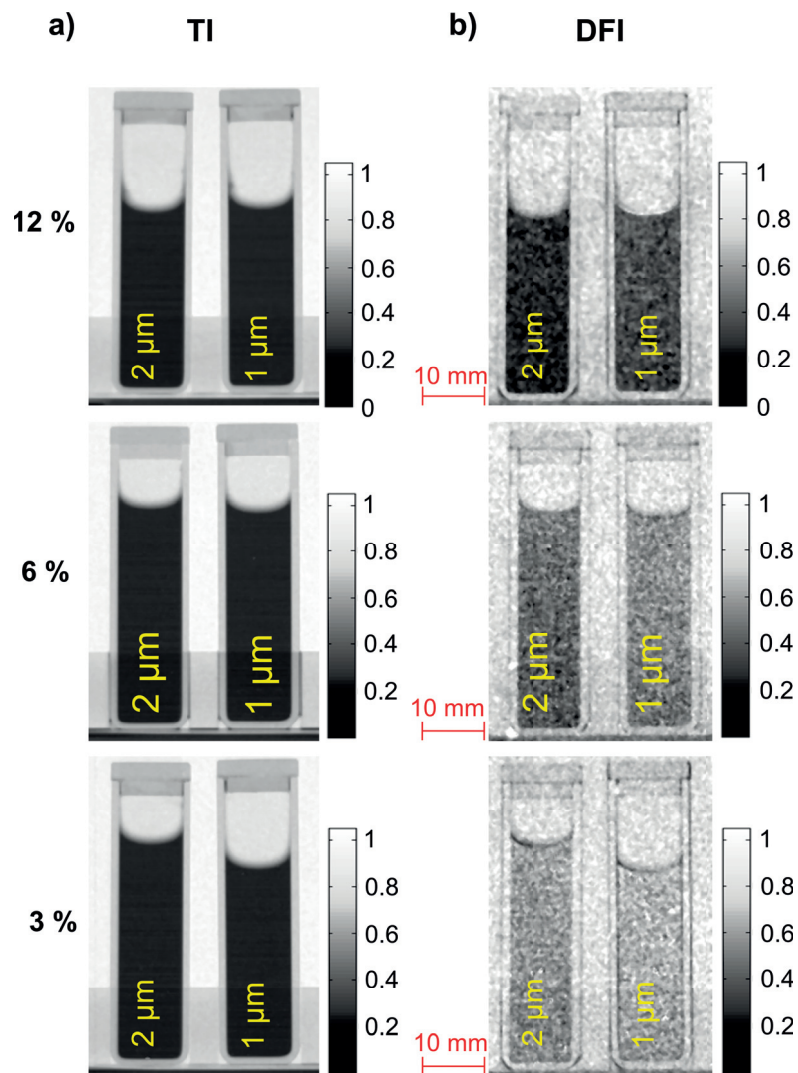
Figure 3.11: a) TIs of solutions containing 1 μm and 2 μm particles with different particle concentrations of 12%, 6% and 3%. b) DFI of the same cuvettes. In the TI again no significant differences occur due to the change in concentration, while in the DFI a concentration dependent signal is observed.
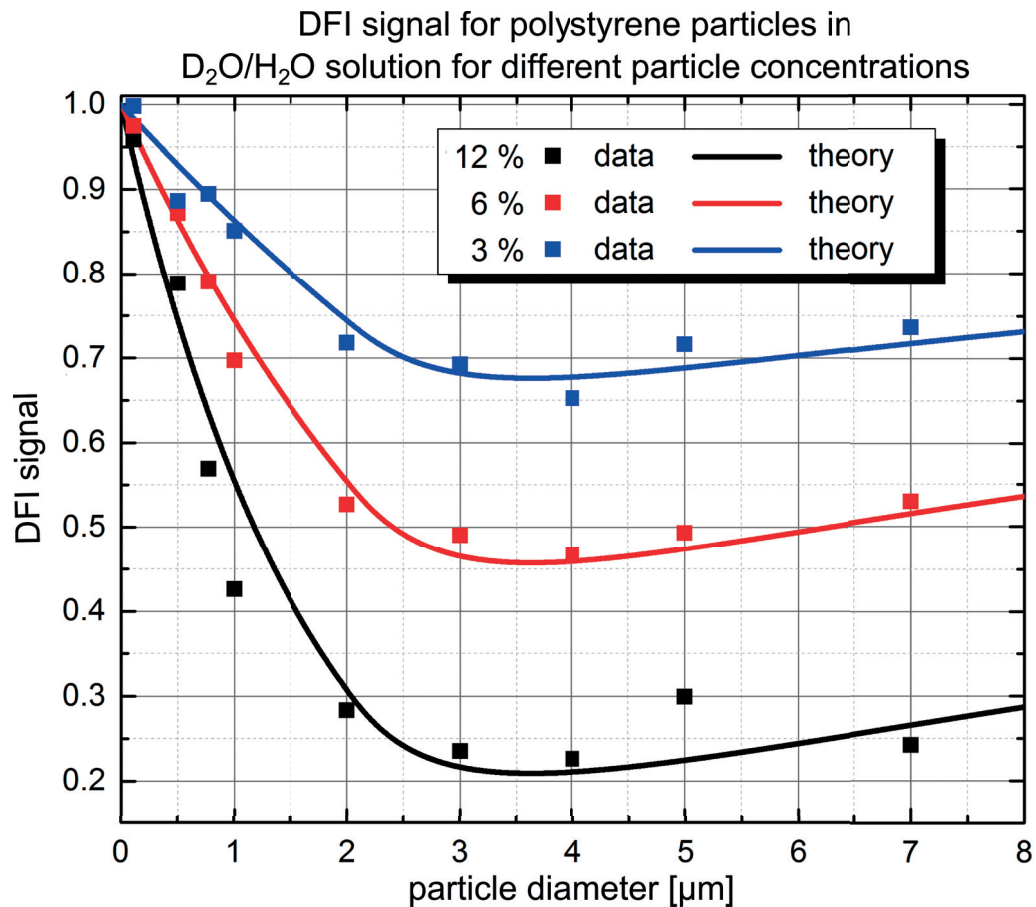
Figure 3.12: Concentration dependent experimental results (squares) of the DFI signal versus parti-
cle diameter. The corresponding theoretical calculations (lines) are included too. The
decreasing concentration mitigates the sensitivity as expected, but does not change the
range in which quantitative results could be obtained.

a concentration dependent behaviour with, as has to be expected due to the increasing
macroscopic scattering cross section and hence scattering contributions, the smallest DFI
values for the highest concentration.

The quantitative results of the concentration dependence are shown in Figure 3.12 including
the calculated theoretical values. Lowering the concentration results in a smaller interaction
probability and hence in a larger DFI value independent of the particle size. Note, that the
particle size behaviour stays qualitatively the same independent of the concentration. The
theoretical model describes all three measurements well.

The quantification of the dark-field signal concerning particle diameters has been performed by the use of mono-dispersive polystyrene particles in solution. The sensitivity of the method and set-up to a significant range of length scales has been demonstrated through an accurate quantitative matching of experimental data with theoretical predictions. This underlines not only the potential of quantitative measurements with nGIs but also underlines the reliability and accuracy of results in the investigated size range. The same has been found valid for a range of particle concentrations and hence for altering the macroscopic scattering cross section, which proofs that quantification of both, size and concentration but in principle also scattering length contrast of scattering structures is potentially possible with neutron DFI with good quantitative accuracy. The experimental characterisation and the found consistency of measurements with theory pave the way for non-destructive investigations of, for example porous media and the determination of their pore size as well as the concentration of pores with spatial resolution, to name just one wide field of applications. In addition, based on these results, the set-up parameters can be used to shift the maximum sensitivity of the set-up to the range of interest in a specific study and to hence optimise measurements for certain applications. Furthermore estimates of feasibility for sample investigations can be given more precisely by the gained knowledge.

4 Experiments I: *Static* magnetisation process of Goss-oriented electrical steels in magnetic DC - fields

The following chapter reports on the investigation of the locally resolved response of both, bulk basic and supplementary magnetic domain structures to externally applied magnetic fields. They are visualised in the dark-field image in-situ by neutron grating interferometry. Hysteresis effects were investigated and a correlation of grain misorientation and dark-field value was derived. To compare and to verify the DFI findings and their interpretation, more conventional, complementary surface-sensitive magneto-optical Kerr-microscopy investigations, optical Faraday imaging experiments, small-angle neutron scattering experiments and crystallographic Laue X-Ray diffraction experiments were performed. The results are based and continue with the work published in [127].

4.1 Neutron grating interferometry results

For the investigation of the response of the magnetic domain structure to externally applied magnetic fields the modified setup (compare section 3.1.2) is used in combination with the magnetisation frame. Figure 4.1 shows a schematic of the setup. The gratings are used in combination with a 100 μm thick ^{6}LiF/ZnS scintillator screen and a digital camera [Andor NEO sCMOS, 2160 x 2560 pixels, pixel size: 6.5 μm]. The effective spatial resolution of 70 μm is the result of intrinsic blurring of the scintillation screen, the optical system, and penumbra blurring caused by the sample to detector distance of $\approx$ 3 cm [128]. The C 130-30 GO-steel lamination is inserted into the magnetisation frame. The frame itself is mounted directly in front of G_1 (compare Figure 2.10). The field of view in the experiments is 35 x 35 mm, limited by the magnetic frame window (Figure 4.1, yellow dotted square).

In Figure 4.2 a) a conventional transmission image (TI) of a GO-steel lamination is shown. The 300 μm thick lamination provides a weak but homogeneous contrast. Note that the contrast in the TI is scaled from 0.9 to 1.0. The corresponding DFI of the same lamination is shown in Figure 4.2 b). In contrast to the attenuation based TI, a pronounced heterogeneous contrast with sharp features is observed in the DFI. The vertical black line pattern represents elongated basic magnetic volume domains, while the lines themselves are the domain walls.
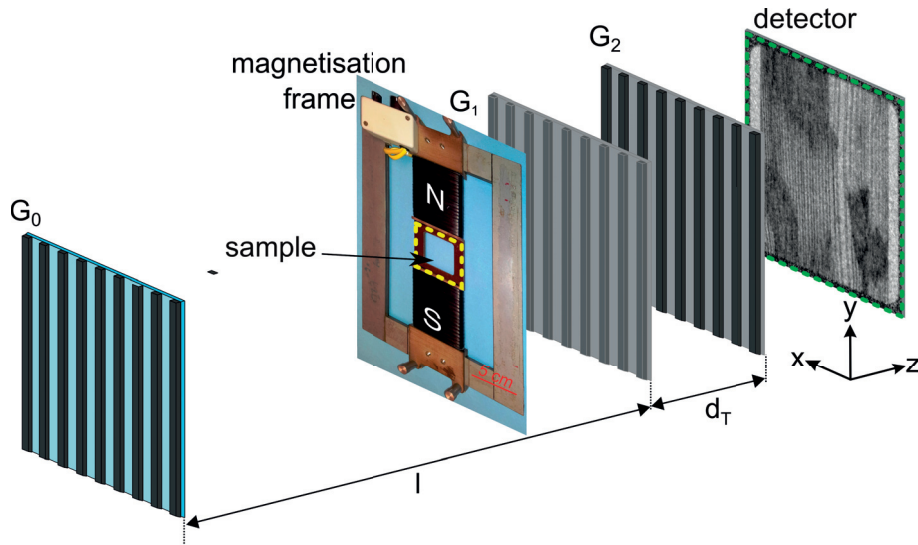
Figure 4.1: Schematic of the neutron grating interferometer for the investigation of a C 130-30 GO-steel lamination. The source grating, G_0, is placed at a distance l from the phase grating, G_1. The analyser grating, G_2, is located at first the Talbot distance, d_T, from G_1. The magnetisation frame is mounted as close as possible in front of G_1. The images are recorded by a neutron imaging detection system with a scintillator screen and a digital camera.

As mentioned previously in chapter 2, the magnetisation of the basic domains points along the magnetic easy axis. The magnetic easy axis is the [001]-direction of the crystalline structure and points along the vertical axis in the shown DFI. These basic domains are found with a domain wall spacing, the distance between the individual walls, larger than the detector resolution. They are consequently visualised individually. Furthermore, areas with a decreased DFI signal are found in the image. These areas are misoriented grains where supplementary
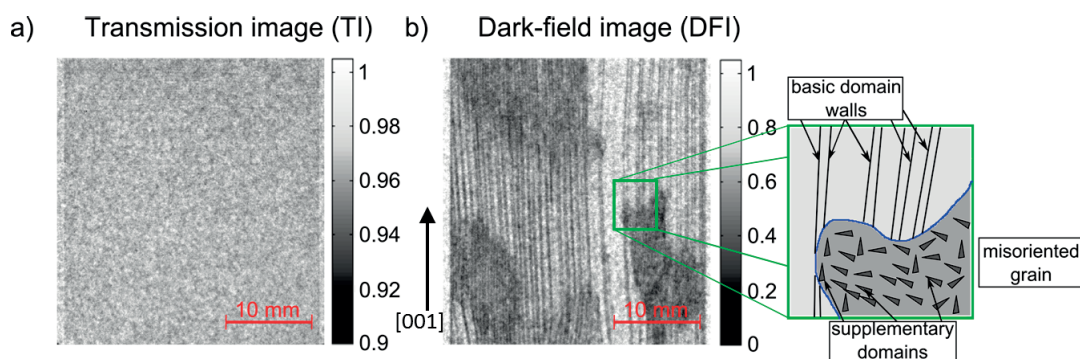
Figure 4.2: a) Transmission image of a GO-steel lamination showing a weak and homogeneous attenuation. Note the contrast is scaled from 0.9 - 1. b) DFI of the same lamination providing a pronounced contrast with dedicated features. Black line patterns represent the walls of elongated magnetic domains. Areas with reduced DFI signal originate from unresolved supplementary domain structures in misoriented grains. The schematic on the right illustrates the basic domain walls as the observed black lines. The misoriented grain with triangular shaped supplementary domains is also sketched.

domains are generated for the reduction of magnetic stray fields[1]. Such an agglomeration of supplementary domains, with a domain wall distance smaller than the detector resolution, contributes to an average degradation of the DFI (compare section 2.5.3). Consequently, the DFI signal reduction is interpreted as a higher relative density of domain walls. The schematic on the right illustrates the basic domain walls in ideally oriented grains as black lines as they are observed in the DFI. In the misoriented grain, triangular shaped supplementary domains are shown.

4.1.1 DFI results of the initial magnetisation curve

As stated in chapter 1 , GO-steels are commonly characterised by recording inductive magnetic B-H-loops. In Figure 4.3 the first quadrant of a hysteresis loop recorded at 50 Hz (black line) is shown. From this measurement, global information such as the saturation polarisation or the permeability can be obtained. However, the underlying domain structure inside the GO-steel sheet that determines these global magnetic properties remains undiscovered. The DFIs fo the visualisation of the bulk domain structure were recorded at different positions of the initial magnetisation curve, starting with a demagnetised lamination[2] and respectively increasing the externally applied field. The blue squares in Figure 4.3 indicate the field values where the individual DFIs were recorded. Due to the prior demagnetisation of the lamination, they are located on the initial magnetisation curve.
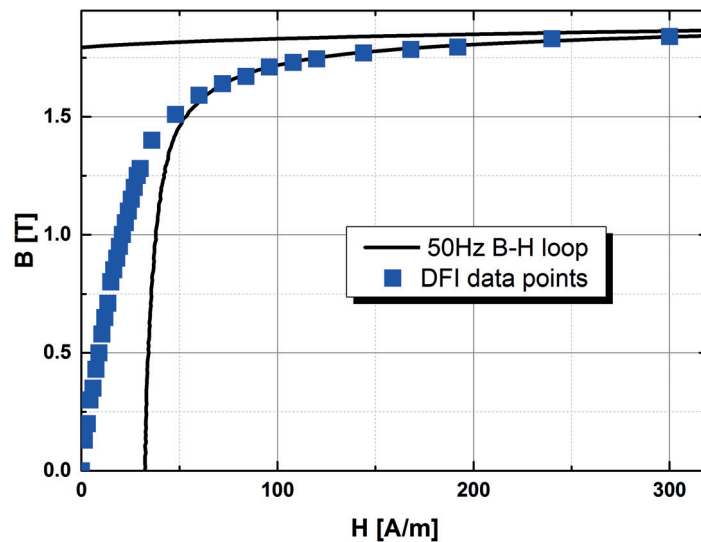
Figure 4.3: Conventional B-H-loop measurements (first quadrant) recorded at 50 Hz of a GO-steel lamination (black line). Blue squares mark where on the initial magnetisation curve the DFIs were recorded according to stepwise increasing magnetic field values.

---

[1]This will be investigated in more detail in section 4.2 with the help of alternative, well-established techniques; Compare also chapter 2

[2]Demagnetisation is performed by the application of a magnetic AC- field with a frequency of 30 Hz while the amplitude of the AC oscillation is continuously decreased.
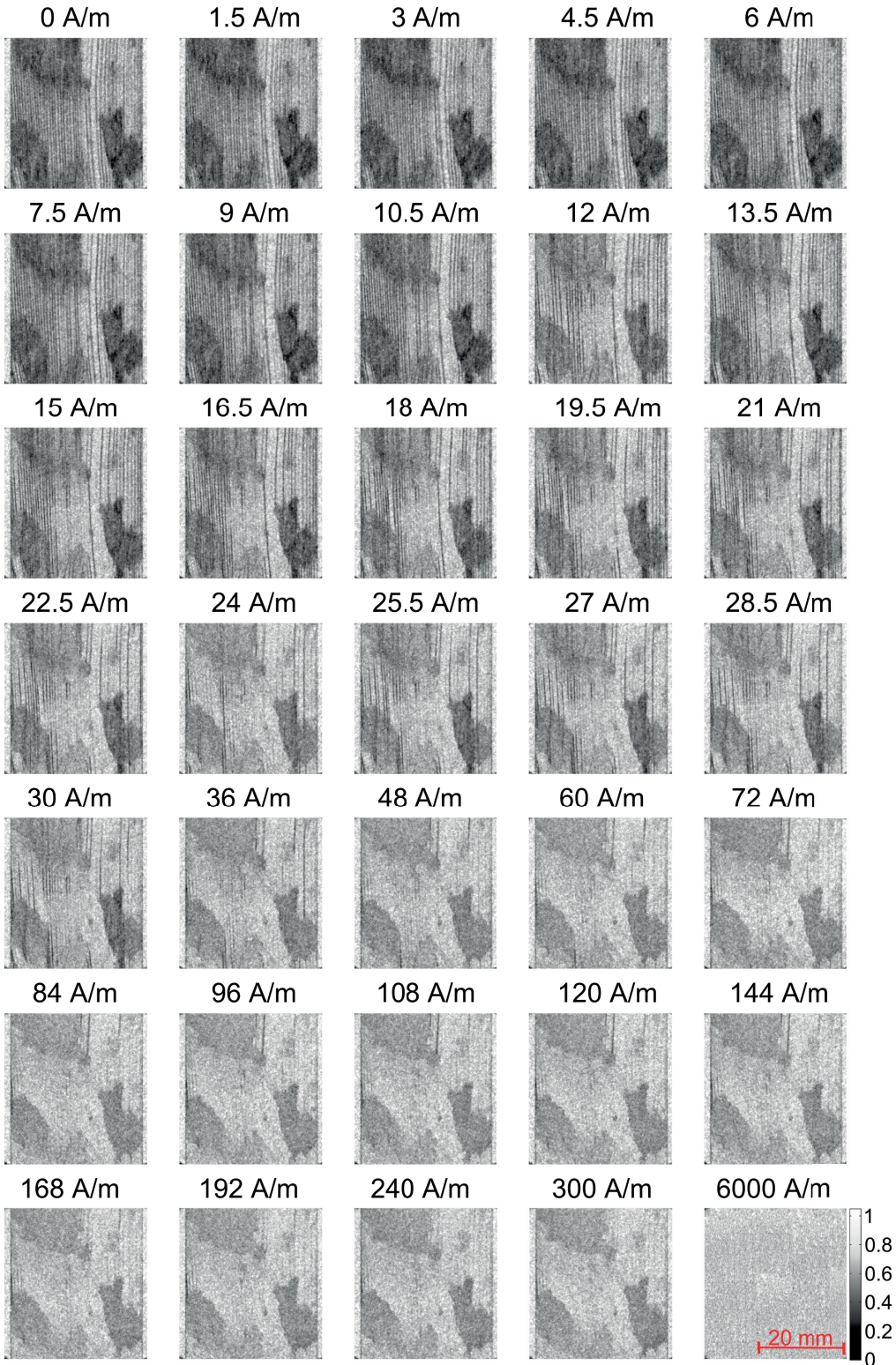
Figure 4.4: In-situ visualisation of the bulk domain wall structure of a GO-steel lamination and its changes during magnetisation. DFIs for increasing magnetic fields values from H = 0 A/m to H = 6000 A/m are shown consecutively. The DFIs show large vertically elongated domains, by black lines, representing the basic domain walls. Misoriented grains appear as dark areas in the DFIs due to the supplementary domains. Increasing fields lead to vanishing domain walls.

Figure 4.4 shows the corresponding DFIs of the GO-steel sheet as marked by the blue squares in Figure 4.3. The obtained DFIs locally visualise the static volume domain structure in the GO-steel. Each DFI presents a dedicated state of the inner magnetic domain structure during static magnetisation for increasing field values (blue squares in Figure 4.3) along the initial magnetisation curve. In the image without magnetic field applied at H = 0 A/m, large elongated domain structures are visible. Vertical black lines still represent the basic domain walls. Likewise, misoriented grains containing supplementary domains can be identified as areas with reduced DFI signal. Stepwise increasing the applied magnetic field to values up to 6 A/m does not induce visible changes in the domain structure. For magnetic fields values from 7.5 A/m to 13.5 A/m several basic domain walls in the middle of the sheet vanish. The remaining basic domain walls either end at grain boundaries or penetrate misoriented grains and build an underlying structure in addition to the supplementary domains. This cancellation of basic domain walls is continued for a further increase in the applied field starting from the center of the lamination towards the vertical edges up to 48 A/m. Applying a field of 48 A/m virtually all basic domain walls disappeared. Due to the magnetic flux that needs to be transported along the GO-steel sheet, domains pointing in the direction parallel to the direction of the externally applied static magnetic field need to grow at the cost of those pointing in the opposite direction (compare Zeeman energy E_{Ze} in section 2.2). The growth of domains, equivalent to the motion of the domain walls, is visible as changes in the magnetic domain walls structure. Due to the pinning of the volume domain walls, their sudden unsnapping (Barkhausen jumps [129]) during magnetisation, and the large exposure time of each single DFI (approximately 25 minutes), the instantaneous jumps of the domain walls appear as a continuous change of the domain structure in the corresponding DFIs. The vanishing of the domain walls starting from the middle of the sheet can be explained by the transported magnetic flux being larger in the middle part of the lamination due to the non-uniform magnetic field distribution inside the lamination [130]. The contrast provided by the misoriented grains only changes because of the underlying basic domain structure, while the contrast originating from the supplementary domains remains constant. Increasing the applied magnetic field further, no significant changes in the basic domain's structure occur up to 300 A/m applied field.

The three misoriented grains as visible in all DFIs start getting brighter for fields from 72 A/m up to 300 A/m with increasing field values. These three grains have different misorientations leading to different amounts of contrast reduction; hence, the DFI values directly correlate with the misorientation angle ϑ_s [3] via the supplementary domain wall density. This is in good agreement with recently reported, surface-sensitive Kerr imaging results on such material [131]. A fully magnetised GO-steel lamination is shown in the DFI at H = 6000 A/m. Here the lamination is in its "single-domain"-state, resulting in no visible contrast in the DFI. The fact that no contrast at all is generated for high fields gives furthermore the proof, that all the contrast in all DFIs is of magnetic origin.

As seen in Figure 4.4, the changes of the volume domain structure take place predominantly at field values between H = 0 A/m and H = 48 A/m. The "knee" of the magnetisation curve B_K

---

[3]compare equation 2.1 ; A detailed investigation will follow in section 4.2

is defined by

$$B_K = \frac{1}{\sqrt{2}} \cdot B_S \qquad (4.1)$$

where B_S is the saturation magnetisation [81]. With the saturation magnetisation $B_S = 1.90$ T for GO-steels, the value of the knee results in $B_K = 1.34$ T. This corresponds to an applied field of approximately 50 A/m. According to section 2.2 the contribution of wall motion to the magnetisation process is vanishing for high magnetic fields. Predominantly rotations of magnetisation of domains occurs above the "'knee"'. These rotations are not visible in the DFIs since not the magnetisation itself but the domain walls are visualised.

In the DFI results in Figure 4.4, the volume basic domain structure vanishes in the same magnetic field range, giving evidence of the accuracy of the performed neutron grating interferometry measurements.

4.1.2   DFI results of the hysteresis loop

To study the hysteretic behaviour of domain walls in the GO-steel lamination, the applied magnetic field is statically decreased, starting from the "single-domain"-state as observed in the DFI with H = 6000 A/m in Figure 4.4.

For the comparison of the magnetic domain structure in increasing and decreasing fields the DFIs of the initial magnetisation curve are compared to the DFIs taken on the hysteric slope back to zero applied field [127]. For the illustration of the changes, Figure 4.5 shows again
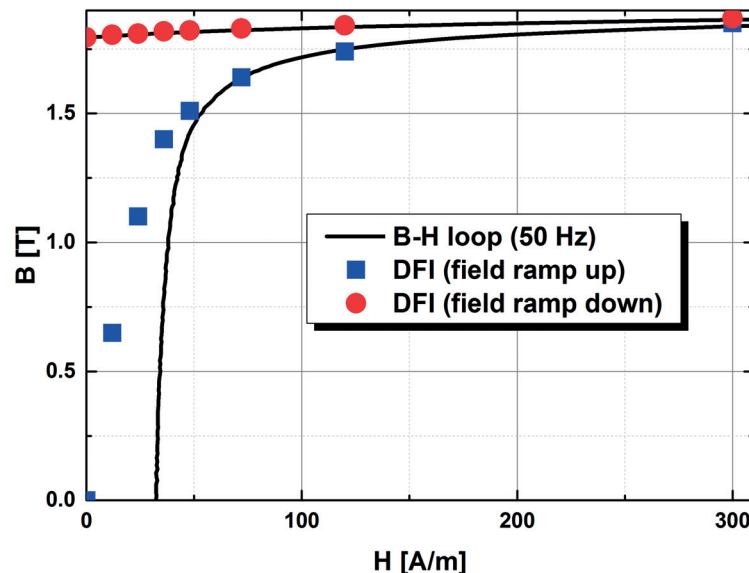

Figure 4.5: Conventional B-H-loop measurements (first quadrant) recorded at 50 Hz of a GO-steel lamination (black line). Blue squares mark where the DFIs were recorded for increasing field values. Red circles mark where the DFIs for decreasing fields were obtained.

the first quadrant of a hysteresis loop. This time with only some blue squares[4] marking the location of DFIs in increasing fields and red circles marking those DFIs taken in decreasing fields.

The corresponding DFIs for increasing and decreasing fields can be found in the left (blue arrow) and the right (red arrow) columns of Figure 4.6 respectively. The contrast of the misoriented grains, containing the supplementary domains reappears immediately at $H_d = 300_d$ A/m (index d for decreasing field). As seen in the B-H-loop in Figure 4.5, no significant flux changes (difference of y-value in Figure 4.5) occur between increasing and decreasing magnetic field values at H = 300 A/m which results in only a slightly different basic domain arrangement. Further decreasing the magnetic field H_d leads to a recurrence of basic domain walls. Hysteretic effects can be visualised by comparing the DFIs for the same value of the applied magnetic field for increasing and decreasing field history.

The differences in the basic domains structure in the DFIs for the pairwise correlation of increasing and decreasing field values are clearly visible. It is known that the basic domain structure depends on the magnetic flux that needs to be transported over the GO-steel lamination [70]. The magnetic flux difference ($\Delta B = B_d - B$) increases for smaller values of applied magnetic field (compare Figure 4.5). This effect is similarly reflected in the individual DFIs by a smaller number of basic domain walls and an asymmetric, non-periodic width distribution of basic domains in decreasing fields (especially seen in the left half of the DFI with 12 A/m applied field). The small supplementary domains in the misaligned grains do not contribute significantly to the magnetic flux transport. This results in no visible difference in the contrast for the images taken with increasing or decreasing field history. Only slight changes due to the underlying basic domain structure occur, while these changes in contrast are not related to the supplementary domains themselves. Note, that the DFI at $H_d = 0_d$ A/m shows the remanent state of the GO-steel lamination. The initially observed magnetic state in the DFI at H = 0 A/m is almost entirely reproduced in the DFI of the demagnetised state. The GO-steel lamination was finally demagnetised by applying an AC-magnetic field with a frequency of 30 Hz and an continuously decreasing field amplitude.

---

[4] only those points are included, which are compared as DFI in Figure 4.6
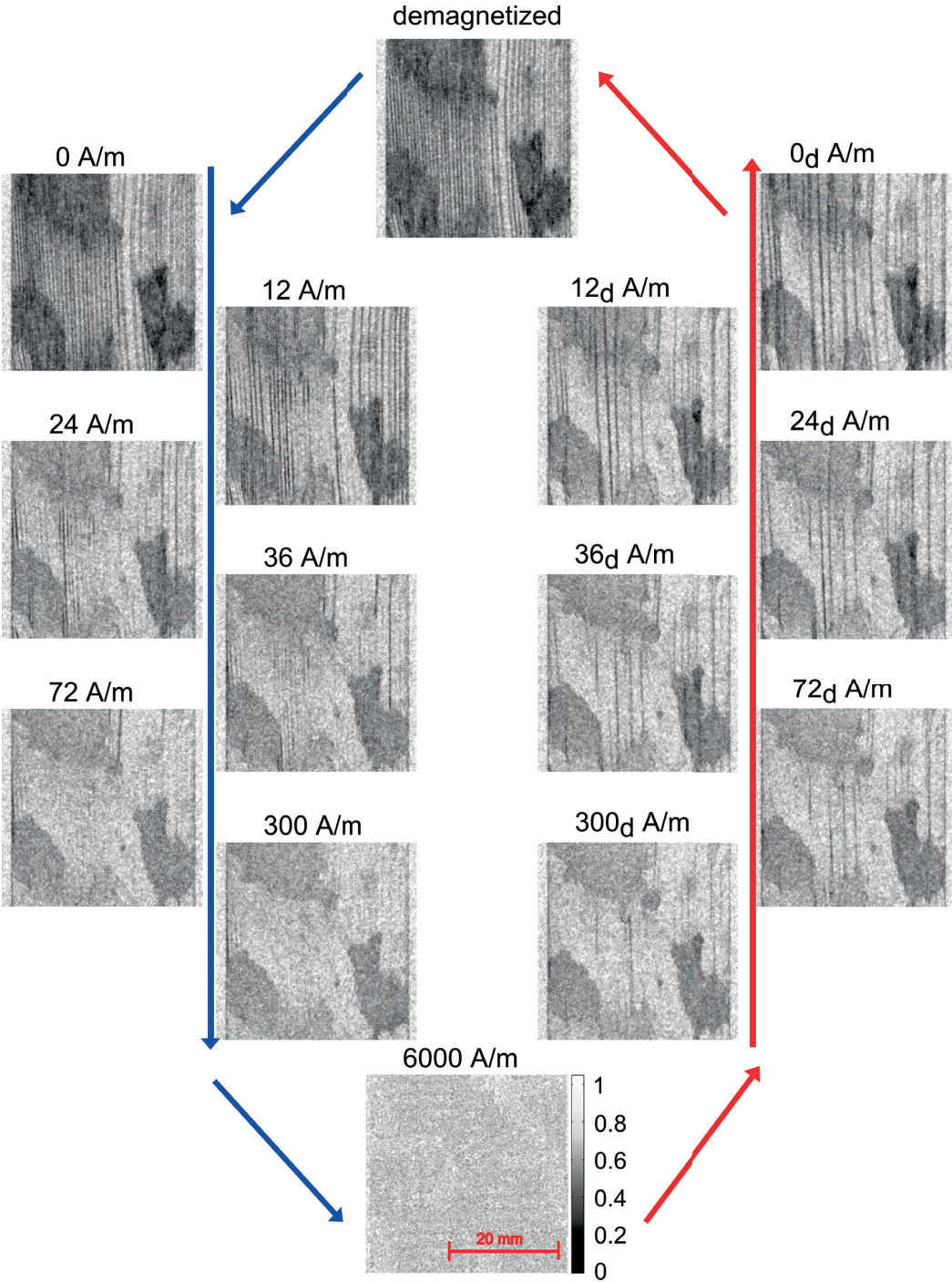
Figure 4.6: In-situ visualisation of the hysteretic bulk domain wall structure of a GO-steel lamination and its changes during magnetisation. In the left columns the DFIs for increasing magnetic field values from H = 0 A/m to H = 6000 A/m are shown consecutively. The DFIs show large vertically elongated domains by black lines, representing the domain walls. Misoriented grains appear as dark areas in the DFIs. In the right columns, the DFIs in decreasing field (denoted by index d) are shown for the same values as the DFIs in increasing fields. The remanent state is the DFI denoted with $0_d A/m$ while the demagnetised state can be found on the top of the Figure.

4.2 Complementary measurements

To verify the DFI findings from the previous section, complementary experiments using well-established investigation techniques were conducted. Those were in detail: (i) Kerr microscopy experiments to study the surface domain structure, (ii) Faraday imaging to detect magnetic stray fields with high resolution and to reveal the superposition of supplementary domains onto the basic domain structure, (iii) small-angle neutron scattering (SANS) experiments to access volume information about the interaction of neutrons with the magnetic domain walls and (iv) X-ray Laue diffraction (XRD) experiments to reveal the crystallographic orientation of individual grains.

4.2.1 Magneto-optical-Kerr-microscopy

A Kerr-microscope uses the magneto optical Kerr effect for the visualisation of magnetic domains [67]: When a magnetic material is illuminated with linear polarised light, the polarisation of the light is rotated by the magnetisation, as shown in Figure 4.7. The rotation angle depends on the material and on the magnetisation M relative to the plane of polarisation of the incidence light beam. This is illustrated in Figure 4.7 a). Incoming light is linearly polarised and gets reflected at two magnetic domains providing opposite magnetisations (M and $-M$). At the first domain (red) the polarisation of the reflected light is rotated about an angle θ (yellow) and at the second domain (blue) about an angle $-\theta$ (green).

Due to a suitable alignment of a polariser and an analyser the rotation of the lights' polarisation plane can be studied. Thus, some magnetic domains having one particular magnetisation will
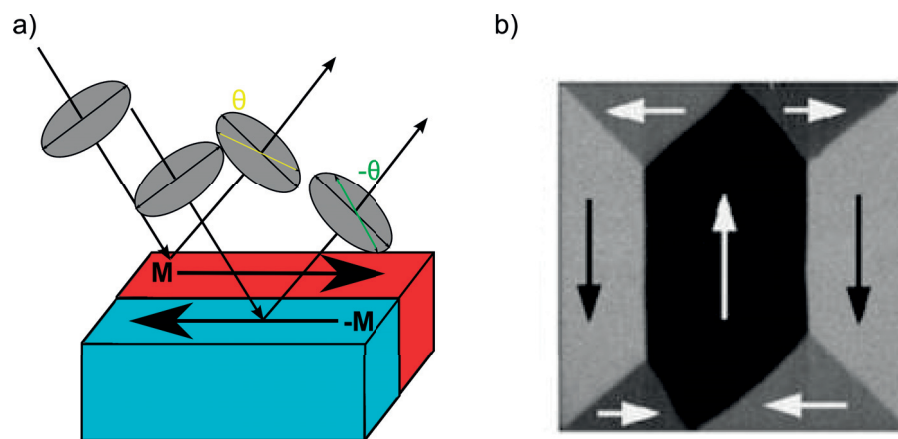
Figure 4.7: The magneto-optical Kerr effect. a) Two linear polarised incoming light beams get reflected at a sample surface with magnetisation M or $-M$. The polarisation plane of the reflected beams is rotated about an angle θ (yellow) or $-\theta$ (green), depending on the magnetisation M and $-M$ of the two opposite magnetic domains. Analysing the polarisation plane results in some domains appearing bright other dark. b) Shows an exemplary Kerr image of a sample, where seven domains with four different magnetisation directions are visible, with a gray value corresponding to the respective magnetisation [70].

appear bright while domains providing other magnetisation will appear dark. This can be seen exemplary in Figure 4.7 b). A Kerr image of a simple domain structure in a Permalloy element is shown, with seven domains providing four different magnetisation directions. The gray value in the image corresponds to a certain magnetisation of the magnetic domain. The setting of the desired microscopy apertures defines the sensitive direction. Thus, the magnetic domains are classified according to their direction of magnetisation in different gray levels by varying the analyser. This can be either observed directly by eye or unceremoniously images can be recorded with a digital CCD camera. Kerr-microscopes provide a spatial resolution of down to $1\,\mu m$, or even slightly below, and due to their fast acquisition times (μs) Kerr-microscopes can realise even time resolved growth and motion of domains[5] [132].

Figure 4.8 a) shows the DFI of a GO-steel lamination[6], where the yellow box indicates the position of the following Kerr investigations. An overview Kerr image of the yellow area is shown in Figure 4.8 b), and reveals large basic domains on the lower left side and an
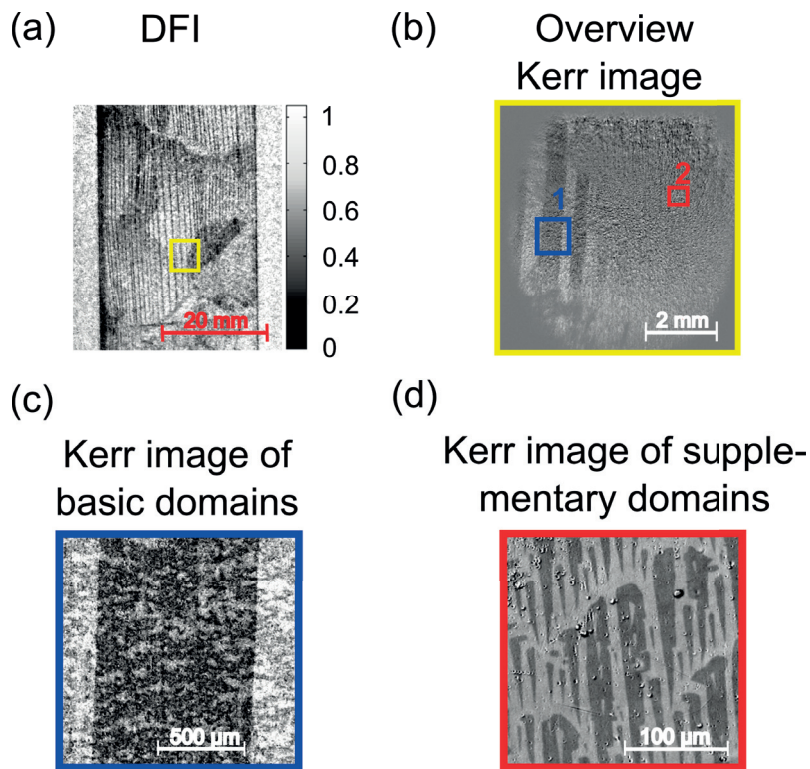
Figure 4.8: a) DFI of a GO-steel sheet, showing where the Kerr images were recorded. b) Overview Kerr image of the yellow-marked area in a). Images c) and d) are magnified Kerr images of the blue and red areas marked in b), respectively. In c) the large basic domains are visible, while in d) the triangular shaped supplementary domains can be seen.

---

[5]Since the polarisation rotations are generally very small, the magnetic contrast is very small. This restriction is usually circumvented by means of digital difference image technique. Further information about Kerr microscopy technique can be found in [41] or [70].

[6]Note, that for the correlative investigations a different lamination has been used than previously, due to the destructive nature of the sample preparation for Kerr microscopy and Laue diffraction.

unresolvable area on the upper right side. Higher magnified images of areas 1 and 2 are shown in Figure 4.8 c) and d), respectively. Figure 4.8 c) reveals millimeter-wide basic domains[7]. The Kerr image of the supplementary domain structure in Figure 4.8 d) shows triangular shaped lancet domains with a width, on average, of well below 50 micrometers as schematically illustrated in Figure 2.3 and explained in [133]. For the performed neutron experiments, these domains are below the detector resolution and cannot be resolved individually, leading to a reduced average DFI signal as observed in Figure 4.8 a). The presence of and explanation for the supplementary domains can be given by a misorientation of the grain. This will be investigated in more detail in 4.2.3. The here presented Kerr investigations were performed in collaboration with Prof. R. Schäfer and S. Pofahl at the Leibniz Institute for solid state and material research Dresden.

4.2.2 Faraday imaging

The Faraday-effect [134] is similar to the Kerr effect. The fundamental difference between those two effects is, that the polarisation plane of the light beam is rotated in transmission for the Faraday effect instead of in reflection for the Kerr effect. This is schematically illustrated in Figure 4.9.
Using the CMOS-magview instrument from Matesy [135], a Bismuth-substituted yttrium iron garnet-indicator film is placed on a magnetic surface. Magnetic stray-fields induce a
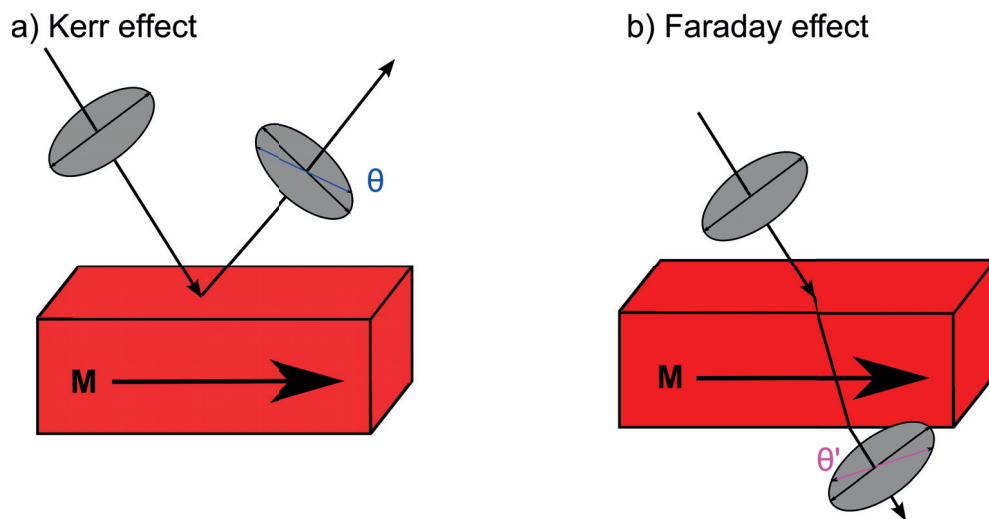
Figure 4.9: Comparison of Kerr and Faraday effect. a) Kerr effect: A linear polarised light beam is reflected at a surface of a material with magnetic field B. The polarisation of the reflected beam is rotated by an angle θ. b) Faraday effect: A linear polarised light beam is transmitted through a material with magnetic field B. The polarisation of the transmitted beam beam is rotated by an angle θ'.

---

[7]Note, that in contrast to the DFI results, which visualise the domain walls, Kerr microscopy depicts the magnetic domain.

Figure 4.10: DFI of the GO-steel lamination on left. Green box indicates the position, where the Faraday image on the right is taken from. In the Faraday image vertical basic domains with a width of hundreds of μm are visible. Additionally triangular shaped supplementary domains are found in the misoriented grain (the grain boundary is schematically draw by a dotted white line). It is clearly visible, that the basic domain structure is superimposed by the supplementary domain structure.

magnetisation in the indicator film. In this indicator film, a projection of the stray fields of the sample is produced. Visible light is able to penetrate the indicator and is reflected back by a mirror behind the layer. Due to the Faraday-effect, the polarisation plane of the visible light is rotated. Afterwards this rotation can be analysed in analogy to the Kerr microscopy investigations [133] [135]. Figure 4.10 shows a DFI of the GO-steel lamination on the left. The 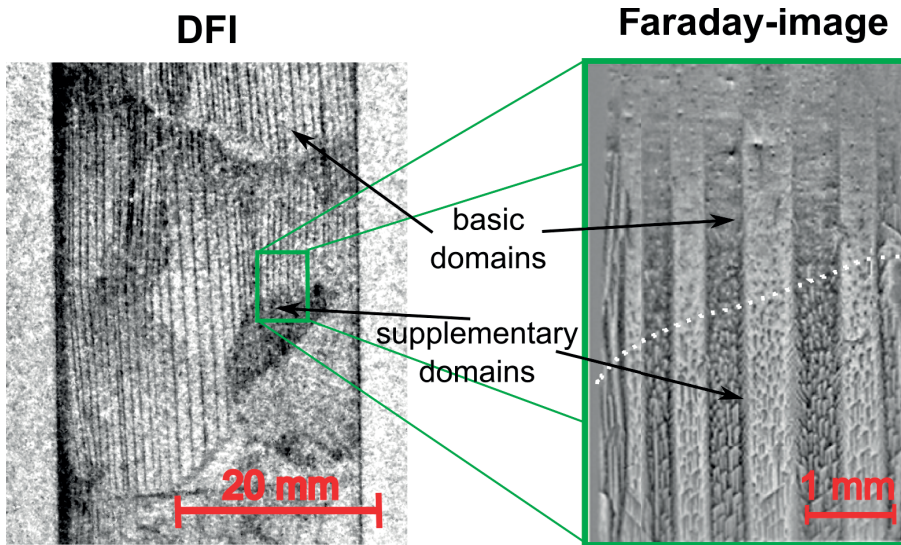green box indicates the position, were the Faraday image, which can be seen on the right, is located. In this Faraday image vertical basic domains with a width of hundreds of μm are visible. Additionally small, triangular shaped supplementary domains are visible in the misoriented grain, as expected from the previous investigations. These supplementary domains are superimposed onto the basic domain structure as was also expected from the DFI investigations.

4.2.3 Small angle neutron scattering (SANS)

Since small-angle neutron scattering (SANS) is the most common neutron technique for the investigation of scattering properties, SANS experiments were carried out, to correlate and verify the DFI findings concerning the interaction of the neutrons with the magnetic domain walls.

SANS techniques use elastic neutron scattering at small angles ($\approx$mrad) to investigate structures with sizes from 1 nm up to several hundreds of nm. The neutrons interact with nuclear and magnetic potential fluctuations [55] as already derived in section 2.4. In Figure 4.11 a
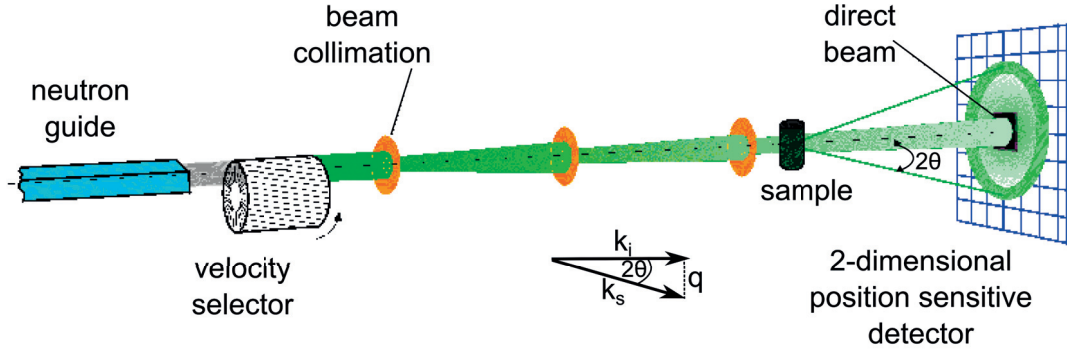
Figure 4.11: SANS instrument as used at PSI [136]. Schematic of a SANS instrument including a velocity selector, several beam collimators a sample and a 2-dimensional position sensitive detection system. The direct neutron beam as well as the scattered beam are shown and the detector records both beams. Thereby the scattering vector $\vec{q}$ or the scattering angle 2θ can be observed.

schematic of a SANS instrument is shown [136]. A collimated beam of neutrons is directed onto a sample. Due to the interaction of the neutrons with the potential fluctuations inside the sample, some neutrons will be deflected by a certain angle. In the detector plane, the direct, undeflected beam with incident wave vector k_i as well as the scattered neutrons with wave vector k_s are recorded by a 2-dimensional, position sensitive detector[8]. The scattering angle 2θ[9] or the scattering vector $\vec{q}$ can be measured. The scattering vector $\vec{q}$ is defined as:

$$\vec{q} = 4\pi \frac{\sin(\theta)}{\lambda}, \tag{4.2}$$

with the wavelength λ and the angle between the incident and scattered beam being 2θ. Easy spoken the scattering vector $\vec{q}$ is difference of incident and scattered wave vector: $\vec{q} = \vec{k}_i - \vec{k}_s$. The sensitivity of such an instrument, that is able to detect scattering angles can consequently be given by the scattering vector $\vec{q}$ or the scattering angle 2θ. These are equivalent descriptions, to be seen from Equation 4.2. In addition the sensitivity can also be characterised using the diameter of the scattering structures d. This is obvious for Bragg scattering looking at the famous Bragg equation: $\lambda = 2d \cdot sin(\theta)$. Here the scattering angle θ is directly linked for a monochromatic beam of neutrons to the scattering centers diameter d.

In Figure 4.12 a) the schematic principle of the angular sensitivity of a SANS instrument is shown, including some setup parameters for the instrument at PSI. The maximum sample to detector distance D_{SD} is 20 m and the pixel size s is 7.5 mm. With these parameters, the smallest angle 2θ that deflects a neutron to the next pixel can be calculated as $\approx 4 \times 10^{-4}$ rad using the intercept theorem. This angle corresponds to a structure size d of 2400 nm and a scattering vector $\vec{q}$ of $3 \cdot 10^{-4}$Å^{-1} at a wavelength of 18 Å. This is somehow the theoretical limitation in words of angular resolution of the instrument with these parameters. The

---

[8]Usually a reference measurement without sample is used for the calibration of the incident wave vector. In the measurement itself, the direct beam is blocked to increase the contrast for the deflected neutrons.

[9]The notation 2θ originates from the Bragg equation

real limit for measurements is given on the instrument web page. The structure sizes d are restricted to sizes smaller than 400 nm [136]. This is equivalent to a scattering angle of $2\theta = 23 \times 10^{-4}$ rad and a scattering vector of $\vec{q} = 1.6 \times 10^{-3}\text{Å}^{-1}$ [10]. The lower limit is given by a structure size of 1 nm [136], which corresponds to $\vec{q} = 0.63\text{Å}^{-1}$ and an angle of $2\theta = 1.12$ rad. These values are tabulated on the right in Figure 4.12 a).

To correlate this sensitivity range with the dark-field investigations, a schematic of the principle of the sensitivity for a nGI is shown in Figure 4.12 b). It could be shown in section 3.3 and [123], that the sensitivity for dark-field imaging at 4.1Å has its maximum for scattering structures with sizes of about 3.6 μm and the sensitivity ranges from 750 nm up to 15 μm. This corresponds to scattering vectors $\vec{q}$ between $8 \cdot 10^{-4}\text{Å}^{-1}$ and $4.2 \cdot 10^{-4}\text{Å}^{-1}$ or scattering angles 2θ between 0.3 mrad and 0.014 mrad. These values for the used wavelength of 4.1 Å can be found in the table on the right in Figure 4.12 b) next to the schematic. Here 2 μm, which is half the period of G_2 and corresponds to the highest sensitivity of the instrument is shown as
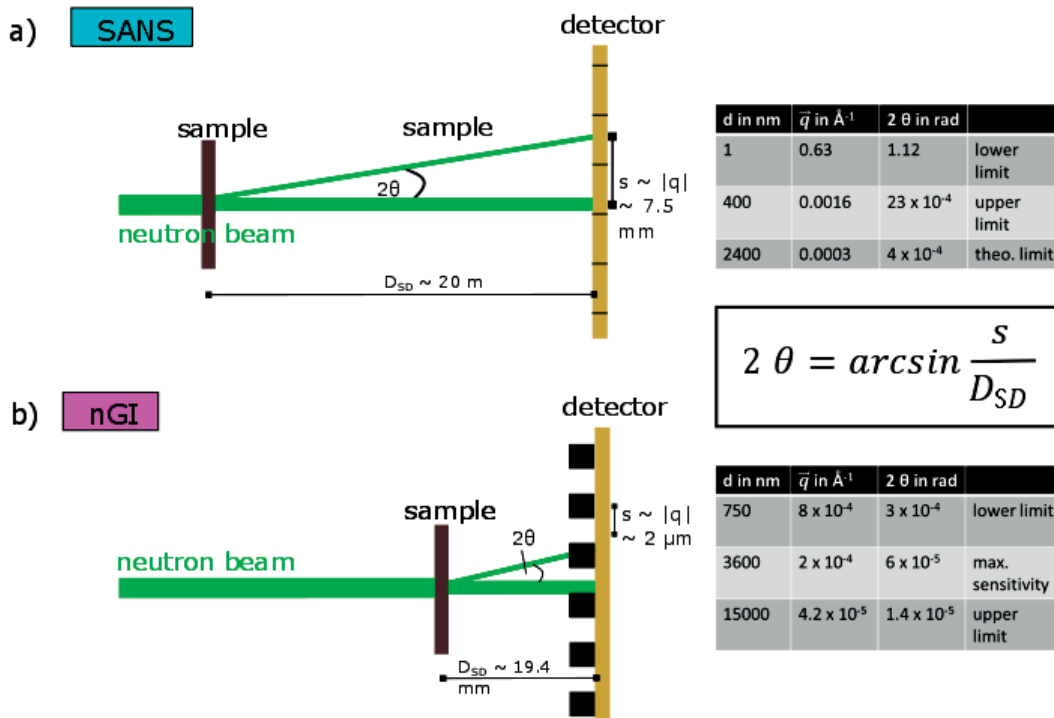
Figure 4.12: Schematic drawing of the SANS and the nGI geometry for sensitivity comparison. For the SANS instrument in a) the theoretically resolvable scattering angle 2θ is ≈ 0.4 mrad, using a sample to detector distance D_{SD} of 20 m and pixel size of 7.5 mm for s. Values for $d, \vec{q}$ and 2θ are shown in the table on the right for a wavelength of 18 Å. In b) a drawing of the geometry of the nGI is shown. From section 3.3 the sensitivity is known to range from 750 nm structures up to 15 μm structures. This corresponds to scattering vectors $\vec{q}$ between $8 \cdot 10^{-4}\text{Å}^{-1}$ and $4.2 \cdot 10^{-4}\text{Å}^{-1}$ or scattering angles 2θ between 0.3 mrad and 0.014 mrad. On the right the values for the lower and upper limit are shown together with the values for the maximum sensitivity for structures of 3.6 μm diameter.

---

[10]This would correspond to a deflection of neutrons for six pixels (45mm) with the mentioned setup parameters.

distance s. From the experimentally detected range of detectable structures the smallest angle 2θ is found to be 0.014 mrad for structures of $d = 15\mu m$, corresponding to a distance s of $\approx$ 200 nm.

Comparing the sensitivity ranges, one can see, that there is hardly an overlap of observable scattering angles in both techniques (nGI: $2\theta \leq 3 \times 10^{-4}$ and SANS: $2\theta \geq 23 \times 10^{-4}$). With the nGI we were able to measure the angular deflection of the neutrons by the magnetic domain walls. But these deflections result in particular but very small scattering angles (tenths of mrad as shown in Figure 2.9) that can not be discretely resolved by the SANS instrument. When the scattering angles become small, so that they cannot be discretely resolved by the SANS instrument, only a slight broadening of the direct neutron beam indicates the occurring of scattering events inside the sample. Therefore the direct beam needs to be analysed unblocked. A slight beam broadening may be observable. As visible from Equation 4.2 on can try to increase the scattering angles by increasing the wavelength, but even for cold neutrons at 18Å, the interaction with magnetic domains still results in a slight broadening of the direct beam.

To observe such a slight beam broadening, SANS experiments were carried out at the SANS-I instrument at SINQ, PSI in collaboration with Dr. J. Kohlbrecher. A pencil neutron beam with a diameter of 1 mm at a wavelength of 18 Å was used to investigate the areas 1 and 2 of the GO-steel lamination. These areas can be seen schematically in the DFI-inset in Figure 4.13. The neutron beam traversing area 2 is slightly broadened, what can be seen in the plot in Figure 4.13. This area (area 2) is in a grain, which contains supplementary domains[11]. The high amount of domain walls (supplementary domain walls) in this area leads to a higher angular deviation of the neutron beam passing this area and consequently to a broadening of the direct neutron beam. This beam broadening can be seen especially in the comparison with the neutron beam penetrating area 1 (with less magnetic domain walls). In the graph in Figure 4.13, the normalised intensity[12] I is plotted versus the scattering vector $\vec{q}$, for both areas. The radial average of the intensity of the beam passing through area 2 (red triangles) is broadened to higher $\vec{q}$-values than the radial average of area 1 (blue squares). This is additionally highlighted by the yellow sphere in the graph. The inherent mechanism for the beam broadening is multiple refraction of the penetrating neutrons at domain walls in the volume of the lamination. The higher amount (density) of domain walls when passing through the volume of area 2, as it was already observed for the surface in Figure 4.8, can be conveyed by this results to the volume of the GO-steel lamination. This is permitted due to the neutrons sensitivity to both, surface and volume domain walls equally during the penetration path through the lamination. This result correlates well with the angular deviations of the neutron beam, detected in the DFIs and verifies the interpretations given in the previous section.

---

[11]Also known from the previous investigation of the chapter.

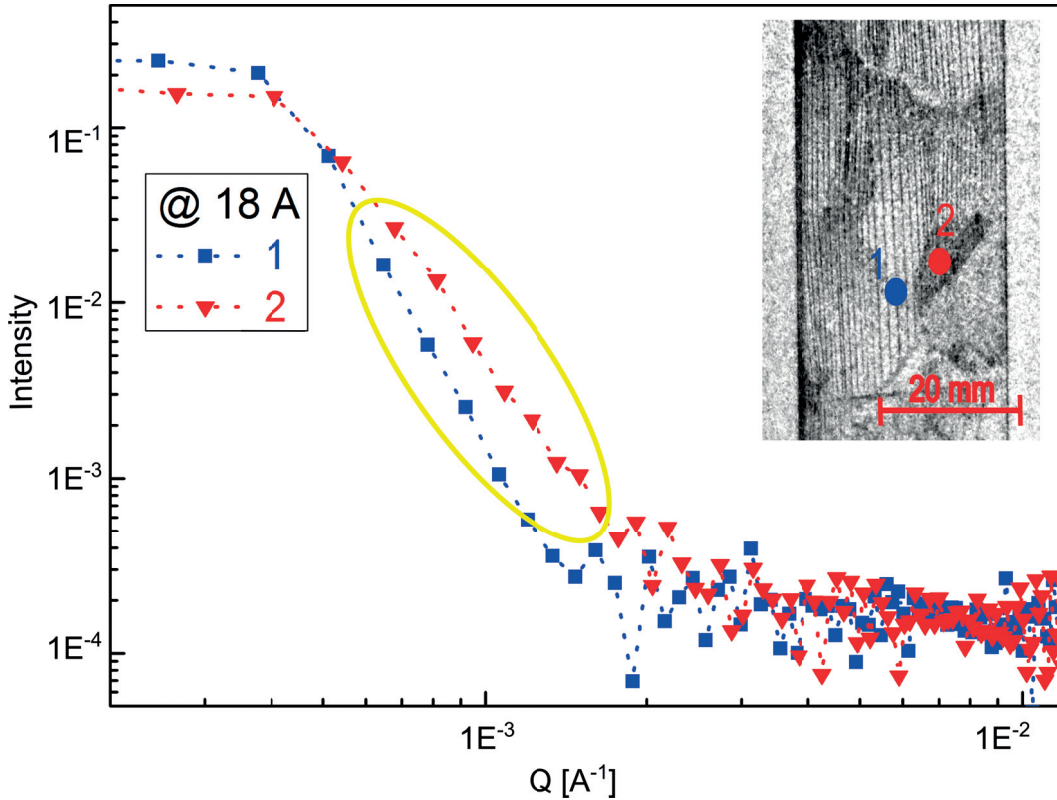[12]Normalised to the intensity of the central beam.

Figure 4.13: The neutron beam, which penetrates area 2 is broadened due to the higher amount of domain walls in the misoriented grain. The comparison of the plots of the radial average of the scattering vector $\vec{q}$ versus the intensity for both beams, penetrating area 1 and 2 respectively, shows the broadening of the beam in area 2 (highlighted by the yellow sphere) compared to the one penetrating area 1 clearly. The inset shows a DFI, where both areas, where the SANS measurements took place, are schematically delineated.

4.2.4 Laue X-ray diffraction

The presence of and explanation for the supplementary domains can be confirmed by crystallographic considerations. If a grain is misaligned with respect to the surface, the magnetic easy axes are misoriented (compare Figure 2.3). This creates energetically unfavorable magnetic stray fields. Though, the stray-field energy can be reduced by the formation of supplementary domains patterns. However, the generation of supplementary domains also costs energy. The reduction in stray-field energy needs to exceed the energy required for the generation of supplementary domains. The stray-field energy increases with an increasing misorientation angle ϑ_s (compare Figure 2.3). As a result, supplementary domains and consequently, a higher number of domain walls, will be generated in misoriented grains [70]. The threshold at which supplementary domains are formed is determined by comparing the sample thickness t to a characteristic length t_0, given by

$$t_0 = \frac{\sqrt{A \cdot K}}{K_d \cdot sin^2(\vartheta_s)}.$$
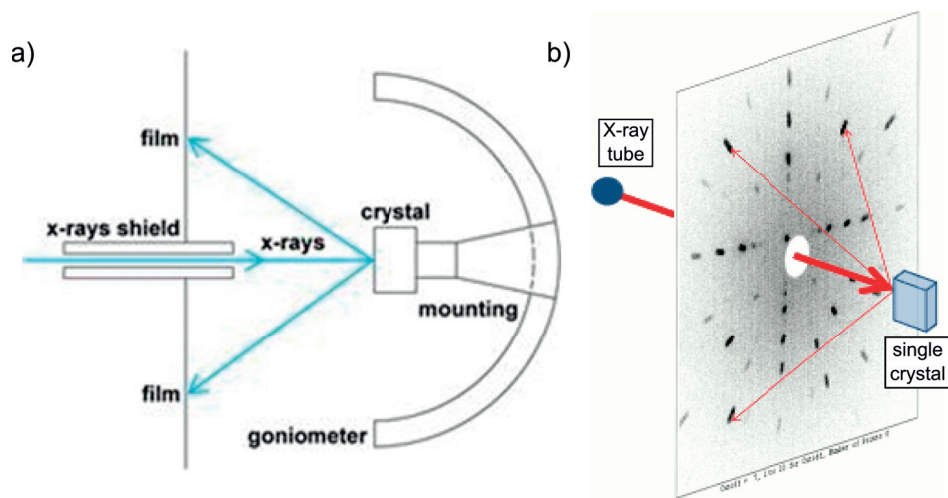
(4.3)

Figure 4.14: Setup and principle of a Laue diffraction experiment. a) Illustration of a setup for a backscattering Laue experiment. The X-ray beam is directed to a crystal sample. The X-rays are back reflected and recorded by a film. The film includes a hole for the penetration of the incident beam and the sample can be aligned by goniometers [137]. b) Schematic of a sample, which reflects back the incident beam to various reflections. These reflections correspond to different lattice planes and wavelength, since Laue diffraction is using a white radiation [138].

In this equation[13], A is the exchange constant, K the anisotropy constant, K_d the stray field constant, and ϑ_s the misorientation angle as introduced in Figure 2.3. If the thickness $t > t_0$, supplementary domains will be present [70]. For the investigated GO-steel lamination having a thickness of t = 300 μm, the misorientation angle ϑ_s needs to exceed 1.1 °. For this calculation, the exchange constant A was $2 \cdot 10^{-11} \frac{J}{m}$, the anisotropy constant K was $3.5 \cdot 10^4 \frac{J}{m^3}$ and the stray field constant was $7.6 \cdot 10^4 \frac{J}{m^3}$ which are exemplary chosen, but realistic values [70]. Note, that supplementary domains are only formed for misorientation angles up to $\vartheta_s \leq 10°$. Larger misorientation angles lead to fractally branched surface domain structures [70].

X-ray Laue diffraction (XRD) can be used to determine the orientation of a single crystal. This means, the determination of the arrangement of the major crystal axes with respect to the coordinates that represent the external form of the crystal. When a single crystal is irradiated with x-rays the lattice planes of the crystal serve as grating (in the sense of Bragg diffraction) and the X-rays will be diffracted intensely towards particular directions [139]. These reflections can be described by the Bragg- or von Laue-equations equivalently. Figure 4.14 a) illustrates the setup of a backscattering Laue experiment. An X-ray beam is directed onto a crystal sample. The X-rays are back reflected and recorded by a film. The film includes a hole for the penetration of the incident beam and the sample can be aligned by goniometers. In Figure 4.14 b) a single crystal is schematically shown, which reflects back the incident beam to the detector, which records various reflections. These reflections correspond to various lattice planes and wavelengths, since Laue diffraction is using a white radiation.

Though, XRD investigations (1 mm beam diameter, 5mA at 20KV acceleration voltage using

---

[13]compare also section 2.1.2 and [70]

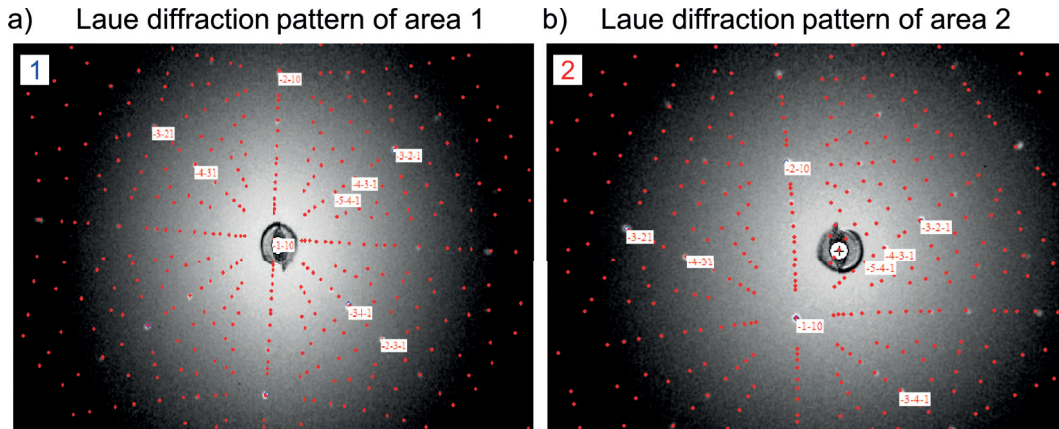a)   Laue diffraction pattern of area 1   b)   Laue diffraction pattern of area 2

Figure 4.15: a) X-Ray Laue diffraction pattern for a nearly perfect oriented grain with $\vartheta_s \approx 0.2°$ (area 1 in Figure 4.13). b) X-Ray Laue diffraction pattern for a slightly misoriented grain (area 2 in Figure 4.13), where $\vartheta_s \approx 8°$.

a tungsten X-ray tube) on the two positions that were already investigated by the previous techniques, were performed under the supervision of Dr. E. Pomjakushina at PSI in the Solid State Chemistry Group, Laboratory for Scientific Developments and Novel Materials (LDM). For each position, an individual Laue pattern, which represents the reciprocal lattice of the crystal, is recorded. The patterns are indexed using the software Orient-express [140], which makes it possible to orient a single crystal of known unit cell dimensions from a single Laue pattern [141]. The needed input parameters were the crystal system (cubic), the cell parameters ($a = b = c = 2.866$Å), sample to detector distance (4.5 cm) and the wavelength range (0.35Å – 2.5Å). The method of the program is based on the indexing of a small set of selected reflections. From this, a small number of possible solutions is proposed. The program computes and displays the corresponding simulated Laue patterns or set of patterns. The correct solution is unambiguously obtained through the visual comparison of simulated and experimentally observed patterns. When the correct solution is found, the program allows for the computation of the orientation matrix of the crystal and thereby the grain (mis-)orientation. The so indexed Laue patterns of both grains of the GO-steel lamination can be found in Figure 4.15. The two positions correspond to the areas 1 and 2 as shown in Figure 4.13.

In Figure 4.15 a) the indexed pattern of area 1 reveals a grain that is nearly perfectly Goss-oriented. From the orientation matrix of the crystal, the misorientation angle ϑ_s turns out to be 0.2 degree for area 1. Therefore no supplementary domains will be generated. In b) the Laue pattern of area 2 is found to provide an angle of approximately $\vartheta_s \approx 8°$ between its easy axis and the samples surface. Here, supplementary domains will be generated, due to the reduction of magnetic stray fields. These two different alignments explain the presence of supplementary domains which are formed to reduce stray-field energies easily in the sense of equation 4.3 in area 2 while non are present in area 1. Though, this result is in accordance to the experimentally observed formation of supplementary domains in the DFI.

4.3 Results & discussion

GO-steel laminations are almost exclusively characterised using global inductive B-H-loop measurements. The underlying physical nature and behaviour of the local domain structure determines the global magnetic properties. However, the bulk magnetic domain arrangement and response cannot be analysed through inductive investigations.

Here the neutron grating interferometry technique, providing the dark-field imaging signal was used to complete a detailed study of the in-situ and locally-resolved visualisation of bulk magnetic domain structures and their response to externally applied static magnetic fields.

The behaviour of the basic and the supplementary domain structure could be distinguished during magnetisation. Even supplementary domains, in superposition with the underlying basic domain structure, could be identified. The domain structure was visualised for the characteristic points in a hysteresis loop, including the initial magnetisation, the saturation magnetisation, the remanent magnetisation, and the recovered demagnetised state.

For the verification of the nGI technique, Kerr microscopy investigations, faraday imaging, SANS experiments and XRD Laue investigations were performed. The interpretations arising from the DFIs are found to be correct and can be applied to further investigations from now on: Large magnetic domains walls are visualised as black lines. Misoriented grains lead to a generation of supplementary domains for energetic reasons of stray field reduction, depending on the angle of misorientation ϑ_s. Basic domains are superimposed by these supplementary domains, and consequently the DFI signal is reduced on average. The link between misorientation angle and DFI signal would enable investigations of the crystallographic texture of a macroscopic sample by only one dark-field image, somewhat a "one-shot" measurement. This would be highly advantageous compared to other commonly used techniques like electron back-scatter diffraction (EBSD) due to the much larger field of view (EBSD $\leq$ mm) and the decreased time needed for the characterisation of an entire lamination [142].

The DFI results presented here have the potential to lead to a further development of the magnetic properties of GO-steel laminations and also to help physicists to better understand macro-magnetic phenomena in bulk ferromagnetic materials. This is due to the possibility of visualising the bulk magnetic domain structure spatially resolved in a centimeter sized field of view under an externally applied magnetic influence [127].

5 Experiments II: *Dynamic* magnetisation process of Goss-oriented electrical steels in magnetic AC - fields

In this chapter, the visualisation and interpretation of the bulk magnetic domain wall response to an external alternating sinusoidal magnetic field is investigated. Parts of this chapter are submitted to [143]. In particular the influence of a DC_{offset}, an oscillation amplitude A_{AC} and a frequency f_{AC} to the bulk magnetic domain structure is studied. By increasing the amplitude A_{AC} while maintaining constant values of DC_{offset} and f_{AC}, a transition from a frozen domain wall structure to a mobile one was recorded. Vice versa, increasing f_{AC} while keeping A_{AC} and DC_{offset} constant led to the reverse transition from a mobile domain wall structure into a frozen one. Additionally the variation of both, A_{AC} and f_{AC} revealed an interplay, that shifts the transition regions.

5.1 Neutron grating interferometry results

In a transformer, an alternating voltage is transferred into a second voltage; therefore, transformer cores are flushed by an *alternating* magnetic flux. The properties of a transformer, such as losses and the degree of efficiency, are mainly determined by the behaviour of the magnetic domain structure inside the core material under the influence of such alternating magnetic excitations. Neutron grating interferometry (nGI) experiments allow to study the response of the bulk magnetic domain wall structure to an alternating sinusoidal magnetic excitation. For this purpose, the modified setup is used in combination with the magnetisation frame. The nGI setup used for the alternating magnetic field measurements is shown schematically in Figure 5.1. The DFIs were recorded again by a conventional scintillator (100 µm thick [6]LiF/ZnS) based detection system using the digital camera [Andor NEO sCMOS, 2160 x 2560 pixels, pixel size: 6.5 µm] placed behind G_2. The intrinsic blurring of the scintillation screen [128] and penumbra blurring caused by the sample to detector distance of $\approx$ 3 cm results in an effective spatial resolution of $\approx$ 70 µm.

The sample, a grade C 130-30 GO-steel lamination, is inserted in the magnetisation frame which is mounted directly in front of the phase grating. The field of view is 35 mm x 35 mm
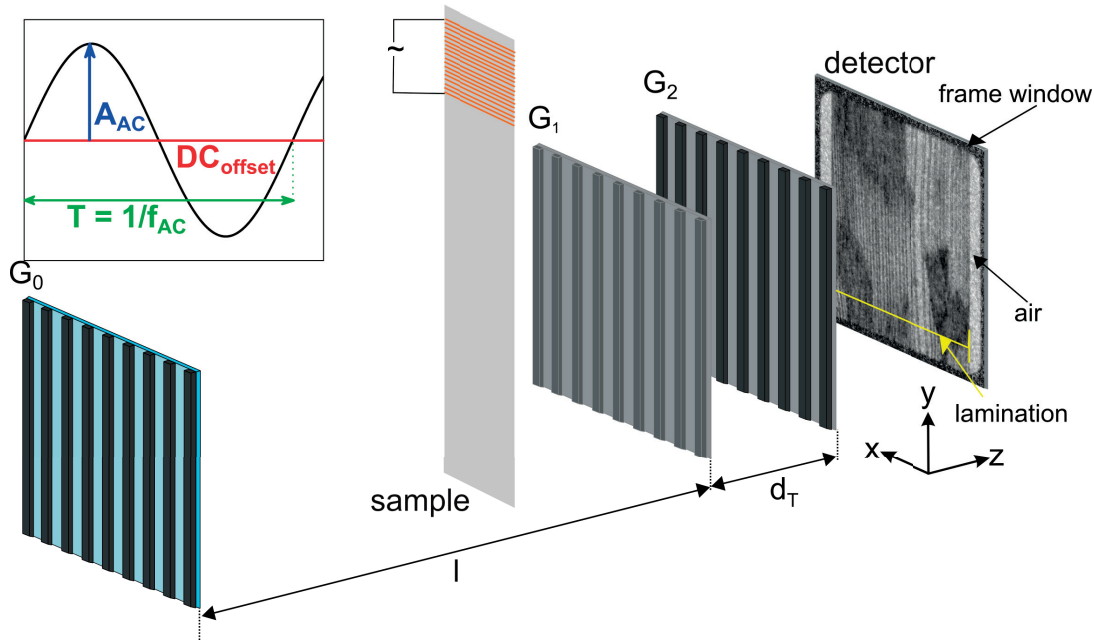
Figure 5.1: Schematic of the neutron grating interferometer for the investigation of the bulk magnetic domain structure under the influence of externally applied alternating magnetic fields with varying parameters DC_{offset}, A_{AC}, and f_{AC} as explained in the inset. The source grating G_0 is placed at a distance l from the phase grating G_1, which is followed by the analyzer grating G_2 at the Talbot distance d_T. The sample is mounted in the magnetization frame and placed as close as possible in front of G_1. The images are recorded using a scintillator based neutron imaging detection system.

limited by the frame window, as in the previous chapter. The alternating magnetic fields are induced by a coil which is supplied with current from an AC power supply [KEPCO BOP100-4ML]. The application of the alternating field is schematically included by the coil, wounded around the sample. The inset in Figure 5.1 schematically depicts the applied magnetic field parameters. A sinusoidal excitation is used with the following parameters, which could be individually varied: The offset of the oscillation DC_{offset} (red) is a constant current. This offset can be seen, in analogy to the investigations in chapter 4, as a static magnetisation of the GO-steel lamination. The amplitude of the sinusoidal oscillation A_{AC} (blue) and the period T or the frequency f_{AC} (green) of the oscillation are a superimposed alternating magnetic excitation. By way of example, a DFI of the sample is shown on the detector. The air gap and the frame window are also visible and marked. The exposure time of every image during the stepping scan was 90 seconds. With 17 steps per scan, this results in a total exposure time for each single DFI in the range of 30 minutes. Thus, it is not possible to visualise a domain wall in motion in real time under conditions of alternating magnetic fields, and the recorded DFIs correspond to a time-averaged domain wall position.

5.1.1 Data acquisition matrix

The behaviour of the bulk magnetic domain structure under the influence of a dynamic, alternating magnetic field differs from static investigations using DC fields in several ways. The alternating, periodical excitation of domain wall movement induces eddy currents which act opposite to the externally applied field and weakens the driving force [41],[70]. With increasing frequencies the wall velocity needs to also increase, which further enhances the eddy-current damping. Altogether this decreases the domain wall mobility.
Consequently, the magnetic domain response to variation in three parameters to examine the frequency-dependent domain wall mobility was investigated. The parameters varied were DC_{offset}, the oscillation amplitude A_{AC}, and the frequency f_{AC}. The corresponding data acquisition matrix is shown in Figure 5.2. Each sphere corresponds to a single DFI measurement. The first investigation was a scan of the DC_{offset} parameter without any oscillation applied ($A_{AC} = 0$ A/m; $f_{AC} = 0$ Hz). This trajectory is marked by the red spheres in Figure 5.2 and the corresponding results are presented in Figure 5.3. This scan reveals the quasistatic magnetisation behaviour (in analogy to chapter 4).

The DC_{offset} was fixed to 4.5 A/m for the remaining investigations, placing the results in the red plane as schematically depicted in Figure 5.2. To represent the amplitude-dependent magnetisation behaviour, a so-called "isofrequency" scan was performed with a fixed frequency of $f_{AC} = 20$ Hz, while the amplitude A_{AC} was stepwise increased from 15 A/m up to 1500 A/m. This scan is illustrated by the blue spheres in Figure 5.2 and the corresponding DFIs are shown in Figure 5.4. To depict the frequency-dependent magnetisation behaviour, an analogous "isoamplitude" scan was conducted, where the amplitude was fixed at $A_{AC} = 225$ A/m and the frequency f_{AC} was increased from 1 Hz up to 200 Hz. This scan is illustrated by the green spheres in Figure 5.2 and the corresponding DFIs are presented in Figure 5.5. To complete the data acquisition matrix, the remaining data points are covered by consecutively recording isofrequency scans at $f_{AC} = 1/5/10/30/50/100/200$ Hz with the amplitude A_{AC} incrementally increased from 15 A/m up to 1500 A/m as in the isofrequency scan. These data points are shown by the orange spheres in Figure 5.2, while the corresponding DFIs can be found in Figure 5.6.
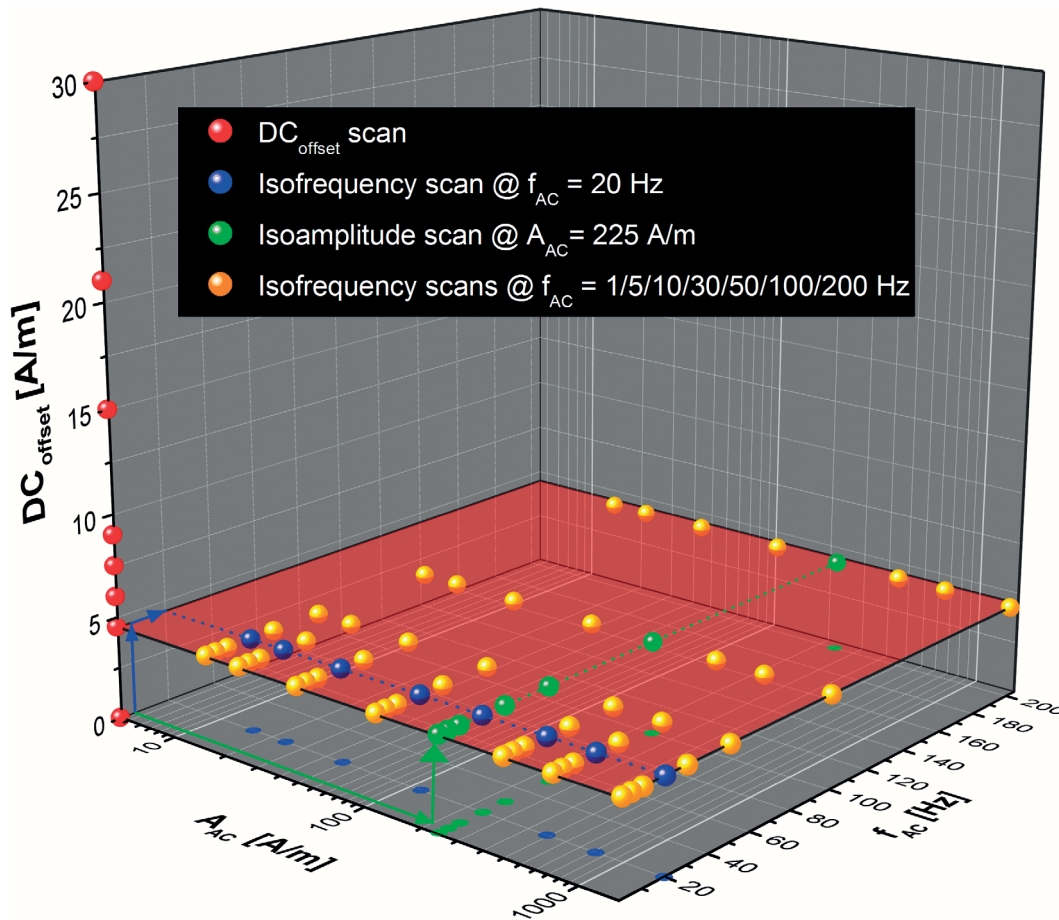
Figure 5.2: Data acquisition matrix for the DC_{offset}, the oscillation amplitude A_{AC}, and frequency f_{AC} of the alternating sinusoidal magnetic field. Each sphere represents a DFI measurement. The red spheres mark the DC_{offset} scan, blue spheres represent the isofrequency scan at a fixed frequency of $f_{AC} = 20$ Hz with increasing oscillation amplitude, green spheres illustrate the isoamplitude scan at a fixed amplitude $A_{AC} = 225$ A/m with increasing frequency, and orange spheres indicate the completing isofrequency scans.

5.1.2 DC_{offset} scan

The DFI results of the DC_{offset} scan (denoted by the red spheres in Figure 5.2) are shown in Figure 5.3. The DFI at 0 A/m, without magnetic field applied, shows a pronounced contrast with dedicated features.

Here the sample is again mounted in such a way that the crystallographic [001]-direction is aligned parallel to the grating lines. Accordingly, the magnetisation of the 180° basic domain points in a vertical direction of the image [70]. The magnetic field is applied in this direction for subsequent investigations. In addition to the basic domain structure, centimeter-sized areas with a decreased DFI value can be observed. These areas indicate grains with a crystallographic misorientation (i.e. out-of-plane misalignment of the almost surface-parallel [001] easy axis by some degrees), leading to the generation of supplementary domains (compare chapter 4) that are smaller than the detector resolution. Consequently, a decreased average DFI signal is

interpreted as a higher relative density of domain walls.

Applying a magnetic field of DC_{offset} = 4.5 A/m leads to the cancellation of several volume domain walls, which is visible in the DFI as an increased domain wall spacing. Magnetic domains with a magnetisation pointing in the direction of the applied magnetic field need to grow at the cost of those pointing in the opposite direction. This is due to the magnetic flux that needs to be transported along the lamination (also compare E_{Ze} in section 2.2; Equation 2.2). The pinning of these basic domain walls and their (possibly) abrupt unsnapping (Barkhausen jumps [129]) during magnetisation, in combination with the exposure time of a single DFI, causes the instantaneous jumps of the domain walls to appear as continuous changes in the domain structure. The contrast of the misoriented grains changes because of simultaneous changes in the underlying basic domain structure, while the contrast originating from the supplementary domains remains constant. Further increasing the DC_{offset} to 6 A/m, 7.5 A/m, 9 A/m, 15 A/m and 21 A/m, consecutively, leads to additional basic domain walls vanishing, while they either end at grain boundaries or penetrate misoriented grains, to ensure flux continuity, seen especially in the DFI at DC_{offset} = 4.5 A/m. If they penetrate the misoriented grains, the basic domains build an underlying structure in addition to the supplementary domains. For an applied field of DC_{offset} 30 A/m only a few basic domain walls can be found, whereas the misoriented grains remain visible due to the supplementary domains being still present at higher fields.
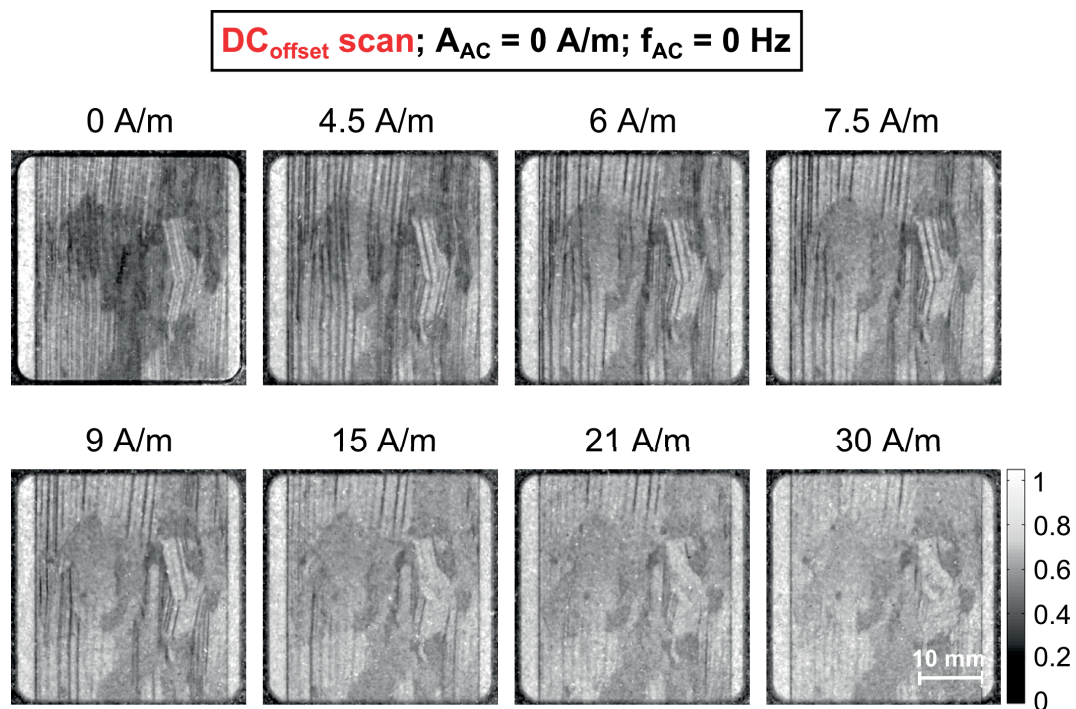
Figure 5.3: Static visualisation of the bulk domain wall structure and response to an applied DC_{offset} (similar to chapter 4). DFIs for increasing field values from DC_{offset} = 0 A/m to 30 A/m are shown (red spheres in Figure 5.2). Large vertically elongated domains are depicted by black lines, representing the domain walls. Misoriented grains appear as dark areas. Increasing fields lead to a cancellation of the basic magnetic domains structure.

These results are similar to those in chapter 4. In the following sections, the investigation of the response of the magnetic domain structures to external alternating, magnetic, sinusoidal excitation that is superimposed on that DC_{offset} value of 4.5 A/m are performed. The frequency- and amplitude-dependent freezing and mobilisation behaviour of bulk magnetic domain structures is studied in detail.

5.1.3 Isofrequency scan

Firstly, the amplitude-dependent behaviour of the bulk domain structure is investigated. A sinusoidal oscillation with a frequency of f_{AC} = 20 Hz in superposition to the DC_{offset} of 4.5 A/m is applied. The results are shown in Figure 5.4. In all DFIs the contrast provided by the walls of the supplementary domains in the misoriented grains remains constant and is independent from A_{AC}. What one can see is a change in the basic domains. In the DFI with an amplitude of A_{AC} = 15 A/m, basic domains are visible as are the supplementary domains , by an average decreased DFI signal, in the misoriented grains. The sharp image of the discrete basic domains indicates that the basic domain walls are stationary[1].

When comparing the DFI with A_{AC} = 15 A/m in Figure 5.4 to the DFI with a DC_{offset} = 15 A/m in Figure 5.3, one sees two different magnetic states. In the DC_{offset} version, most basic domain walls have already vanished. However, in the A_{AC} version many stationary domain walls are, surprisingly, observed. Increasing the amplitude A_{AC} up to 22.5 A/m, 45 A/m, and 112.5 A/m, respectively, does not induce significant changes in the domain wall structure, as can be seen in the corresponding DFIs. The domain structure remains frozen, meaning the domain walls do not move. In the DFI with an amplitude of A_{AC} = 225 A/m, the basic domain walls appear blurred. This is interpreted as a trembling of the domain walls around their initial position. This trembling-based blurring increases with increasing amplitude as seen in the DFI with A_{AC} = 450 A/m, until the domain structure starts to unfreeze. Further increasing the applied amplitude A_{AC} to 750 A/m and 1500 A/m, respectively, the basic domains are completely converted into a gray veil over the whole sample. This veil represents the average position of the domain walls as they moved across the sample during the multitude of alternating field cycles. The basic domain structure is finally entirely mobilised at these amplitudes. Mobilised domain walls structures means, that a magnetic flux can be transported and consequently a transformer would work. Vice versa, frozen domain wall structures do not allow for magnetic flux transport leading to a transformer not working.

The transition from frozen to mobilised basic domain walls is not instantaneous. Small amplitudes maintain stationary domain structures. The domain walls start to tremble under moderate amplitudes with the distance traveled increasing at higher amplitudes. The distance traveled increases until neighboring domain walls intersect. The intersection of domain walls is depicted as a gray veil in the DFIs due to the long exposure time. The steady process of unfreezing leads to a transition region between 225 A/m and 750 A/m instead of a sharp transition point.

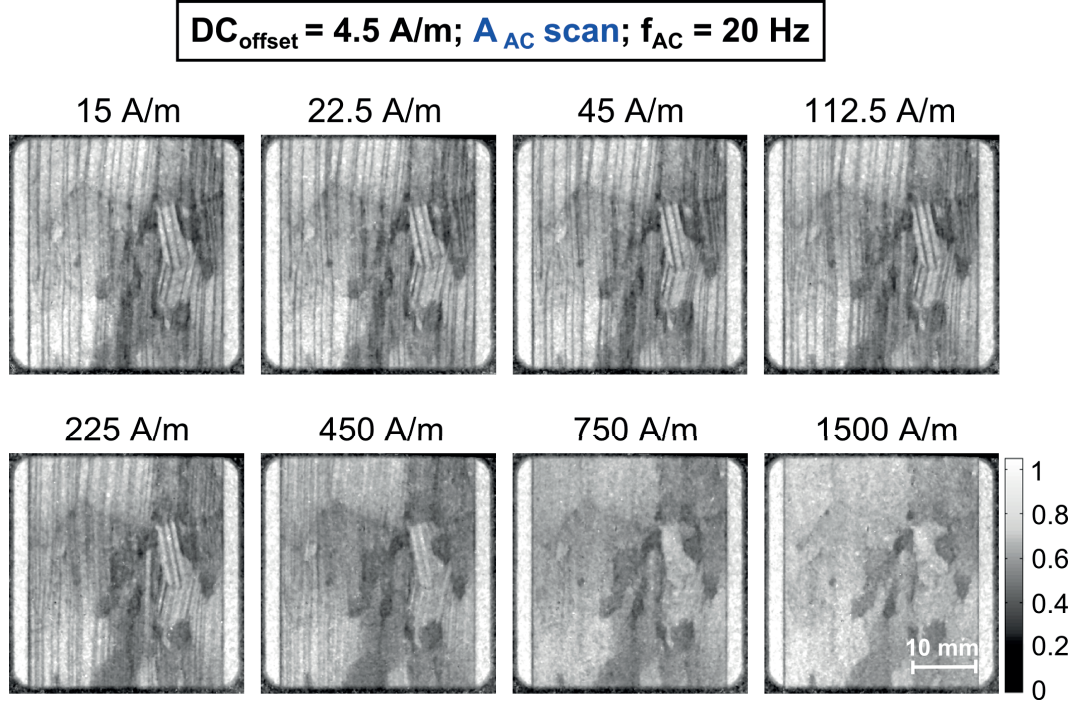[1]At least within one detector pixel.

Figure 5.4: DFIs of the isofrequency-scan (blue spheres in Figure 5.2) at f_{AC} = 20 Hz and DC_{offset} = 4.5 A/m. Stationary domain walls are observed until the amplitude in the transition region (A_{AC} = 450 A/m) starts to excite the domain walls, causing them to tremble. Further increase in amplitude leads to a mobilisation of the basic domain walls, seen as a gray veil that represents the average position of the domain walls during the scan.

The transition from the frozen to mobilised basic domain structure is caused by eddy-current damping phenomena. The eddy-current damping D is proportional to the square of the velocity v of domain walls, v^2, which is proportional to the square of the exciting frequency, f_{AC}^2 [41]:

$$D \propto v^2 \propto f_{AC}^2 \tag{5.1}$$

At a fixed frequency f_{AC}, the amplitude A_{AC} needs to overcome a threshold value to energetically compensate for the frequency-induced eddy-current damping.

Note that the DFI in Figure 5.3 with DC_{offset} = 30 A/m and the DFI in Figure 5.4 with an A_{AC} of 1500 A/m look rather similar. However, the origins of the contrast in both images fundamentally differ. The contrast in the DC_{offset} DFI represents only one point in the hysteresis curve. In this case, a net magnetic flux can be transported across the sample, due to the domain structure arrangement. Therefore, domain walls are effectively expelled from the sample. In the case of an alternating field, the domain walls are not completely expelled from the sample, but are invisible due to their motion.

5.1.4 Isoamplitude scan

In this section the magnetic domain structure under variable oscillation frequencies f_{AC}, while the amplitude A_{AC} and the DC_{offset} are kept constant, is discussed.

The bulk magnetic domain behaviour is expected to depend not only on the applied amplitude but also on the frequency of the exciting oscillation [41] [144]. It is known from hysteresis loop measurements, that eddy-current damping effects in iron-silicon alloys are especially dependent on the applied frequency. Therefore, the frequency-dependent domain freezing process was studied by conducting a series of measurements using a fixed amplitude of A_{AC} = 225 A/m superimposed on a DC_{offset} = 4.5 A/m, while the frequency was incrementally increased from 1 Hz to 200 Hz. Consequently this is called an "isoamplitude scan". The corresponding DFI results are shown in Figure 5.5.

Interestingly, the DFIs for increasing frequencies f_{AC} reveal an inverted freezing and mobilisation behaviour to that found for increasing amplitudes A_{AC} in Figure 5.4. The isofrequency scan in Figure 5.4 showed the domain wall mobilisation, whereas in the isoamplitude scan in Figure 5.5 the frequency-induced freezing is visualised.

No basic domain walls are visible in Figure 5.5 in the beginning with a frequency of 1 Hz. The applied amplitude in combination with low frequencies of 1 Hz and 5 Hz leads to the basic domain walls being mobilised, resulting in a gray veil as explained before. In the DFI with

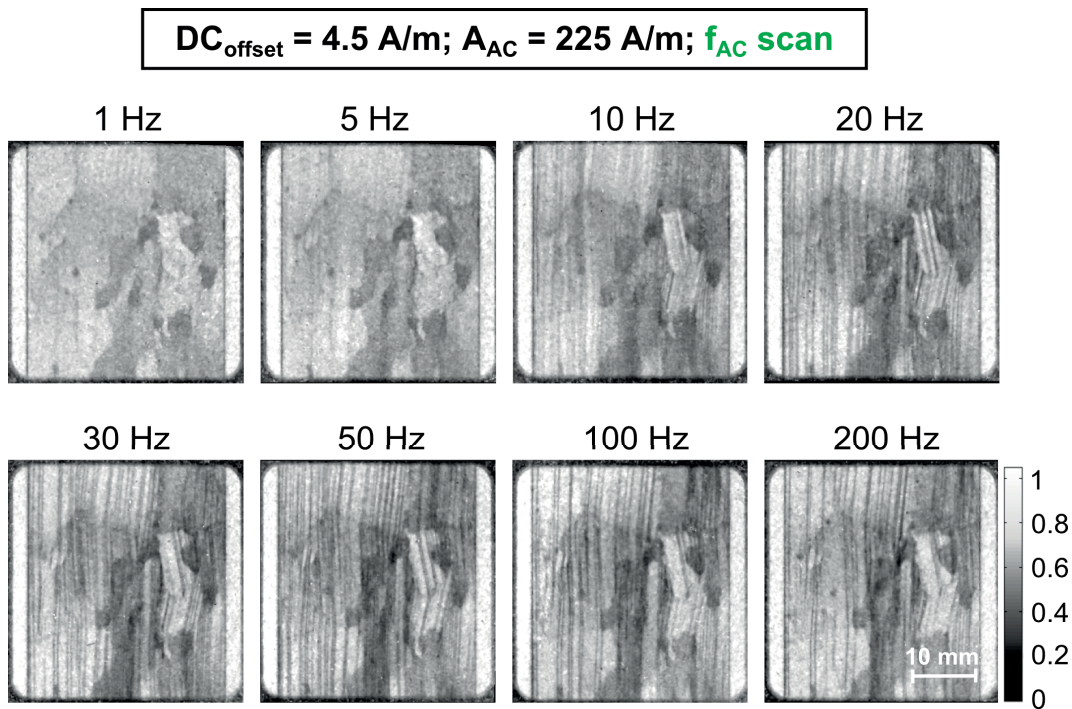**Figure 5.5:** Frequency-induced bulk magnetic domain wall freezing. DFIs of an isoamplitude-scan (green spheres in Figure 5.2) at a DC_{offset} = 4.5 A/m and an A_{AC} = 225 A/m. At low frequencies, domain walls are mobilised. The transition into a frozen domain structure is observed between 5 Hz - 10 Hz. For higher frequencies, the domain walls stay frozen and no significant changes in the DFIs are recorded.

f_{AC} = 10 Hz the basic domain walls start to become visible; the domain walls are visualised as blurred lines as a consequence of their trembling. In the transition region between 5 Hz and 10 Hz, the basic domain wall structure freezes and becomes stationary. Even for higher frequencies such as 20 Hz, 30 Hz, 50 Hz, 100 Hz, and 200 Hz, the basic domain walls remain frozen and no significant changes in the DFIs are recorded.

The transformation into a frozen domain wall structure can likewise be explained by the eddy-current damping phenomena. An increase in frequency f_{AC} according to equation 5.1 leads to an increased domain wall velocity v, which results in larger eddy-current damping. Hence, a magnetic field amplitude of A_{AC} = 225 A/m is large enough to compensate energetically for the eddy-current damping induced by a frequency of 5 Hz and the domain walls are mobile. In contrast, at 10 Hz the excitation amplitude is no longer large enough to compensate for the eddy-current damping, which are proportional to the frequency squared, and the domain walls are frozen. In contrast to the basic domain structure, the supplementary domain structure in the misoriented grains reveals no frequency-dependent behaviour.

The results so far show both an amplitude- and frequency-dependent transition region between frozen and mobilised basic domain wall structures. Therefore, the following section discusses the interplay of these two parameters with respect to the induced freezing phenomena of the basic domain structures.

5.1.5 Shift of the transition regions

To complete the data acquisition matrix, additional isofrequency scans at 1/5/10/30/50/100/200 Hz were performed as indicated by the orange spheres in Figure 5.2. The corresponding DFI results can be found in Figure 5.6. The data of the isofrequency scan from Figure 5.4 are marked by a blue box and the data for the isoamplitude scan shown in Figure 5.5 by a green box, respectively. For small amplitudes A_{AC} and high frequencies f_{AC} (upper left part of the data acquisition matrix), the basic domain walls are found in a frozen state, whereas for high amplitudes and small frequencies the basic domain walls are found in a mobilised state (bottom right part of the data acquisition matrix). Similar to the isofrequency scan at 20 Hz (blue box), no significant changes in the basic domain structure are observed in the isofrequency scans from 1 Hz – 200 Hz until the particular mobilisation (unfreezing) of the domain structure occurs. These transitions are marked by the purple dashed boxes.

The particular transition regions are found to be frequency-dependent. Higher frequencies need higher excitation amplitudes to overcome freezing. Since eddy-current damping increases with increasing frequencies, the amplitude to compensate for these needs to be concordantly increased. At a frequency of 50 Hz and an amplitude of 1500 A/m, it was barely possible to reach the transition region. This is due to the limitations of the sample environment, which does not allow for the application of higher field values[2]. For larger frequencies of 100 Hz and 200 Hz, it was not possible to apply sufficiently large amplitudes to mobilise

---

[2]Higher applied alternating currents would lead to an overheating of the magnetisation frame and consequently destroy the frames windings.

the basic domain walls. Despite these limitations, one can clearly see the trend that larger amplitudes are needed to transform frozen basic domain walls into mobilised domain wall structures at increased frequencies.
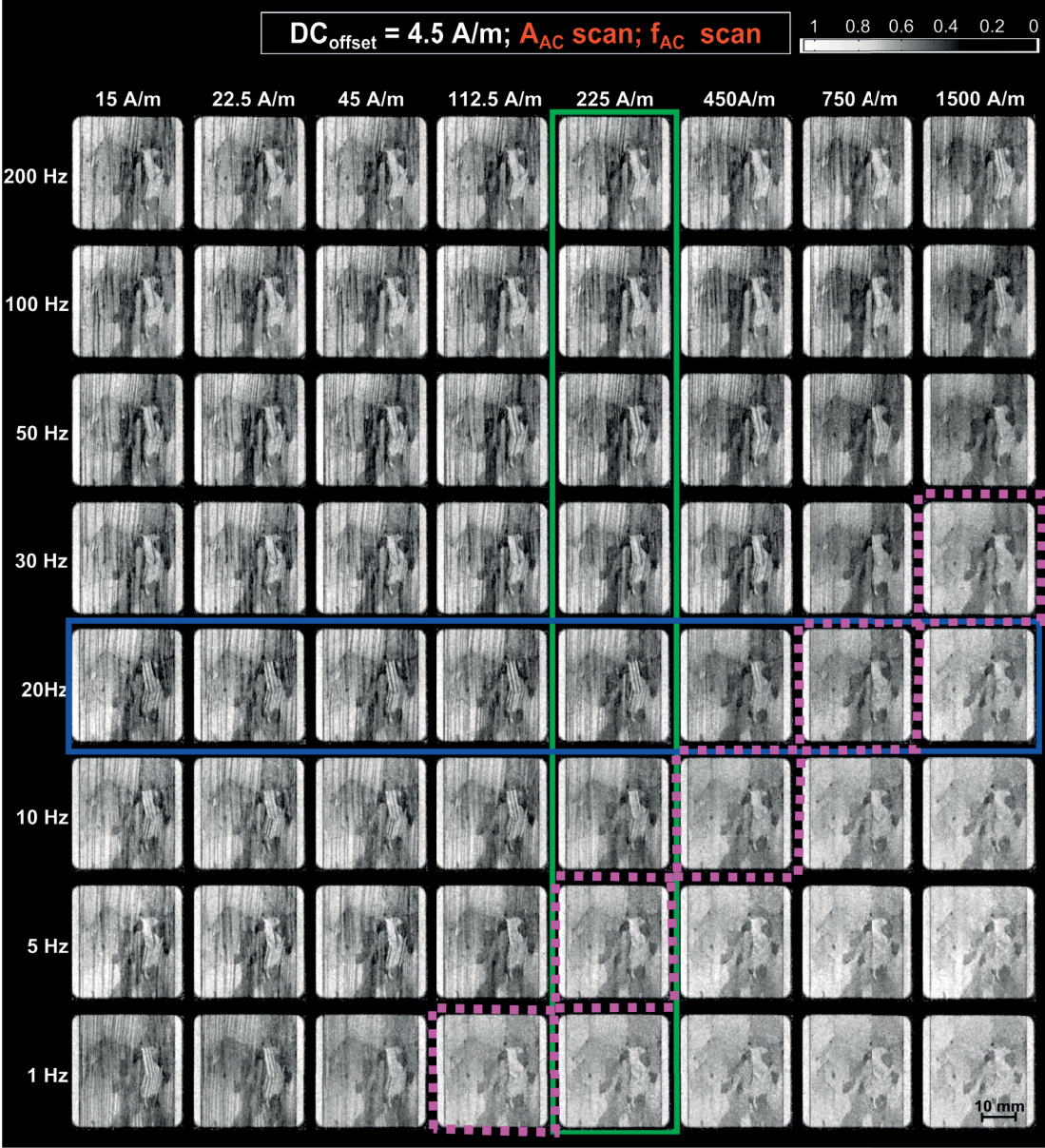

Figure 5.6: Matrix of DFIs, showing the amplitude- and frequency- dependent shift of the transition between frozen and mobilised basic domain wall structures. In the upper left part of the figure with high frequencies and small amplitudes, frozen domain walls are observed. In the bottom right part of the figure with large amplitudes and small frequencies, mobilised domain walls are seen. Representative isofrequency and isoamplitude scans are marked by the blue and green boxes, respectively. The DFIs showing the transition points are marked by purple dashed boxes.

5.2 Results & discussion

In this chapter, the bulk magnetic domain response of an GO-steel lamination under varying frequencies and amplitudes of a sinusoidal magnetic field oscillation given a constant DC_{offset} value was investigated. Transitions of the basic domain structure from a frozen into a mobilised state and vice versa could be identified.

An isoamplitude scan showed that the freezing of the domain structure is induced by increasing the excitation frequency. In contrast, the isofrequency scan revealed, that increasing the excitation amplitude leads to a mobilisation of the domain structure.

Furthermore the identification of a shift of the transition region towards higher amplitudes for increasing frequencies was given. This was done, by studying in detail the interplay between the frequency and amplitude of the magnetic excitation. Thus, the frequency-induced freezing phenomena of bulk magnetic domain walls could be visualised. These results are submitted to [143].

Due to this locally resolved visualisation of the freezing phenomena fundamental insights in to local magnetic domain behaviour could be gained, since B-H-measurements only obtain this effects globally. The experimental findings of this chapter, correspond however well with the global measured effects of frequency dependent losses in iron silicon alloys. The basic understanding of the frequency induced freezing process in GO-steel alloys is of high interest to further develop descriptive models for bulk macro magnetic phenomena. Likewise, the DFI results could lead to improvments in the performance and efficiency of transformers. Future experiments using a time-resolved detector setup will provide a more detailed insight into the dynamic magnetic domain wall behaviour, especially in the transition regions [145] [146].

6 Experiments III: Magnetic domain structures in Goss-oriented electrical steels versus externally applied mechanical tensile stress

In this chapter it is shown, how the neutron dark-field image can be used to analyse the influence of the protective coating to the volume basic and supplementary magnetic domain structure in GO-steel laminations. Parts of this chapter can be found in [147]. To visualise the stress effect of the coating to the bulk domain formation, an uncoated GO-steel lamination was used. Then, an externally applied tensile stress was stepwise increased up to 20 MPa. The domain configuration of the intermediate stress states was visualised and furthermore the reproduction of the original domain structure of the coated state was achieved. Additionally, the explanation of how the applied stresses lead to a refinement of the basic domain structure and the suppression and reoccurrence of supplementary domains is given.

6.1 Neutron grating interferometry results

6.1.1 Influence of the protective coating

To perform investigations of the magnetic domain wall structure response to externally applied mechanical forces the modified setup is used in combination with the stress application environment introduced in chapter 3. A schematic drawing of the setup as it is used can be seen in Figure 6.1. A grade C 130-30 GO-steel lamination is mounted in an uni-axial tensile loading machine which is itself placed as close as possible in front of G_1. The applied force is measured by a load cell [Soemer 614] with an accuracy of 0.5 N. For the recording of the image stacks, the nGI setup is combined with a 100 μm thick [6]LiF/ZnS scintillator screen and the digital camera [Andor NEO sCMOS, 2160 x 2560 pixels, pixel size: 6.5 μm]. The effective spatial resolution is 70 μm. This is a result of the used optical system, intrinsic blurring of the scintillation screen and penumbra blurring, which is caused by the sample to detector distance [128]. The GO-steel lamination is inserted into the stress-stage. The field of view in
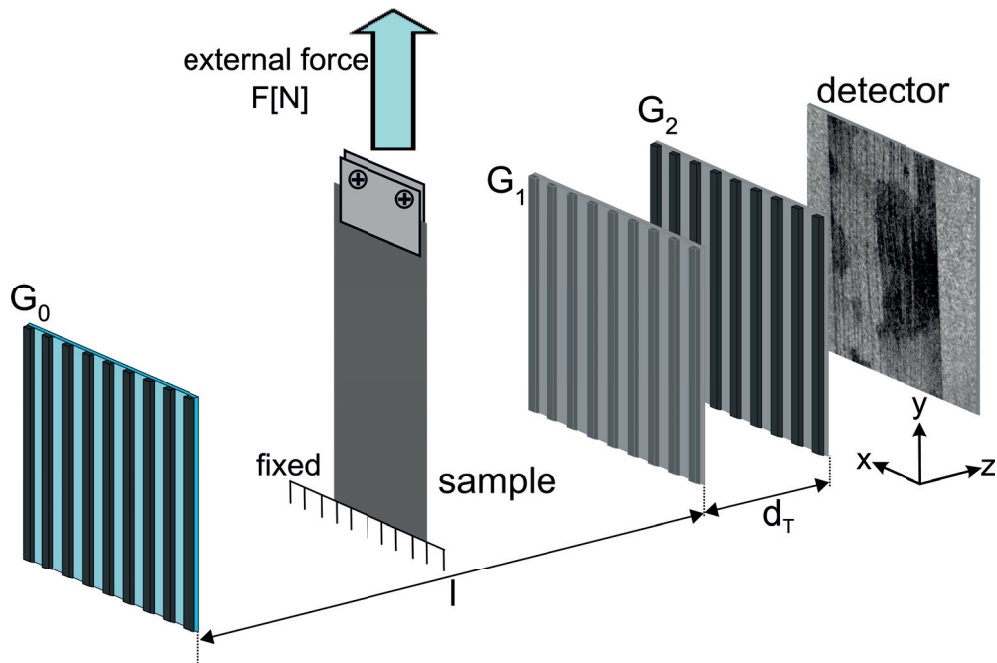
Figure 6.1: Schematic drawing of neutron grating interferometer for the *in-situ* visualisation of the magnetic domain response for externally applied tensile stresses. The source grating, G_0, is placed at distance l in front of the phase grating, G_1. The analyser grating, G_2, is located at the Talbot distance d_T behind G_1. The GO-steel lamination is mounted in a uni-axial tensile loading machine directly in front of G_1. Images are formed by a conventional neutron detection system based on a scintillator screen and a digital camera.

the experiments is 64 x 64 mm, limited by the active grating area. Images shown in this chapter are already cut for clarity and do show smaller areas.

The GO-steel lamination under investigation is clamped in the stage, while it is fixed at the bottom and coupled via springs to the load cell on the top. By moving the translation stage, where the load cell is fixed on, the tensile stress is applied via the springs. The maximum possible force that can be applied is $300N$, while in the measurements only up to $180N$ are applied, for the purpose of staying in the elastic regime.

As previously explained , the coating of GO-steel laminations has articulate effects to the magnetic properties and the magnetic domain structure. Hence, the dark-field imaging technique allows for the comparison of the magnetic domain structure of a coated and an uncoated lamination due to the invisibility of the coating, which is a glassy magnesium silicate layer. For the purpose of comparing the two states, Figure 6.2 shows the transmission images (TIs) of a coated a) and uncoated b) GO-steel lamination where the coating was removed chemically[1] after taking the first images [20]. Here the same lamination is used as for the complementary experiments in section 4.2.

Independent of the presence or the absence of the coating, the TIs in Figure 6.2 a) and b) show a homogeneous, very weak contrast. The corresponding line profiles show an attenuation of

---

[1]No polishing was performed, to avoid additional mechanical influences.

less than 5 %.

In contrast to the TIs, the recorded DFIs, as shown in Figure 6.2 c) and d), reveal a pronounced
contrast with dedicated features for the coated and the uncoated state of the GO-steel lam-
ination, respectively. Black vertical line patterns in both DFIs in Figure 6.2 c) and d) depict
elongated magnetic domains, while the black lines represent the domain walls. The individual
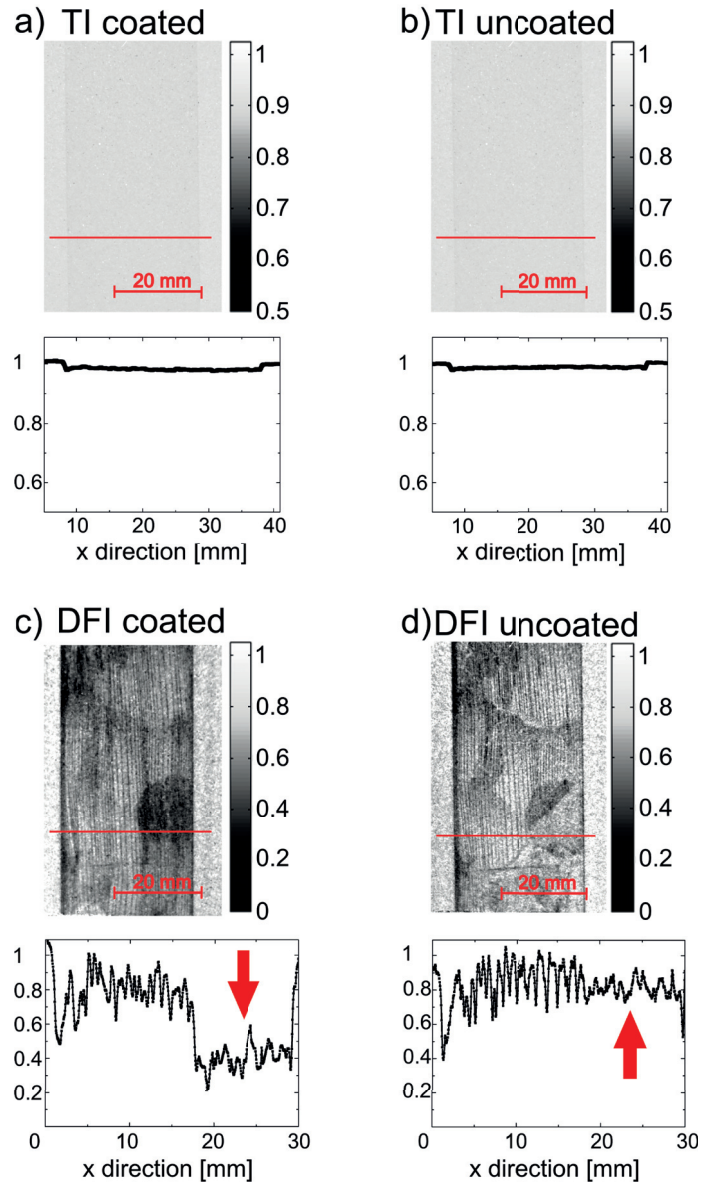domain walls are visible because the width of these volume domains is larger than the detector

Figure 6.2: TI and line profile of a coated a) and uncoated b) GO-steel lamination. Both TI profiles show
a weak, homogeneous attenuation. The profiles in c) and d) correspond to the DFI images
of the coated and uncoated state. Black line patterns represent the walls of elongated
magnetic domains. Areas with reduced DFI signal (red arrow), originating from unresolved
supplementary domain structures, are also visible in the corresponding line profiles.

resolution (compare chapter 4 & 5). Given that the magnetisation of the 180° basic domains points along the crystallographic [001]-direction, the lamination is mounted such that the [001]-direction is aligned parallel to the grating line. In addition, an oval area with a decreased DFI value is observed in the lower part of the coated lamination in Figure 6.2 c). This indicates a grain with a (somewhat) stronger misorientation than the surrounding areas, leading to a high density of supplementary domains (compare section 4.2), that are smaller than the detector resolution. Consequently, a decreased average DFI signal is interpreted as a higher relative density of domain walls.

Comparing the lamination in the uncoated state (Figure 6.2 d)) to the lamination in the coated state, two major effects can be seen. Firstly, a qualitatively similar volume domain structure is observed in the uncoated state, but the width of the basic domains has changed. Secondly, the grain boundaries become more pronounced visible, because some volume domain walls are interrupted at these boundaries. Narrow supplementary domains are formed at the grain boundaries in order to reduce or avoid magnetic poles that would otherwise arise due to a flux misfit across the grain boundary. These grain boundary domains may contain significant transversely magnetised domain volumes [70]. In the DFI images, the presence of these narrow domains leads to a gray veil in (some) grain boundary neighborhoods. In the coated state, a planar tensile stress caused by the glassy coating acts as an effective uni-axial tensile stress in the rolling direction due to the sharp Goss texture. This stress in combination with the inverse magnetostrictive effect favors the [001]-direction in comparison to the transverse magnetic easy axis, and leads to a (certain) suppression of supplementary and grain-boundary domains [41] [70] . Accordingly a removal of the coating implies a removal of tensile stresses. Consequently, the stress removal explains the occurrence of the supplementary domains at the grain boundaries in Figure 6.2 d). The reduction of supplementary domains in the coated state leads to a refinement of the basic domain structure for the reduction of stray fields. This effect is visualised by the widening of the volume domain structure when comparing Figure 6.2 c) and d).

In the oval grain in Figure 6.2 c), the tensile stress of the coating seems to be not strong enough to suppress the supplementary domains due to the stronger misorientation of that grain. After removing the coating (see Figure 6.2 d)), one would even expect a darker DFI signal due to a further increased supplementary domain density. This is not observed. Furthermore, after removing the coating a diagonal line appears in that grain for an unknown reason. For this effect not explanation can be given so far.

It is evident from Figure 6.2 that different magnetic states are analysed when investigation techniques require the removal of the coating to explore the underlying domain structure.

6.1.2   Recovery of the initial domain structure by external mechanical forces

As seen in Figure 6.2, the removal of the coating significantly changes the underlying magnetic domain structure. This was analysed by comparing the domain structures of the initial (uncoated) and final (coated) states. Thus, to analyse the stress dependent magnetic domain

formation in more detail, stepwise an external mechanical force was applied. Starting from the uncoated, stress-free state, the transition via the intermediate stress states up to the reoccurrence of the domain structure of the final coated state was investigated. The experimental results of the stress-dependent domain formation of the uncoated GO-steel lamination are shown in Figure 6.3.

In the here used experimental conditions the externally applied force is completely transferred into stress. Within the resolution of the setup no deformation of the GO-steel lamination is observed and hence the statement of complete stress transfer is justified. In reference [38] it is shown that typical values for stresses, applied by such coatings, are in the range of up to several tenths of MPa. The cross section of the GO-steel lamination is $0.3mm \times 30mm = 9mm^2$. To realise an applied stress of $\sigma = 10$ MPa, a force of $F = 90$ N needs to be applied. The maximum applied stress in the experiments was 20 MPa which corresponds to an applied force of $180N$.
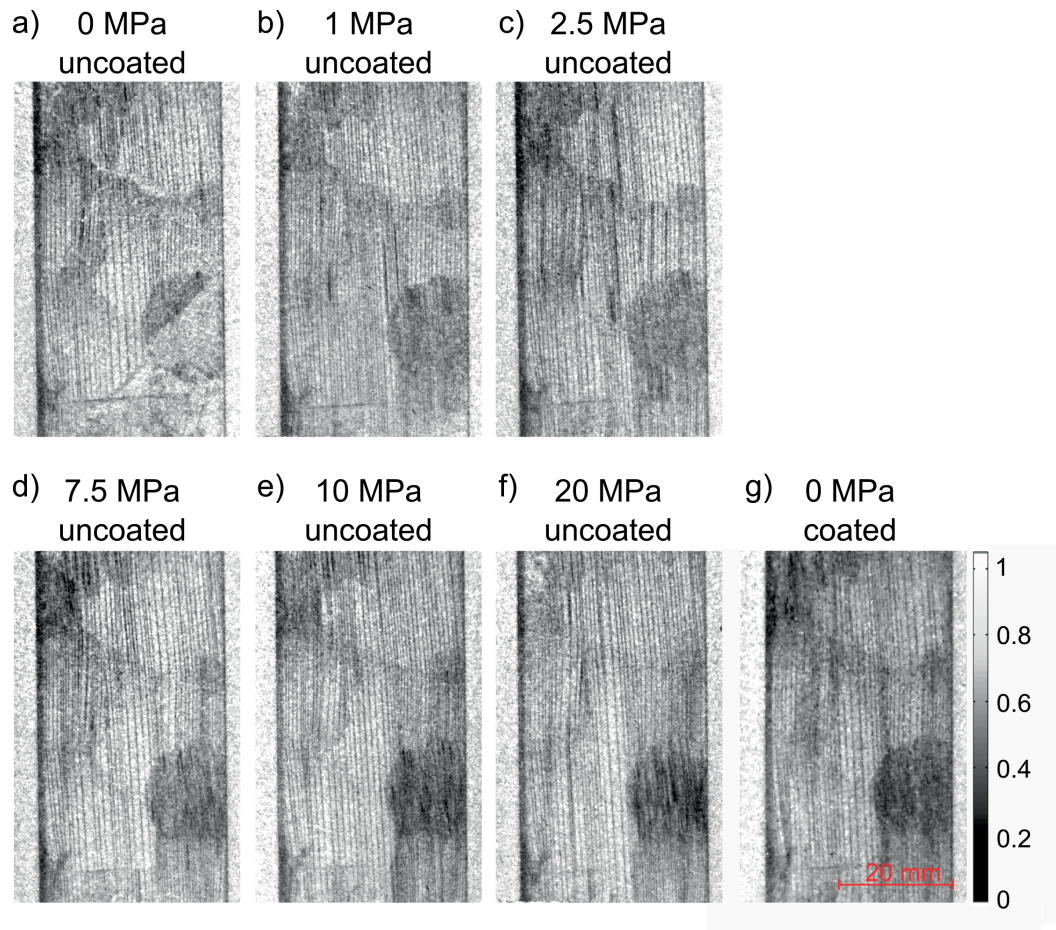

Figure 6.3: DFIs of several intermediate stress states. a) Uncoated GO-steel lamination without externally applied stress. b)-f) Increasing applied stresses up to 20 MPa lead to a refinement of the volume domain structure, the suppression of grain boundary domains at grain boundaries, and a recurrence of the domain structures in the misoriented grain. g) Coated GO-steel lamination without applied stress.

This is far below plasticity of the lamination, since the yield strength of a GO-steel lamination is larger than 300 MPa [39]; hence, the conditions remain within the elastic regime.

In Figure 6.3 a) the DFI of the uncoated GO-steel lamination without applied stress ($\sigma = 0$ MPa) is shown. It serves as both the initial and reference point for the comparison of the domain structure for the following different stress states. Figure 6.3 b) shows the GO-steel lamination with $\sigma = 1$ MPa applied stress. Already applying this small stress leads to a refinement of the basic domain structure. This can be clearly seen on the left side of the misoriented grain. Increasing the stress to $\sigma = 2.5$ MPa, $\sigma = 7.5$ MPa, $\sigma = 10$ MPa, and $\sigma = 20$ MPa (Figure 6.3 c)-f)), respectively, leads to further mutations of the volume and the supplementary domain structure. The changes in the basic domain structure do not manifest in a further refinement. Changes are clearly visible, but the average domain wall spacing does not show a trend and is roughly constant. It can be stated that the refinement process of the basic, volume domain structure is predominantly taking place when small stresses are applied. This can be seen as well in comparison to the coated state in Figure 6.3 g).

It is also observable that, as the applied stress increases, the visibility of the grain boundaries is reduced by the grain boundary domain density being decreased. The grain boundaries are nearly invisible in the DFI with a stress of $\sigma = 20$ MPa shown in Figure 5.4 f), which is similar to that observed in the coated state in Figure 6.3 g).

Most notably, the supplementary domain structure, together with the underlying volume domain structure in the misoriented grain, reappears immediately at an applied stress of only $\sigma = 1$ MPa as shown in Figure 6.3 b).

The application of increasing stresses leads to a more pronounced contrast originating from the misoriented grain in the corresponding DFI. The analysis of this effect is illustrated for better clarity in Figure 6.4. The average dark-field values in the misoriented grain (green circle in the inset) are plotted versus the applied tensile stresses. The red line in Figure 6.4 represents the final DFI value of the coated GO-steel lamination. The grain in the uncoated state of the lamination in the stress-free state provides a DFI value of 0.74. This value decreases as applied stress gradually increases. The reproduction of the original DFI value, observed for the coated GO-steel lamination, is achieved when a stress of σ between 15 MPa and 20 MPa is applied. Because the average DFI signal is a measure of the relative domain wall density, the magnetic domain structure in the coated state can be reproduced to a similar degree in the misoriented grain.

Interestingly, the supplementary domain structure in this misoriented grain is reproduced at significantly higher stresses than those required for the refinement of the volume domain structure.
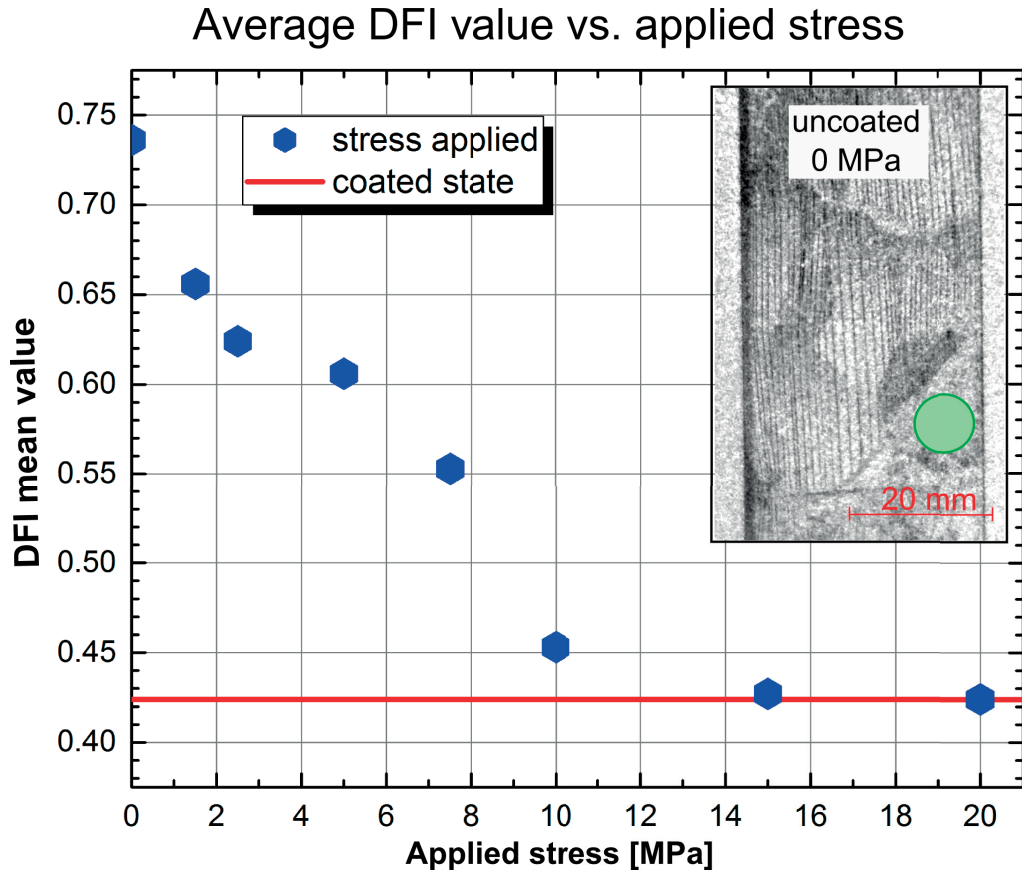
Figure 6.4: Stress-dependent supplementary domain formation in the misoriented grain (area marked by the green circle in the inset). The DFI value for the coated state (red line) is reproduced at stresses between $\sigma = 15 MPa$ and $\sigma = 20 MPa$.

6.2 Results & Discussion

The significant and fundamental influence of the protective coating to the bulk magnetic domain structures was clearly observed by the comparison of a GO-steel lamination once in its coated and once in its uncoated state. These locally resolved findings of the volume behaviour could be explained by the stress relief, resulting from the chemical coating removal and are partly published in [147]. The advantage of the unique possibility delivered by the neutron grating interferometer, to study the underlying magnetic domain structure without removing the protective coating was clearly proven. It was furthermore shown that the removal of the coating influences both, the underlying volume basic and supplementary domain structures.

In this chapter furthermore the stress-dependent recovery of the domain structures under applied external forces was analysed. Both, basic volume and supplementary structures could be reproduced. Basic volume domains were reproduced at small stresses, whereas the supplementary domain structure in a misoriented grain was entirely recovered at significantly higher values of applied stress.

The DFI findings presented here have the potential to further improve the properties and the understanding of magnetic phenomena in GO-steels, although the effects in the misoriented grain could not be explained and were unexpected. For the understanding of these phenomena additional studies are needed. Especially the expansion to more samples is needed to increase the statistics of this observation. The crystallographic investigation of such misoriented grains as well as the validation using alternative experimental approaches can help to understand and explain this phenomena.

7 Conclusion & Outlook

Neutron grating interferometry allows for the visualisation of bulk magnetic domain structures in Goss-oriented high-permeability electrical steel laminations.

In this thesis, the neutron dark-field image (DFI) is used to investigate the local response of both, basic and supplementary domains to various external influences. These external influence are: (i) externally applied *static* DC-magnetic fields, (ii) externally applied alternating, *dynamic* AC-magnetic fields and (iii) externally applied mechanical forces, that apply tensile *stresses* to the sample.
The basic domain structures as well as the superimposed supplementary domain structures could be distinguished and visualised independently. The basic domains are visualised individually due to their domain wall spacing that is larger than the detector resolution of ≈ 70 μm. If the domains are smaller than the detector resolution, like the supplementary domains, the DFI signal can be interpreted as a projection of a relative domain wall density distribution in the sample.

The influence of *static* DC-magnetic fields to the behaviour of the bulk magnetic domain structures was investigated. In detail, the basic and supplementary domain structures response was *in-situ* visualised by the application of a stepwise increasing external magnetic field. Thereby locally resolved images of characteristical points of a hysteresis loop, such as the initial magnetisation, the saturation magetisation, the remanent magnetisation and the recovered demagnetised state of a weak-magnetic Goss-oriented transformer steel could be taken. These DFI results, have the potential to lead to a further development of the magnetic properties of GO-steel laminations and also to support physicists to better understand macromagnetic phenomena in bulk ferromagnetic materials.

The *dynamic* magnetic domain response was investigated under the influence of externally applied alternating AC-magnetic fields. In particular, the influence of varying frequencies and amplitudes of a sinusoidal magnetic field oscillation, which was superimposed onto a DC offset value, was studied. Here a time averaged domain wall information was recorded in the neutron dark-field image, because the exposure time for a DFI is the range of 30 minutes.

Transitions of the basic domain structure from a frozen into a mobilised stadium and vice versa could be identified. Systematically performed isoamplitude scans up to 200 Hz showed that the freezing of the domain structure can be induced by increasing the excitation frequency. In contrast, the isofrequency scans revealed, that increasing the excitation amplitude leads to a mobilisation of the domain structure. The detailed study of the interplay between the frequency and the amplitude of the magnetic excitation allowed for the identification of a shift of the transition regions towards higher amplitudes for increasing frequencies. Hence frequency induced freezing phenomena of bulk magnetic domain walls in GO-steels could be shown and were explained by eddy-current damping effects. The here presented experimental findings are able to support existing theoretical descriptions of the bulk magnetic domain behaviour. Due to the lack of alternative techniques that are able to directly investigate bulk magnetic domain structures, the here presented results are novel.

Furthermore, tensile *stresses* as applied to GO-steels by their common protective coatings were studied. These stresses have a significant impact to the global magnetic performance of transformers as they are determined by the underlying magnetic domain structure in each lamination. The advantage of the possibility delivered by the nGI, to study the domain structures without removing the coating was demonstrated. This allowed for the investigation of the impact of the coating removal from the GO-steel lamination, and the subsequent elimination of stress, to the changes in the underlying domain structures. These changes were especially illustrated by the comparison of the same lamination in its coated and uncoated state. Afterwards, the stress-dependent recovery of the domain structures under the application of external forces was analysed. Both, basic and supplementary structures could be reproduced. Basic domains were found to be reproduced at small stresses, whereas the supplementary domain structures in misoriented grains were recovered at significantly higher values of applied stress. The coating removal also induced a heterogeneous reduction in dark-field contrast in a misoriented grain, which was a very unexpected behaviour. The reason for its occurrence remains unclear, does not fit into existing magnetic models and needs to be further studied. Nevertheless the DFI findings have the potential to further improve the properties of GO-steels used in industrial transformer applications but allow also to enable new approaches in the field of descriptive models for bulk macro-magnetic phenomena.

The DFI findings and their interpretations were verified by correlative measurements. Those were namely Kerr microscopy investigations, Faraday imaging, small angle neutron scattering experiments and X-ray Laue diffraction investigations. Furthermore, a correlation of the grain orientation with the domain wall density and thereby with the obtained DFI signal was found.

The experimentally gained results lead to several new ideas of further investigations and studies. Firstly experiments using a time-resolved detector setup will provide a more detailed insight into the dynamic magnetic domain wall behaviour under the influence of alternating magnetic excitations. Hereby the use of the multichannel plate detector setup with a time resolved imaging approach, which is able to follow the dynamic motion of domain walls, enables especially for the more detailed investigation of the transformation mechanism from

frozen to mobilised magnetic domain structures. Secondly the exact quantitative correlation of the misorientation angle of grains in GO-steel lamination with the DFI signal would allow for the investigation of the crystallographic texture of a macroscopic sample by only one dark-field image, somewhat a "one-shot" measurement. This would be highly advantageous compared to other commonly used techniques like electron backscatter diffraction (EBSD) due to the much larger field of view (EBSD ≤ mm) and the decreased time needed for the characterisation of an entire lamination.

Glossary

A$_{AC}$ amplitude of a alternating magnetic field

CCD charge-coupled device types

DC$_{offset}$ offset of a alternating magnetic field

DFI dark-field image

DPCI differential phase contrast image

EBSD electron backscattering diffraction

f$_{AC}$ frequency of a alternating magnetic field

FeSi Iron-silicon

GO Goss-oriented

GRO Grain-oriented

ICON beam line at PSI; Imaging with COld Neutrons

LiF/ZnS Lithium flouride / Zink sulfuite - mixture

MOKE Magneto optical Kerr effect

nGI neutron Grating Interferometer

NOR Non-oriented

PIN controll software of the beam line; Program for Icon and Neutra or Program for Imaging with Neutrons

PSI Paul Scherrer Institut

SANS small angle neutron scattering

sCMOS scientific complementary metal-oxide-semiconductor

SEM scanning electron microscopy

SINQ Spallation neutron source

TI transmission image

VA volt-amperes

XRD x-ray diffraction

Index

Index

Bibliography

[1] www.sourcingmetals.com.

[2] worldsteel committee on economics studies Brussels. Steel statistical yearbook 2014. Technical report.

[3] ftp://ftp2.stahl-online.de/siz/pdf-publikationen/mb401-elektroband-und-blech.pdf.

[4] Challenges in optimizing the magnetic properties of bulk soft magnetic materials. *Journal of Magnetism and Magnetic Materials*, 320(20):2411 – 2422, 2008. Proceedings of the 18th International Symposium on Soft Magnetic Materials.

[5] incarplus.thyssenkrupp.com.

[6] http://www.vde.com. Vde-studie effizienz- und einsparpotentiale elektrischer energie perspektive bis 2025 und handlungsbedarf, 2008.

[7] Engnet: Engineering Dictionary. http://www.engnetglobal.com.

[8] www.electronics.ca. Electronics industry market research and knowledge network: Global electricity transformers market is expected to exceed 36.7 billion by 2015, Dezember 2008.

[9] http://www.mgmelectricalsurplus.com/Details/Transformers/Substation/265.php.

[10] www.aliexpress.com. 5 watt mini amp transformator.

[11] wikimedia.org. Transformator-primaer-sekundaersida.svg.

[12] A. Mayer and F. Bölling. Some physical and matallurgical fundamentals of the electrical sheet production. *Journal of Magnetism and Magnetic materials*, 2:151–161, 1976.

[13] Dipl.-Ing. N. Brachthäuser. Elektromobilität. Vortrag.

[14] J.S. Marsh E. S. Greiner and B. Stoughton. *The Alloys of Iron and Silicon.* [Alloys of Iron Research. Monograph Series.]. 1933.

[15] https://www.thyssenkrupp.com/de/.

[16] http://nlmk.com/docs/tree/transformer-steel07be2f096fb34b7e3208631f.pdf. www.nlmk.com.

[17] US Patent- No. 1965559 -July 3, 1934.

Bibliography

[18] S M Na and A B Flatau. Surface-energy-induced selective growth of (001) grains in magnetostrictive ternary fe–ga-based alloys. *Smart Materials and Structures*, 21(5):055024, 2012.

[19] http://www.tkes.com. Thyssenkrupp electrical steel produktkatalog.

[20] The sample was etched by the use of hydrochlorid acid diluted with H2O (1:2).

[21] M. Frommert C. Zobrist L. Lahn A. Böttcher D. Raabe S. Zaefferer. Texture measurement of grain-oriented electrical steels aftersecondary recrystallization. *Journal of Magnetism and Magnetic Materials*, 320:657–660, 2008.

[22] M. Soinski. Anisotropy of mechanical properties in cold rolled electrical sheet of goss texture. *Journal of Materials Shaping Technology*, 8:187–191, 1990.

[23] M. Takashima H. Inoue and S. Okabe. Grain oriented electrical steel sheet, 2013.

[24] I. Gutierrez-Urrutia A. Boettcher L. Lahn and D. Raabe. Effects of pulsed magnetic annealing on goss texture development in the primary recrystallization of grain-oriented electrical steel. *J. Magn. Magn. Mater*, 47:4110–4117, 2012.

[25] I. Gutierrez-Urrutia A. Boettcher L. Lahn and D. Raabe. Microstructure - magnetic property relations in grain oriented electrical steels: quantitative analysis of the sharpness of the goss orientation. *Journal of Magnetism and Magnetic Materials*, 49:269–276, 2014.

[26] Raabe Dierk. http://www.dierk-raabe.com/electrical-steels-fe-3-si/.

[27] IEC 60404-2:2008 - 1963.

[28] www.KIT.edu.

[29] https://en.wikipedia.org/wiki/Epstein frame.

[30] wikipedia.org. https://en.wikipedia.org/wiki/electrical-steel.

[31] T. Saito S.Takemoto. Effects of crystal grain size and particle size on core loss for fe - si compressed cores. *Materials Science Forum*, 534-536:1313–1316, 2007.

[32] J. Schneider L. Michalowsky. *Magnettechnik*, volume 3. Vulkan Verlag, 2006.

[33] R. Hilzinger and W. Rodeald. *Magnetic Materials Fundamentals, prproduct,properties, appliapplications ISBN: 978-3-89578-352-4*. Publicis Erlangen, 2013.

[34] http://www.edaboard.com.

[35] K. Akanuma, H. Koshiishi, and N. Urushiyama. Insulation coating for electrical steel sheet and method of application, January 4 1972. US Patent 3,632,362.

[36] K.G. C. Inorganic insulating coating for electrical steel sheet and strip, June 7 1949. US Patent 2,472,592.

[37] W. Grimm, W. Jillek, and A. Hubert. Messung und auswirkungen der von den isolierschichten auf orientiertes transformatorenblech uebertragenen spannungen. *Journal of Magnetism and Magnetic Materials*, 9(1–3):225 – 228, 1978.

[38] E. Beyer, L. Lahn, C. Schepers, and T. Stucky. The influence of compressive stress applied by hard coatings on the power loss of grain oriented electrical steel sheet. *Journal of Magnetism and Magnetic Materials*, 323(15):1985 – 1991, 2011.

[39] AK Steel. Product data bulletin - grain oriented electrical steels.

[40] www.tkes.com. http://www.tkes.com/web/tkeswebcms.nsf/www/en-isolation-h.html.

[41] C.D. Graham B.D. Cullity. *Introduction to magnetic materials*. Wiley, 2009.

[42] T. Yamamoto and T. Nozawa. Effects of tensile stress on total loss of single crystals of 3silicon/iron. *Journal of applied Physics*, 41:2981, 1970.

[43] R. Schaefer and S. Schinnerling. Bulk domain analysis in fesi-crystals. *Journal of Magnetism and magnetic materials*, 215:140–146, 2000.

[44] F. Bitter. Experiments on the nature of ferromagnetism. *Phys. Rev*, 41:507–515, 1932.

[45] J.N. Chapman and M.R. Scheinfein. Transmission electron microscopies of magnetic microstructures. *Journal of magnetism and magnetic materials*, 200(1):729–740, 1999.

[46] A. Tonomura, T. Matsuda, J. Endo, T. Arii, and K. Mihama. Direct observation of fine structure of magnetic domain walls by electron holography. *Physical Review Letters*, 44(21):1430, 1980.

[47] C.M. Schneider. Soft x-ray photoemission electron microscopy as an element-specific probe of magnetic microstructures. *Journal of magnetism and magnetic materials*, 175(1):160–176, 1997.

[48] S. Taguchi and A. Sakakura. Characteristics of magnetic properties of grain-oriented silicon iron with high permeability. *Journal of Applied Physics*, 40(3):1539–1541, 1969.

[49] G.L. Houze Jr. Effect of longitudinal tensile stress on the static and 60 hz domain structures of grain-oriented silicon steel. *Journal of Applied Physics*, 40(3):1090–1091, 1969.

[50] F.E. Werner. Electrical steels: 1970-1990. *Energy Efficient Electrical Steels*, pages 1–32, 1980.

[51] O. Halpern and T. Holstein. On the passage of neutrons through ferromagnets. *Physical Review*, 59(12):960, 1941.

[52] M. Schlenker, W. Bauspiess, W. Graeff, U. Bonse, and H. Rauch. Imaging of ferromagnetic domains by neutron interferometry. *Journal of Magnetism and Magnetic Materials*, 15:1507–1509, 1980.

[53] S. Nakatani, H. Tomimitsu, T. Takahashi, and S. Kikuta. Phase shift of neutrons in magnetic domains observed by interferometry. *Japanese journal of applied physics*, 31(8A):L1137, 1992.

[54] H. Rauch, W. Treimer, and U. Bonse. Test of a single crystal neutron interferometer. *Physics Letters A*, 47(5):369–371, 1974.

Bibliography

[55] H. Rauch and S. A. Werner. *Neutron Interferometry: Lessons in Experimental Quantum Mechanics, Wave-particle Duality, and Entanglement*, volume 12. Oxford University Press, 2015.

[56] M. Schlenker and J. Baruchel. Neutron techniques for the observation of ferro-and antiferromagnetic domains. *Journal of Applied Physics*, 49(3):1996–2001, 1978.

[57] J Baruchel. X-ray and neutron topographical studies of magnetic materials. *Physica B: Condensed Matter*, 192(1):79–93, 1993.

[58] M. Schlenker and C.G. Shull. Polarized neutron techniques for the observation of ferromagnetic domains. *Journal of Applied Physics*, 44(9):4181–4184, 1973.

[59] M. Th. Rekveldt. Study of ferromagnetic bulk domains by neutron depolarization in three dimensions. *Zeitschrift für Physik*, 259(5):391–410, 1973.

[60] F. Pfeiffer, C. Grünzweig, O. Bunk, G. Frei, E. Lehmann, and C. David. Neutron phase imaging and tomography. *Physical review letters*, 96(21):215505, 2006.

[61] C. Grünzweig, C. David, O. Bunk, M. Dierolf, G. Frei, G. Kühne, J. Kohlbrecher, R. Schäfer, P. Lejcek, H.M.R. Rønnow, et al. Neutron decoherence imaging for visualizing bulk magnetic domain structures. *Physical review letters*, 101(2):025504, 2008.

[62] C. Grünzweig, C. David, O. Bunk, M. Dierolf, G. Frei, G. Kühne, R. Schäfer, S. Pofahl, H.M.R. Rønnow, and F. Pfeiffer. Bulk magnetic domain structures visualized by neutron dark-field imaging. *Applied Physics Letters*, 93(11):112504, 2008.

[63] C. Grünzweig, C. David, O. Bunk, J. Kohlbrecher, E. Lehmann, Y.W. Lai, R. Schäfer, S. Roth, P. Lejcek, J. Kopecek, et al. Visualizing the propagation of volume magnetization in bulk ferromagnetic materials by neutron grating interferometry. *Journal of Applied Physics*, 107(9):09D308, 2010.

[64] N. Kardjilov, I. Manke, M. Strobl, A. Hilger, W. Treimer, M. Meissner, T. Krist, and J. Banhart. Three-dimensional imaging of magnetic fields with polarized neutrons. *Nature Physics*, 4(5):399–403, 2008.

[65] http://hoffman.physics.harvard.edu/materials/NdFeB.php.

[66] J. McCord. Progress in magnetic domain observation by advanced magneto-optical microscopy. *Journal of Physics D: Applied Physics*, 48(33):333001, 2015.

[67] J. Kerr. On the magnetisation of light and the illumination of magnetic lines of force. *Rep. Brit. Ass. S*, 5:85, 1876.

[68] J.W. Shilling and G.L. Houze Jr. Magnetic properties and domain structure in grain-oriented 3% si-fe. *Magnetics, IEEE Transactions on*, 10(2):195–223, 1974.

[69] G.L. Houze Jr. Domain-wall motion in grain-oriented silicon steel in cyclic magnetic fields. *Journal of Applied Physics*, 38(3):1089–1096, 1967.

[70] R. Schaefer A. Hubert. *Magnetic Domains*. Springer Verlag, 2000.

[71] Y. Ushigami, M. Mizokami, M. Fujikura, T. Kubota, H. Fujii, and K. Murakami. Recent development of low-loss grain-oriented silicon steel. *Journal of magnetism and magnetic materials*, 254:307–314, 2003.

[72] P.F. Davis. A theory of the shape of spike-like magnetic domains. *Journal of Physics D: Applied Physics*, 2(4):515, 1969.

[73] T. Iuchi, S. Yamaguchi, T. Ichiyama, M. Nakamura, T. Ishimoto, and K. Kuroki. Laser processing for reducing core loss of grain oriented silicon steel. *Journal of Applied Physics*, 53(3):2410–2412, 1982.

[74] R.F. Krause, G.C. Rauch, W.H. Kasner, and R.A. Miller. Effect of laser scribing on the magnetic properties and domain structure of high-permeability 3% si-fe. *Journal of applied physics*, 55(6):2121–2123, 1984.

[75] H. Kronmüller. Theory of nucleation fields in inhomogeneous ferromagnets. *physica status solidi (b)*, 144(1):385–396, 1987.

[76] A. Lazarian. Tracing magnetic fields with aligned grains. *Journal of Quantitative Spectroscopy and Radiative Transfer*, 106(1):225–256, 2007.

[77] C. Kittel. Physical theory of ferromagnetic domains. *Reviews of modern Physics*, 21(4):541, 1949.

[78] H.J. Williams and W. Shockley. A simple domain structure in an iron crystal showing a direct correlation with the magnetization. *Phys. Rev.*, 75:178, 1949.

[79] F. Bitter. On inhomogeneities in the magnetization of ferromagnetic materials. *Physical review*, 38(10):1903, 1931.

[80] P. Zeeman. On the influence of magnetism on the nature of the light emitted by a substance. *The Astrophysical Journal*, 5:332, 1897.

[81] E. Kneller. *Ferromagnetismus*. Springer, Berlin, 1962.

[82] S. Libovicky. Spatial replica of ferromagnetic domains in iron-silicon alloys. *physica status solidi (a)*, 12(2):539–547, 1972.

[83] psi.ch. https://www.psi.ch/niag/neutron-physics.

[84] https://www.ncnr.nist.gov/resources/activation/.

[85] Klett, Eberhard Witwe, Detleffsen, Christoph Peter, et al. *IH Lambert... Photometria sive de mensura et gradibus luminis, colorum et umbrae*. sumptibus viduae Eberhardi Klett, 1760.

[86] Erwin Schrödinger. Quantisierung als eigenwertproblem. *Annalen der physik*, 385(13):437–490, 1926.

[87] James Clerk Maxwell. *A treatise on electricity and magnetism*, volume 1. Clarendon press, 1881.

Bibliography

[88] Louis De Broglie. The reinterpretation of wave mechanics. *Foundations of Physics*, 1(1):5–15, 1970.

[89] Varley F Sears. *Neutron optics: an introduction to the theory of neutron optical phenomena and their applications*, volume 3. Oxford University Press, USA, 1989.

[90] Enrico Fermi. *Collected Papers: Italy 1921-1938*, volume 1. University of Chicago Press, 1971.

[91] Frank Laloe Claude Cohen-Tannoudji, Bernard Diu. *Quantum Mechanics*. Wiley, 2006.

[92] John Markus Blatt and Victor Frederick Weisskopf. *Theoretical nuclear physics*. Springer Science & Business Media, 2012.

[93] M.L. Goldberger and F. Seitz. Theory of the refraction and the diffraction of neutrons by crystals. *Physical Review*, 71(5):294, 1947.

[94] W. Just, C.S. Schneider, R. Ciszewski, and C.G. Shull. Refraction of thermal neutrons by shaped magnetic fields. *Physical Review B*, 7(9):4142, 1973.

[95] M. Strobl, W. Treimer, P. Walter, S. Keil, and I. Manke. Magnetic field induced differential neutron phase contrast imaging. *Applied Physics Letters*, 91(25):254104, 2007.

[96] Pieter Zeeman. Vii. doublets and triplets in the spectrum produced by external magnetic forces. *The London, Edinburgh, and Dublin Philosophical Magazine and Journal of Science*, 44(266):55–60, 1897.

[97] S. Chikazumi and C. D. Graham. *Physics of Ferromagnetism 2e*. Number 94. Oxford University Press, 2009.

[98] F. Ekstein H. Sloch. Magnetic interaction between neutrons and electrons . *Physical review*, 76 (9):1328, 1949.

[99] O. Schaerpf. *Verhalten der NeNeutron beim Durchgang durch die Blochwand*. PhD thesis, Habilitationsschrift, University of Braunschweig, 1976.

[100] O. Schärpf. Theory of magnetic neutron small-angle scattering using the dynamical theory of diffraction instead of the born approximation. i. determination of the scattering angle. *Journal of Applied Crystallography*, 11(5):626–630, 1978.

[101] O. Schärpf. Theory of magnetic neutron small-angle scattering using the dynamical theory of diffraction instead of the born approximation. ii. the behaviour of the intensity of neutrons after transition through a helical magnetic structure. *Journal of Applied Crystallography*, 11(5):631–636, 1978.

[102] J. Peters and W. Treimer. Bloch walls in a nickel single crystal. *Physical Review B*, 64(21):214415, 2001.

[103] C. Grünzweig, F. Pfeiffer, O. Bunk, T. Donath, G. Kühne, G. Frei, M. Dierolf, and C. David. Design, fabrication, and characterization of diffraction gratings for neutron phase contrast imaging. *Review of Scientific Instruments*, 79(5):053703, 2008.

[104] I. Heilmann and J. Kjems. Mechanical velocity selector, neutron flux and q-range for the small angle neutron scattering facility at risø. Technical report, 1980.

[105] T. Weitkamp C. David C. Kottler O. Bunk and F. Pfeiffer. Tomography with grating interferometrs at low-brilliant sources. *Proc. SPIE*, 6318, 2006.

[106] H.F. Talbot. Facts relating to optical science. *Phil. Mag.*, 9:401–407, 1836.

[107] A.P. Kaestner, S. Hartmann, G. Kühne, G. Frei, C. Grünzweig, L. Josic, F. Schmid, and E.H. Lehmann. The icon beamline–a facility for cold neutron imaging at sinq. *Nuclear Instruments and Methods in Physics Research Section A: Accelerators, Spectrometers, Detectors and Associated Equipment*, 659(1):387–393, 2011.

[108] M. J. Knitel. *New inorganic scintillators and starage phosphors for detection of thermal neutrons*. PhD thesis, Delft University of technology, 1998.

[109] E.H. Lehmann, G. Frei, G. Kühne, and P. Boillat. The micro-setup for neutron imaging: A major step forward to improve the spatial resolution. *Nuclear Instruments and Methods in Physics Research Section A: Accelerators, Spectrometers, Detectors and Associated Equipment*, 576(2):389–396, 2007.

[110] P.H. Chan, P.J. Bryanston-Cross, and S.C. Parker. Fringe-pattern analysis using a spatial phase-stepping method with automatic phase unwrapping. *Measurement Science and Technology*, 6(9):1250, 1995.

[111] C. Grünzweig, J. Kopecek, B. Betz, A. Kaestner, K. Jefimovs, J. Kohlbrecher, U. Gasser, O. Bunk, C. David, E. Lehmann, et al. Quantification of the neutron dark-field imaging signal in grating interferometry. *Physical Review B*, 88(12):125104, 2013.

[112] Steven Luc Peetermans. *Energy-selective neutron imaging for materials science*. PhD thesis, STI, Lausanne, 2015.

[113] E. Nowak. On the refractive index for neutrons. *Zeitschrift für Physik B Condensed Matter*, 49(1):1–8, 1982.

[114] M. Strobl, C. Grünzweig, A. Hilger, I. Manke, N. Kardjilov, C. David, and F. Pfeiffer. Neutron dark-field tomography. *Physical review letters*, 101(12):123902, 2008.

[115] M. Strobl, I. Manke, N. Kardjilov, A. Hilger, M. Dawson, and J. Banhart. Advances in neutron radiography and tomography. *Journal of Physics D: Applied Physics*, 42(24):243001, 2009.

[116] A. Hilger, N. Kardjilov, T. Kandemir, I. Manke, J. Banhart, D. Penumadu, A. Manescu, and M. Strobl. Revealing microstructural inhomogeneities with dark-field neutron imaging. *Journal of Applied Physics*, 107(3):036101, 2010.

[117] N. Kardjilov, I. Manke, A. Hilger, M. Strobl, and J. Banhart. Neutron imaging in materials science. *Materials Today*, 14(6):248–256, 2011.

[118] F. Pfeiffer, T. Weitkamp, O. Bunk, and C. David. Phase retrieval and differential phase-contrast imaging with low-brilliance x-ray sources. *Nature physics*, 2(4):258–261, 2006.

Bibliography

[119] T. Weitkamp, A. Diaz, C. David, F. Pfeiffer, M. Stampanoni, P. Cloetens, and E. Ziegler. X-ray phase imaging with a grating interferometer. *Optics express*, 13(16):6296–6304, 2005.

[120] S. W. Lee, K. Kim, O. Y. Kwon, N. Kardjilov, M. Dawson, A. Hilger, and I. Manke. Observation of magnetic domains in insulation-coated electrical steels by neutron dark-field imaging. *Applied physics express*, 3(10):106602, 2010.

[121] E.H. Lehmann and A.P. Kaestner. 3d neutron imaging. *Encyclopedia of Analytical Chemistry*.

[122] http://www.evico magnetics.de/. single sheet magnet.

[123] B. Betz R. P. Harti M. Strobl J Hovind A. Kaestner E. Lehmann H. Van Swygenhoven and C. Grünzweig. Quantification of the sensitivity range in neutron dar-field imaging. *Review of scientific instruments*, 86, 2015.

[124] S. K. Lynch, V. Pai, J. Auxier, A. F. Stein, E. E. Bennett, C. K. Kemble, X. Xiao, W. K. Lee, N. Y. Morgan, and H. Harold Wen. Interpretation of dark-field contrast and particle-size selectivity in grating interferometers. *Applied optics*, 50(22):4310–4319, 2011.

[125] W. Yashiro, Y. Terui, K. Kawabata, and A. Momose. On the origin of visibility contrast in x-ray talbot interferometry. *Optics express*, 18(16):16890–16901, 2010.

[126] M. Strobl. General solution for quantitative dark-field contrast imaging with grating interferometers. *Scientific reports*, 4, 2014.

[127] B.Betz P. Rauscher R. P. Harti A. Irastorza-Lada R. Schäfer H. Van Swygenhoven A. Kaestner E. Pomjakushina J. Hovind E. Lehmann and C. Grünzweig. Magnetisation response of the bulk magnetic domain structure in high-permeability steel laminations in-situ visualised by neutron dark-field imaging. *Physical review applied*, submitted:–, 2015.

[128] C. Gruenzweig G. Frei E. Lehmann et al. Highly absorbing gadolinium test device to characterize the performance of neutron imaging detector systems. *Rev. Sci. Instr*, 78:053708, 2007.

[129] H. Barkhausen. Two phenomena, discovered with the help of the new amplifiers. *Phys. Z.,* 20:401–403, 1919.

[130] Prof. David Staelin. Course on electromagnetics and applications. electrically, Spring 2009.

[131] D. Markó, I. Soldatov, M. Tekielak, and R. Schäfer. Stray-field-induced faraday contributions in wide-field kerr microscopy and-magnetometry. *Journal of Magnetism and Magnetic Materials*, 396:9–15, 2015.

[132] wiki/magnetic-domain/media/file:moving-magnetic-domains-by-zureks.gif.

[133] S. Arai and A. Hubert. The profiles of lancet-shaped surface domains in iron. *physica status solidi (a)*, 147(2):563–568, 1995.

[134] M. Faraday. Subject: Faraday effect. *Ann. Phys. Chem*, 68:105, 1846.

[135] H. Richert, H. Schmidt, S. Lindner, M. Lindner, B. Wenzel, R. Holzhey, and R. Schäfer. Dynamic magneto-optical imaging of domains in grain-oriented electrical steel. *steel research international*, 2015.

[136] www.psi.ch/sinq/sansi/components.

[137] http://www.mapeng.net/news/mechanical English-article/2012/8/mapeng12812151535299.html.

[138] http://multiwire.com/index.shtml.

[139] BD Cullity. Elements of. *X-ray Diffraction*, 1978.

[140] Institut Laue-Langevin. www.ill.eu.

[141] http://www.ccp14.ac.uk/tutorial/lmgp/orientexpress.htm. Goals of orient express.

[142] K.H. Gaukler, R. Schwarzer, J. Hofmeister, G.H. Hartmann, H.P. Niemitz, and R.A. Schwarzer. Die verbesserung des bildkontrastes and durch eine ringförmige aperturblende. *Optik*, 33:215–229, 1971.

[143] B. Betz P. Rauscher R. P. Harti R. Schäfer H. Van Swygenhoven A. Kaestner J. Hovind E. Lehmann C. Grünzweig. Frequency induced bulk magnetic domain wall freezing visualized by neutron dark-field imaging. *Physical review X*, page submitted, 2015.

[144] M Pott-Langemeyer B Weidenfeller W Riehemann. Measurement and calculation of frequency dependent losses in grain oriented electrical sheets. *Soft Magnetic Materials*, 1:227–232, 2004.

[145] J. Jakubek, T. Holy, E. Lehmann, S. Pospisil, J. Uher, J. Vacik, and D. Vavrik. Spatial resolution of medipix-2 device as neutron pixel detector. *Nuclear Instruments and Methods in Physics Research Section A: Accelerators, Spectrometers, Detectors and Associated Equipment*, 546(1–2):164 – 169, 2005. Proceedings of the 6th International Workshop on Radiation Imaging DetectorsRadiation Imaging Detectors 20046th International Workshop on Radiation Imaging Detectors.

[146] A. S. Tremsin, J. B. McPhate, J. V. Vallerga, O. H.W. Siegmund, W. B. Feller, E. Lehmann, A. Kaestner, P. Boillat, T. Panzner, and U. Filges. Neutron radiography with sub-15 μm resolution through event centroiding. *Nuclear Instruments and Methods in Physics Research Section A: Accelerators, Spectrometers, Detectors and Associated Equipment*, 688:32 – 40, 2012.

[147] B. Betz, P. Rauscher, R.P. Harti, R. Schäfer, H. Van Swygenhoven, A. Kaestner, J. Hovind, E. Lehmann, and C. Grünzweig. In-situ visualization of stress-dependent bulk magnetic domain formation by neutron grating interferometry. *Applied Physics Letters*, 108(1):012405, 2016.

Acknowledgement

After many years of hard work it is now lying in front of me: my PhD-thesis.

At this time, at the end, it is time to thank those people, who have accompanied me in this challenging, but also extremely rewarding and forming phase of my life.

Primarily I do want to thank my advisers. Especially my "'supervisor"' *Dr. C. Grünzweig*. His professional supervision was probably irreplaceable, but also the privat evenings together with *Ela, Emma* and *Paul* were always great (maybe *Flor, Nari* and *Schanzi* belong also to this *family*). His hints on problems like: how to move, insure and accustom in Switzerland were very helpful, otherwise it would have become much more difficult for me.

Furthermore, I would like to thank the two Co-proposers of this work. My group leader *Dr. E. Lehmann*, who always had an open ear, whether for technical or other questions, such as the tennis championship draw. *Prof. R. Schäfer* whom I thank for the scientific input in terms of magnetism for my publications, the thesis and the fruitful discussions in Dresden. Furthermore, that he made contact with the Fraunhofer in Dresden. I also like to thank the reviewers of this work: *Prof. H. Ronnøw*, *Prof. P. Böni* and *Prof. M. Strobl* for just doing so. The last one also for the cooperation and discussions concerning the colloid experiments and papers.

Likewise, my thanks go to all those who supported me in measurements, provided samples or had those annoying discussions with me, that helped me to not lose the overview. I therefore thank the members of the "Neutron Imaging and Activation Group ", the Dresden guys, the colleagues in our hallway and all other colleagues here at the institute and at the tennis club. Some special thanks are given to my two office mates Steven and Ralph, who both provided me with important corrections, and comments for the dissertation as my fraternity brother Greg (hopefully the english fits now?) did. But not to forget: the two in the background, always making sure, that the scientists create at least something. Renate for management and other life issues and Jan for *"'physicist-safe"'* components and holders.

Very important for me are those people who already did and still continue to accompany me throughout my life. Especially at all times wherever but apart from work. I simply call them

Bibliography

Danksagung

Nach vielen Jahren intensiver Arbeit liegt sie nun vor mir: meine Dissertation.
Oder auch: Da ist das Ding!

Jetzt ist es also an der Zeit, mich bei denjenigen zu bedanken, die mich in dieser herausfordernden, aber auch ungemein lohnenswerten und prägenden Phase meines Lebens begleitet haben.

Zu besonderem Dank bin ich meinen Betreuern verpflichtet. In erster Linie meinem "'Supervisor"' und Freund *Dr. C. Grünzweig*. Einerseits war seine fachliche Betreuung unersetzlich, aber auch die vielen Abende zusammen mit *Ela*, *Emma* und *Paul* waren klasse. Seine privaten Tipps, wie man sich in der Schweiz meldet, versichert oder sonst was tut haben mir ebenfalls vieles erleichtert.

Des Weiteren möchte ich mich bei den beiden Co-Proposern dieser Arbeit bedanken. Mein Gruppenleiter *Dr. E. Lehmann*, der stets ein offenes Ohr hatte, egal ob es um fachliche oder andere Fragen, wie die Tennismeisterschaftsauslosung oder ähnlichem ging. Bei *Prof. R. Schäfer* bedanke ich mich für den fachlichen Input was die magnetischen Seiten und Fragestellungen der Arbeit angeht, sowie die fruchtbaren Diskussionen in Dresden. Des Weiteren dafür, dass er den Kontakt zum Fraunhofer in Dresden herstellte. Ebenfalls danke ich den weiteren Gutachtern dieser Arbeit: *Prof. H. Ronnøw*, *Prof. P. Böni* und *Prof. M. Strobl* für eben dieses. Bei letzterem ebenfalls für die gemeinsamen arbeiten an allem was mit Kolloiden zu tun hatte.

Ebenso geht mein Dank an alle diejenigen, welche mich bei Messungen unterstützt oder mich mit Proben versorgt oder in nervigen Diskussionen mir geholfen haben den Überblick nicht zu verlieren. Daher danke ich den Mitgliedern der "'Neutron Imaging and Activation Group"', den Dresdenern, den Kollegen auf unserem Flur und allen anderen Kollegen hier am Institut und beim Tennis. Etwas spezieller noch geht mein Dank an meine beiden Bürokollegen Steven und Ralph, die mich beide ebenso mit wichtigen Korrekturen und Kommentaren für die Dissertation versorgt haben wie mein Bundesbruder Greg (hoffentlich passt das Englisch jetzt?). Nicht zu vergessen: Die beiden die im Hintergrund immer dafür sorgen das die Physiker zumindest irgend etwas schaffen: Renate für Verwaltung und sonstige Lebensfragen und Jan für *"'physikersichere"'* Bauteile und Halterungen.

Bibliography

Ganz wichtig für mich sind auch die Personen, die mich weiter durch mein Leben begleiteten und mit mir die Zeiten ausserhalb der Arbeit teilten und hoffentlich weiter teilen. Um sie einfach zu nennen, meine **Freunde**. *Freundschaft muss auf einem soliden Fundament, welches auf Alkohol, Sarkasmus und Schweinereien aufbaut, stehen.* Solche Menschen durfte ich in verschiedenen Kreisen kennenlernen: Schule, Macaria, RUF, Schottland, Uni, Handball, Fussballclique (Hornussen & Brunegg). Dies gilt aber auch für alle anderen die sich mit mir am Leben freuen.

Eine herausragende Stellung in jeglicher Hinsicht nimmt meine Familie ein. Ohne diese wäre weder ich derjenige der ich bin, noch wäre diese Arbeit jemals entstanden. In den letzten Jahren zähle ich nicht nur die in Herchenrath sondern auch die in Dettenhausen dazu. Meine Geschwister Veronika, Maximiliane und Leonard (auch Christopher und Martin gehören mittlerweile dazu) haben mich geprägt, am meisten jedoch meine Eltern: Thomas und Monika. Danke für all eure immerwährende Unterstützung.

Als letztes danke ich noch der wichtigsten Person in meinem Leben: Meinem Hasen. Du bist der einzige Mensch, der mich tagtäglich aushällt, und das meist sogar ganz gerne (hoffe ich zumindest). Danke das du bist wie du bist, und mich, obwohl manchmal Tollpatsch oder Sheldon, so liebst wie ich bin.

Klingnau, 4. April 2016   B. B.

List of Publications

Publications

First author

- *Advances in Neutron Imaging with Grating Interferomerty*; B. Betz, C. Grünzweig, E. H. Lehmann; Materials Evaluation; **72**; 491-496, (2014)

- *Visualization of Bulk Magnetic Properties by Neutron Grating Interferometry*; B. Betz, P. Rauscher, R. Siebert, R. Schäfer, A. Kaestner, H. Van Swygenhoven, E. Lehmann, C. Grünzweig; Physics Procedia; **69**; 413-419, (2015)

- *Quantification of the sensitivity range in neutron dark-field imaging*; B. Betz, R. P. Harti, M. Strobl, J. Hovind, A. Kaestner, E. Lehmann, H. Van Swygenhoven, and C. Grünzweig; Review of scientific instruments; **86**, http://dx.doi.org/10.1063/1.4937616 (2015)

- *In-situ visualization of stress-dependent bulk magnetic domain formation by neutron grating interferometry*; B. Betz, P. Rauscher, R. P. Harti, R. Schäfer, H. Van Swygenhoven, A. Kaestner, J. Hovind, E. Lehmann, and C. Grünzweig; Applied Physics Letters; **108** 1; (2016)

- *Magnetisation response of the bulk magnetic domain structure in high-permeability steel laminations in-situ visualised by neutron dark-field imaging*; B. Betz, P. Rauscher, R. P. Harti, A. Irastorza-Lada, R. Schäfer, H. Van Swygenhoven, A. Kaestner, E. Pomjakushina, J. Hovind, E. Lehmann, and C. Grünzweig; in review; (2015)

- *Frequency induced bulk magnetic domain wall freezing visualized by neutron dark-field imaging*; B. Betz, P. Rauscher, R. P. Harti, R. Schäfer, H. Van Swygenhoven, A. Kaestner, J. Hovind, E. Lehmann, and C. Grünzweig; in review; (2015)

Bibliography

Co - author

- *Localized investigation of magnetic bulk property deterioration of electrical steel: Analysing magnetic property drop thorough mechanical and laser cutting of electrical steel laminations using neutron grating interferometry*; R. Siebert, A. Wetzig, E. Beyer, B. Betz, C. Grünzweig, E. Lehmann; Electric Drives Production Conference (EDPC); 1-5, (2013)

- *Quantification of the neutron dark-field imaging signal in grating interferometry*; C. Grünzweig, J. Kopecek, B. Betz, A. Kaestner, K. Jefimovs, J. Kohlbrecher, U. Gasser, O. Bunk, C. David, E. Lehmann, T. Donath, F. Pfeiffer; Physical Review B; **88**; 125104, (2013)

- *Localized investigation of magnetic bulk property deterioration of electrical steel*; R. Siebert, A. Wetzig, E. Beyer, B. Betz, C. Grünzweig, E. Lehmann; International Electric Drives Production Conference Nuremberg, Germany; (2013)

- *Instrumentation in Neutron Imaging—A world-wide overview*; E. H. Lehmann, S. Peetermans, B. Betz; Neutron News; **26**; 6-10, (2015)

- *Determination of Bulk Magnetic Volume Properties by Neutron Dark-Field Imaging*; C. Grünzweig, R. Siebert, B. Betz, P. Rauscher, R. Schäfer, E. Lehmann; Physics Procedia; **69**; 413-419, (2015)

- *Visualizing the morphology of vortex lattice domains in a bulk type-II superconductor*; T. Reimann, S. Mühlbauer, M. Schulz, B. Betz, A. Kaestner, V. Pipich, P. Böni, C. Grünzweig; Nature Communications; **6**; (2015)

- *New neutron imaging techniques to close the gap to scattering applications*; E. H. Lehmann, S. Peetermans, P. Trtik, B. Betz, C. Grünzweig; ECNS , Sevilla; accepted; (2015)

- *Wavelength dispersive dark-field contrast: micrometer structure resolution in neutron imaging with gratings*; M. Strobl, B. Betz, R. P. Harti, A. Hilger, N. Kardjilov, I. Manke and C. Gruenzweig; J. Appl. Cryst., **49**, 569–573; (2016)

Conferences

- B.Betz; *Providing additional contrast information by neutron grating interferometry compared to conventional imaging*; American society for non-destructive testing, 22nd research symposium; Memphis, USA, March 2013, oral presentation

- B. Betz; *Visualization of magnetization processes in electrical steel laminations by neutron grating Interferometry*; XNPIG 2014 Garmisch-Patenkirchen, Germany, January 22, 2014, oral presentation

- B. Betz; *Visualization of bulk magnetic properties by neutron grating interferometry*; Neuwave 6, Garching, Germany, April 8, 2014, oral presentation

- B. Betz; *Visualization of bulk magnetic properties by neutron grating interferometry*; IEEE Intermag, Dresden, Germany, April 17, 2014, oral presentation

- B. Betz, C. Grünzweig, E. Lehmann, H. Van Swygenhoven; *Neutron grating interferometry for material research*; EDMX-Day EPFL Lausanne, Switzerland, September 13, 2014, poster

- B. Betz, C. Grünzweig, E. Lehmann, H. Van Swygenhoven; *Grating interferometry with neutrons*; WCNR 10 Grindelwald, Switzerland, October 7, 2014, poster

- B. Betz; *Visualization of bulk magnetic properties by neutron grating Interferometry*; ECNS, Sevilla, Spain; 2015, oral presentation

- B. Betz, C. Grünzweig, E. Lehmann and H. Van Swygenhoven; *Neutron grating interferometry – Dark-field imaging*; EDMX-Research Day EPFL Lausanne, Switzerland, Novenmber 23, 2015, poster

Teaching

Supervision of a summerstudent; Jan Reuter; (8 weeks); *Characterisation of electrical steel laminations using neutron grating interferometry and Laue XRD*

Diplom-Physiker
Benedikt Betz

Persönliche Daten

Anschrift	Traubenweg 85
	CH-5313 Klingnau
E-Mail	BKJG.Betz@gmail.com
Telefon	+41 [0] 56 555 8295
Mobil	+41 [0] 786623302
Geboren	11.08.1984 in Köln
Familienstand	ledig
Nationalität	deutsch

Schule, Ausbildung und Studium:

03.2012 – voraussichtlich 02.2016	**Dissertation,** Paul-Scherrer Institut, Villigen, Schweiz (EPFL Lausanne) Neutron imaging and activation group, Thema: "*Visualization of magnetic domain structures and magnetization processes in grain oriented, high permeability steels by neutron grating interferometry*"
11.2011 – 02.2012	**Wissenschaftliche Hilfskraft,** Eberhard-Karls-Universität Tübingen, Physikalisches Institut II,
10.2010 – 10.2011	**Diplomarbeit,** Eberhard-Karls-Universität Tübingen, Physikalisches Institut II, Thema: „*Fabrikation von dickemodulierten Nb-Filmen zur Untersuchung der statischen und dynamischen Eigenschaften von Abrikosov-Vortizes in maßgeschneiderten Potentialen*"
04.2008 – 10.2011	**Studium der Physik** an der Eberhard-Karls-Universität Tübingen Schwerpunkte Nanotechnologie und Festkörperphysik **Diplom**: 10.2011
10.2005 – 03.2008	**Studium der Physik** an der Universität zu Köln **Vordiplom**: 03.2008
10.2004 – 09.2005	**Wehrdienst**, Deutsche Marine, Fregatte Schleswig-Holstein Signalgast, Kommunikation mittels Lichtmorsen, Flaggenalphabet und Sprechfunk
09.1995 – 05.2004	Antoniuskolleg Neunkirchen-Seelscheid: **Allgemeine Hochschulreife 06/2004**

Weitere Tätigkeiten

2000 (6 Wochen)	Ferienarbeit, Bauunternehmen Rückert, Much
2001 - 2004	Nebenjob, Shell-Tankstelle, Much
2006 - 2013	Chefreiseleiter bei Ruf-Jugendreisen, Bielefeld
2009 - 2011	Betreuung des physikalischen Anfängerpraktikums für Naturwissenschaftler, Tübingen

Kenntnisse

Fremdsprachen	➢ **Englisch:** fließend / verhandlungssicher
	➢ **Französisch:** erweiterte Kenntnisse
	➢ **Spanisch:** Grundkenntnisse
Software	➢ Fundierte Kenntnisse in Windows, Scientific Linux
	➢ Büroanwendungen: MS Office, Open Office, Latex
	➢ Mathematisch-naturwissenschaftliche Software: Origin, Labview, Elphy Plus, MatLab, Orient Express, ImageJ, Virtual Studio
Sonstiges	➢ PKW & Motorrad-Führerschein

Interessen, Hobbys

Diverse Sportarten (Tennis, Handball, Fussball, Skifahren, Radfahren, Wandern), Reisen, Musik, Literatur

Ehrenämter, Mitgliedschaften

➢ Diverse Vereinstätigkeiten im Tennis – sowie Handballverein

➢ Vorsitzender der Jugendabteilung des Tambourcorps Kreuzkapelle

➢ Vorstandsmitglied der Jungen Union Much

➢ Mitglied im Organisationskommitee der Schule

➢ 1. Stellvertretender Sprecher des Coburger Conventes (2013)